

Space-Time Residual Distribution Schemes and  
Application to Two-Phase Flow Computations on  
Unstructured Meshes

Mario Ricchiuto  
Supervisor: H. Deconinck  
Advisor: Á. Csík

June 2001



# Acknowledgments

The last days have come, the work is over<sup>1</sup> and the time to say *goodbye* is very very close. This was one of the most difficult years of my entire life and also probably the best. I know that nothing like this will never happen again to me and probably to any of my fellows...I will miss them a lot !

Thank U fellows.....

Of course most of the time here I spent it working and once more my supervisor has proven to be able to give me the support which I need to perform always at my best... This year I've also discovered that Gerard Degrez, besides being a bright mind, is one of the best teachers I've ever met... Arpi, apart from being the best collaborator I could have had this year, U behaved like a friend and this was the best of it.

A special thanks goes of course to my parents and my sister.... they say they're very proud of me, but they can't even imagine how much I missed them and how much proud of them I am.

---

<sup>1</sup>almost



## **Abstract**

The extension of Residual Distribution Schemes to general unsteady and complex inhomogeneous systems of conservation laws poses several technical difficulties which have made many efforts unsuccessful until now. First, the schemes in their original formulation cannot be more than first order accurate in space in unsteady computations due to an inconsistent treatment of the time derivative in the discretization. Furthermore, the conservation property strongly relies on the existence of a Roe-type linearization of the Jacobians of the system which is not available in general. Finally, including forcing terms in the discretization in a consistent way has not been achieved until now.

The goal of this project was therefore to cure the above problems and to demonstrate the application towards complex hyperbolic systems on a two-fluid two-phase flow model. Second order of accuracy in time and space was obtained by using a space-time approach for which general boundary conditions based on characteristic eigenvector decomposition were implemented. A new source-term discretization, consistent with the Residual Distribution method, has been proposed and tested. This new treatment of the forcing terms has been shown to be robust and extendable to second order of accuracy. The same idea at the basis of the source term discretization allowed rewriting the schemes in a way that does not require any Roe-type linearization of the Jacobians to guarantee discrete conservation. Comparison with the classical formulation has shown the robustness and reliability of the approach. Finally, the space-time schemes, combined with the new treatment of the source terms, have been applied to a simple two-phase flow model. The solution of some well known two-phase flow problems involving separated flow is shown.



# Contents

<b>1</b>	<b>Introduction</b>	<b>1</b>
1.1	Unsteady Computations, $\mathcal{LP}$ property and Mass Matrix . . . . .	2
1.2	Source terms and $\mathcal{LP}$ property . . . . .	3
1.3	Conservative Linearization and Quasi-Linear Equations . . . . .	5
1.4	Physical and Numerical Modeling of Two-Phase Flow . . . . .	6
<b>2</b>	<b>Residual Distribution Schemes</b>	<b>9</b>
2.1	$\mathcal{RD}$ Schemes for Steady Hyperbolic Problems . . . . .	9
2.1.1	$\mathcal{RD}$ Schemes for Scalar Advection . . . . .	9
2.1.2	Matrix Schemes for Hyperbolic Systems . . . . .	14
2.2	Space-Time $\mathcal{RD}$ Schemes . . . . .	19
2.2.1	Unsteady Scalar Conservation Laws . . . . .	19
2.2.2	Unsteady Hyperbolic Systems . . . . .	25
<b>3</b>	<b>New Developments for <math>\mathcal{RD}</math> Schemes: Source Terms and Conservation</b>	<b>27</b>
3.1	$\mathcal{RD}$ Schemes for Non-Homogeneous Equations . . . . .	27
3.1.1	An N-Scheme for Non-Homogeneous Equations . . . . .	28
3.1.2	A $\mathcal{LP}$ Scheme for Non-Homogeneous Equations . . . . .	30
3.2	A New Approach for Conservative $\mathcal{RD}$ Schemes Based on the N Scheme . . . . .	32
3.2.1	A Conservative N-Scheme for General Systems of Conservation Laws . . . . .	32
3.2.2	A Conservative $\mathcal{LP}$ Scheme for General Systems of Conservation Laws . . . . .	33
3.2.3	Contour Integration . . . . .	33
<b>4</b>	<b>Boundary Conditions and Time Integration</b>	<b>37</b>
4.1	Characteristics-Based B.C.s . . . . .	37
4.2	Local Time-Stepping Technique . . . . .	42
<b>5</b>	<b>Results</b>	<b>43</b>
5.1	Euler Equations . . . . .	43
5.1.1	Unsteady Computations . . . . .	44
5.1.2	Steady Computations . . . . .	58
5.2	Two-Fluid Mechanical Equilibrium Model . . . . .	67
<b>6</b>	<b>Conclusions, Final Remarks and Future Perspectives</b>	<b>79</b>

<b>A</b>	<b>Consistency of the <math>N^S</math> Scheme in 1D</b>	<b>83</b>
<b>B</b>	<b>The New N Scheme is <math>IST</math></b>	<b>85</b>
<b>C</b>	<b>Flux Computations</b>	<b>87</b>
	C.1 Second Order Flux Integration . . . . .	87
	C.2 Third Order Flux Integration . . . . .	88
<b>D</b>	<b>Boundary Conditions</b>	<b>91</b>
	D.1 Euler Equations . . . . .	91
	D.2 Two-Phase Equilibrium Model . . . . .	95
<b>E</b>	<b>Equations, Jacobians and Eigenvalue Decompositions</b>	<b>97</b>
	E.1 2D Euler Equations . . . . .	97
	E.2 1D Euler Equations . . . . .	98
	E.3 2D Two-Phase Equilibrium Model . . . . .	100
	E.4 1D Two-Phase Equilibrium Model . . . . .	100

# List of Figures

1.1	1D $\mathcal{RD}$ scheme . . . . .	4
2.1	Tent-shaped interpolation function $N_i$ . . . . .	9
2.2	2D and 3D grid geometry . . . . .	10
2.3	Median Dual Cell in 2D . . . . .	11
2.4	Space-time mesh in 1D. Nodes at levels $n$ , $n + 1/2$ and $n + 1$ are labeled by black, gray and empty circles, respectively. . . . .	21
2.5	Basic triangular elements in the first layer . . . . .	21
2.6	Space-time mesh in 2D. Nodes at levels $n$ , $n + 1/2$ and $n + 1$ are respectively labeled by black, gray and empty circles. Squares indicate intermediate nodes positioned in the centroid of the triangles of the level $n$ spatial mesh. . . . .	22
2.7	Basic tetrahedra used to build the first layer of the space-time mesh in two space dimensions, and schematic view of the mesh. . . . .	23
2.8	Elementary tetrahedra of types E1 (left) and E2 (right) . . . . .	24
4.1	In-going and outgoing waves at the boundaries and boundary conditions . . . . .	38
4.2	Nodal normal at the boundary . . . . .	39
5.1	Expansion at the Singular Point, $t = 0.5$ . Left: Solution From [7], Right: Solution Obtained with the Space-Time Approach . . . . .	45
5.2	Unphysical Mach Stem on the Lower Wall, $t = 4.0$ . Left: Solution from [30], Right: Solution Obtained with the Space-Time Approach . . . . .	45
5.3	Entropy Production at the Corner . . . . .	46
5.4	Effect of the Progressive Grid Refinement Around the Corner (from [30]) . . . . .	46
5.5	Grid Refinement Around the Corner and Improvement of the Solution . . . . .	47
5.6	Mach 3 Wind Tunnel with a Step, Solutions at $t = 1.0$ and $t = 1.5$ . Top: Present, Bottom: Reference Solution [29] . . . . .	48
5.7	Mach 3 Wind Tunnel with a Step, Solutions at $t = 3.0$ and $t = 4.0$ . Top: Present, Bottom: Reference Solution [29] . . . . .	48
5.8	Mach 3 Wind Tunnel with a Step: Solution at $t = 4.0$ Obtained with the B Scheme Based on the New Treatment of Conservation . . . . .	49
5.9	Transonic Channel: Grid (left) and Mach Contours of the Initial Solution (right) . . . . .	49
5.10	Transonic Channel: Unsteady Solution, $\omega t = 2\pi$ . Left: Present, Right: [33] . . . . .	50
5.11	Transonic Channel: Unsteady Solution, $\omega t = 18\pi/8$ . Left: Present, Right: [33] . . . . .	50
5.12	Transonic Channel: Unsteady Solution, $\omega t = 20\pi/8$ . Left: Present, Right: [33] . . . . .	50
5.13	Transonic Channel: Unsteady Solution, $\omega t = 22\pi/8$ . Left: Present, Right: [33] . . . . .	51

5.14	Transonic Channel: Unsteady Solution, $\omega t = 24\pi/8$ . Left: Present, Right: [33]	51
5.15	Transonic Channel: Unsteady Solution, $\omega t = 26\pi/8$ . Left: Present, Right: [33]	51
5.16	Transonic Channel: Unsteady Solution, $\omega t = 28\pi/8$ . Left: Present, Right: [33]	51
5.17	Transonic Channel: Unsteady Solution, $\omega t = 4\pi$ . Left: Present, Right: [33]	51
5.18	Initial Physical State for the Cylindrical Riemann Problem	52
5.19	Close-up View of the Isotropic Mesh used for the Cylindrical Riemann Problem	54
5.20	Cylindrical Riemann Problem: $t = 0.4$ , B scheme. Left: density, Right: pressure	54
5.21	Cylindrical Riemann Problem: Comparison of the 1D Solution (solid line) with cuts of the 2D Solution Along Rays at Different Angles (symbols)	55
5.22	1D Cylindrical Riemann Problem: $t = 0.4$ , density. Left: B scheme, Right: N scheme	56
5.23	1D Cylindrical Riemann Problem: $t = 0.4$ , pressure. Left: B scheme, Right: N scheme	56
5.24	1D Cylindrical Riemann Problem: $t = 0.4$ , Mach. Left: B scheme, Right: N scheme	57
5.25	1D Cylindrical Riemann Problem: comparison between N and B schemes both with the new consistent treatment of the source term	57
5.26	Cross-Sectional Area Variation for the Quasi-1D Nozzle Flow Simulations	58
5.27	Steady Quasi-1D Euler: Mach Number distribution along the nozzle. (a) Fully Subsonic, (b) Chocked Subsonic, (c) Adapted, (d) Transonic Shock, (e) Fully Supersonic	59
5.28	Jets Interaction Problem: Problem Description and Zoom of the grid	60
5.29	Jets Interaction Problem: Solution obtained with the new schemes. Left: N scheme, Right: B scheme	61
5.30	Jets Interaction Problem: Comparison with Roe Averaging, Outlet Mach Number. Left: N scheme, Right: B scheme	61
5.31	Scramjet Inlet. Particular of the Grid	62
5.32	Scramjet Inlet: Mach Number Isolines. Left: new N Scheme, Right: new B Scheme	62
5.33	Scramjet Inlet: density along the symmetry line, comparison with Roe averaging. Left: N scheme, Right B scheme. Symbols: New Approach, Solid: Roe Average	63
5.34	Scramjet Inlet: pressure along the symmetry line, comparison with Roe averaging. Left: N scheme, Right B scheme. Symbols: New Approach, Solid: Roe Average	63
5.35	Scramjet Inlet: Mach number along the symmetry line, comparison with Roe averaging. Left: N scheme, Right B scheme. Symbols: New Approach, Solid: Roe Average	63
5.36	Mach 10 Flow Over a Cylinder: comparison with Roe averaging	64
5.37	Mach 10 Flow Over a Cylinder: Stagnation point	64
5.38	Mach 10 Flow Over a Cylinder: comparison with Roe averaging. Pressure and Mach distribution along the symmetry line	65
5.39	Mach 4 Flow Over a Sphere: Mach (left) and pressure (right) isolines	66

5.40	Mach 4 Flow Over a Sphere: Mach (left) and pressure (right) isolines at the Stagnation Point . . . . .	66
5.41	Mach 4 Flow Over a Sphere: Mach (left) and pressure (right) distribution along the axis of symmetry . . . . .	66
5.42	Oscillating Manometer: Problem Statement and Initial Condition . . . . .	69
5.43	Oscillating Manometer Problem: Comparison with the Exact Solution. Left: 201 nodes - $CFL = 1$ , Right: 201 nodes - $CFL = 10$ . . . . .	70
5.44	Oscillating Manometer Problem: Comparison with the Exact Solution. Left: 201 nodes - $CFL = 20$ , Right: 401 nodes - $CFL = 20$ . . . . .	70
5.45	Oscillating Manometer Problem: Comparison with the Exact Solution. Left: 201 nodes - influence of $CFL$ number, Right: $CFL = 20$ - Influence of grid resolution . . . . .	71
5.46	Sloshing of a Water Column: Geometry of the Problem and Initial Condition . . . . .	72
5.47	Sloshing of a Water Column: Comparison with Experimental Data . . . . .	73
5.48	Sloshing of a Water Column: Gas Void Fraction. Left: $t^* = 0$ , Right: $t^* \approx 1.2$ . . . . .	73
5.49	Sloshing of a Water Column: Gas Void Fraction. Left: $t^* \approx 2.5$ , Right: $t^* \approx 3.8$ . . . . .	74
5.50	Sloshing of a Water Column: Gas Void Fraction. Left: $t^* \approx 5.2$ , Right: $t^* \approx 6.5$ . . . . .	74
5.51	Sloshing of a Water Column: Gas Void Fraction. Left: $t^* \approx 7.8$ , Right: $t^* \approx 9$ . . . . .	75
5.52	Gas Plume Problem: Gas Void Fraction at the inlet. Left: $t = 0.2$ s, Right: $t = 0.4$ s . . . . .	76
5.53	Gas Plume Problem: Gas Void Fraction at the inlet. Left: $t = 0.6$ s, Right: $t = 0.8$ s . . . . .	76
5.54	Gas Plume Problem: Gas Void Fraction at the inlet. Left: $t = 1.0$ s, Right: $t = 1.2$ s . . . . .	77
5.55	Gas Plume Problem: Gas Void Fraction at the inlet. Left: $t = 1.4$ s, Right: $t = 1.6$ s . . . . .	77
A.1	$\mathcal{RD}$ formulation of a 1D Finite Volume Scheme . . . . .	83
C.1	Contour Integration with Trapezium Rule . . . . .	87
C.2	Contour Integration on a Triangle with Simpson's Rule . . . . .	88



# List of symbols

## Alphanumeric symbols

$a$	: speed of sound ; 1D advection speed
$A$	: jacobian matrix; cross-sectional area
$A$	: jacobian matrix
$\mathbf{B}, B$	: jacobian matrix
$\mathbf{B}_i^T$	: distribution matrix of node $i$ in element $T$
$C$	: jacobian matrix
$CFL$	: Courant-Friederichs-Lewy number
$d$	: number of space dimensions
$\mathbf{D}^k$	: boundary coefficient vector
$e$	: 1D grid element
$E$	: multidimensional grid element; total energy
$f, F, \vec{\mathcal{F}}$	: flux function, $x$ component
$\vec{F}$	: force
$g$	: flux function, $y$ component; gravity
$G, \vec{\mathcal{G}}$	: flux function, $y$ component
$h$	: mesh size
$H$	: flux function, $z$ component; total enthalpy
$i$	: node of a grid element
$I$	: identity matrix
$i_j^+$	: positive unit upwind parameter of node $j$
$I_j^+$	: positive matrix unit upwind parameter of node $j$
$k_j^T$	: upwind parameter of node $j$ of element $T$
$k_j^+$	: positive upwind parameter of node $j$
$K_j^T$	: matrix upwind parameter of node $j$ of element $T$
$K_j^+$	: matrix positive upwind parameter of node $j$
$L$	: left eigenvectors matrix; water column dimension
$m_{ij}^T$	: mass matrix
$M$	: Mach number
$\vec{n}_i$	: unit boundary nodal vector
$\vec{n}_\Omega$	: unit boundary normal vector
$N_i$	: linear base function of node $i$
$p$	: pressure

$p_0$	: total pressure
$\tilde{p}_0$	: modified total pressure
$P$	: vector of primitive variables
$\mathbf{q}$	: heat flux vector
$Q$	: space-time grid stretching factor
$\mathbf{r}^k$	: right eigenvector
$R$	: right eigenvectors matrix
$R_i, \mathbf{R}_i$	: nodal residual
$s$	: edge of a grid element
$S$	: source term
$S_i$	: area of the median dual cell of node $i$
$t$	: time
$T$	: grid element
$u$	: scalar field; $x$ velocity component
$U$	: vector field; conservative variables
$v$	: $y$ velocity component
$w$	: number of independent coordinates
$W$	: vector of dependent variables
$u, v$	: velocity components
$x, y, z$	: Cartesian coordinates
$\mathbf{Z}$	: Roe's parameter vector

## Greek symbols

$\alpha$	: void fraction
$\beta^k$	: boundary condition coefficient
$\beta_i^T$	: distribution coefficient of node $i$ of element $T$
$\gamma$	: ratio of specific heats
$\delta$	: provisional increment
$\delta_{ij}$	: Kroenecker's tensor
$\epsilon$	: convergence threshold
$\theta$	: blending coefficient
$\Theta$	: blending matrix
$\vec{\lambda}$	: advection speed
$\lambda$	: space-time advection speed
$\lambda_i$	: jacobian eigenvalue
$\Lambda$	: matrix of the eigenvalues
$\nu$	: pseudo time $CFL$ number
$\rho$	: density
$\sigma$	: 1D scalar source term
$\Sigma$	: multidimensional scalar source term
$\tau$	: pseudo-time
$\phi^T, \Phi^T$	: element residual

$\phi_i^T, \Phi_i^T$  : element-to-node residual contribution  
 $\omega$  : frequency of oscillation  
 $\Omega$  : physical domain

## Superscripts symbols

$c$  : conservative  
 $e$  : relative to element  $e$   
 $E$  : relative to element  $E$   
 $n$  : time level  
 $t$  : transposed vector  
 $T$  : relative to element  $T$   
 $+$  : positive part  
 $-$  : negative part

## Subscripts symbols

$i$  : current node  
 $j$  : current node  
 $k$  : current node; current phase  
 $P$  : relative to primitive variables  
 $U$  : relative to conservative variables  
 $x, y, t$  : component of a vector



# Chapter 1

## Introduction

Over the last decade, a class of upwind spatial discretization schemes has been developed for the solution of systems of hyperbolic conservation laws on unstructured grids [1, 2]. The Residual Distribution ( $\mathcal{RD}$ ) or Fluctuation Splitting Schemes incorporate the same properties which are at the basis of all Godunov-type upwind finite volume schemes, but carried over to a cell-vertex framework with a continuous representation of the variables, like in the standard finite element method. The strength of the method lays in the fact that both monotonicity and second order of accuracy can be obtained on the compact stencil of nearest neighbors, which also enables an easier implicit and parallel implementation. The key feature of the  $\mathcal{RD}$  method is the truly multidimensional upwinding at its basis, which allows to reproduce numerically the multidimensionality of the physics. Successful application of the schemes to the steady 2D and 3D Euler and Navier Stokes Equations, to the MHD equations and to Two-Fluid Models for two-phase flow simulation, has been shown in the past [1, 2, 3, 4, 5]. However, those methods still have several limitations. First of all, the schemes have been developed for the solution of steady state problems and when they are applied to the simulation of unsteady flows, their accuracy is degraded even if used in combination with the method of lines ( Runge-Kutta schemes for example ). Furthermore, their application to flows with strong discontinuities strongly relies on the existence of a conservative Roe-type linearization of the Jacobian matrices of the system, which is not always guaranteed, as, for example, in the case of two-phase flow models such as the Two-Fluid models and of the MHD equations. In addition, up to now a consistent discretization of the source terms has not been found. In particular the point-wise treatment that has been used until now, reduces the accuracy of the second order schemes to first order, while a centered treatment is most of the times unstable. In the following sections these three problems will be analyzed and explained, summarizing the work done in the past years to cure them, and anticipating some of the results obtained in the course of this work. In the last section some information will be given on the two-phase flow modeling and on the related numerical issues. In particular the work previously done at the von Karman Institute will be briefly summarized and the simple model used in the computations introduced.

# 1.1 Unsteady Computations, $\mathcal{LP}$ property and Mass Matrix

Consider the following simple scalar problem

$$\frac{\partial u}{\partial t} + \vec{\lambda} \cdot \nabla u = 0, \quad (1.1)$$

where  $\vec{\lambda}$  is a constant vector. We wish to solve equation (1.1) on an unstructured mesh (triangles in 2D, tetrahedra in 3D). The basic idea of the Fluctuation Splitting schemes is to compute the integral of the advective fluxes on every computational cell and then to distribute portions of it to every node belonging to the element. In formulas:

$$\phi^T = \int_T \vec{\lambda} \cdot \nabla u \, d\Omega \quad R_i += \beta_i^T \phi^T; \quad (1.2)$$

where  $\beta_i^T$  is the so-called distribution coefficient,  $R_i$  is the global residual for node  $i$  and the symbol += indicates that the value of the residual is updated with the portion of the advective fluxes coming from element  $T$ . It can be shown [1] that if the distribution coefficient is bounded, i.e. for  $\phi^T$  going to zero,  $\beta_i^T \phi^T$  also goes to zero, then the scheme is able to reproduce exactly steady linear solutions of (1.1) and hence is second order accurate at steady state. This property is usually called  $\mathcal{LP}$  property or residual property. Of course the  $\mathcal{LP}$  property holds only for steady state computations, in fact for an unsteady solution one can write

$$\phi^T = - \int_T \frac{\partial u}{\partial t} \, d\Omega \neq 0.$$

As a consequence one has that in unsteady computations schemes that are  $\mathcal{LP}$  at steady state, lose this property, hence second order of accuracy is lost.

A different way to explain the lower accuracy that linearity preserving schemes show in unsteady computations can be found in the work done by Maerz [6]. He started observing that any  $\mathcal{LP}$  scheme can be written as a finite element Petrov-Galerkin method with test function given by

$$\omega_i^T = N_i^T + \left(\beta_i^T - \frac{1}{d+1}\right)\gamma^T,$$

where  $N_i^T$  is the linear Galerkin base function,  $d$  the number of spatial dimensions, and  $\gamma^T$  is a piece-wise constant function which is zero outside of element  $T$  and 1 on it. As a consequence, for consistency, the discretization of unsteady problems should include a so-called mass matrix defined on each element  $T$  as

$$m_{ij}^T = \int_T \omega_i^T N_j^T \, d\Omega = \frac{\Omega_T}{3} \begin{bmatrix} \frac{1}{2} + \beta_1^T - \frac{1}{3} & \frac{1}{4} + \beta_1^T - \frac{1}{3} & \frac{1}{4} + \beta_1^T - \frac{1}{3} \\ \frac{1}{4} + \beta_2^T - \frac{1}{3} & \frac{1}{2} + \beta_2^T - \frac{1}{3} & \frac{1}{4} + \beta_2^T - \frac{1}{3} \\ \frac{1}{4} + \beta_3^T - \frac{1}{3} & \frac{1}{4} + \beta_3^T - \frac{1}{3} & \frac{1}{2} + \beta_3^T - \frac{1}{3} \end{bmatrix}.$$

The final semi-discrete equation for node  $i$  then becomes

$$\sum_{T \in \Delta_i} \sum_{j \in T} m_{ij}^T \frac{du_j}{dt} + \sum_{T \in \Delta_i} \beta_i^T \phi^T = 0$$

where  $\Delta_i$  represents the set of elements surrounding node  $i$ . It must be noted that, since the mass matrix is not diagonal, the method becomes implicit. Although the use of the mass matrix allows to recover second order of accuracy in unsteady computations, as shown in [6], monotonicity problems arise from the fact that the matrix is not positive defined. In [7] Ferrante tried to cure this problem through the use of a limiting procedure of the Flux Corrected Transport ( $\mathcal{FCT}$ ) type (see reference [8, 9]), but without satisfactory results, at least for the Euler equations.

A different approach to solve the problem of the accuracy has been tried in [10, 11, 12]. The authors used the  $\mathcal{RD}$  formulation of the Lax-Wendroff scheme combined with a Flux Corrected Transport limiting procedure to obtain second order monotone solutions of unsteady problems. The second order of accuracy of the Lax-Wendroff scheme was shown for a 2D advection equation like the (1.1) in [11] through the use of the 2D modified equation, and in [10] through an equivalent equation and grid refinement studies. Although for scalar problems the results shown compare reasonably well with the ones obtained using the consistent mass matrix with the  $\mathcal{FCT}$  limiting, for the Euler equations monotonicity problems are still present.

More recently another technique to get back second order of accuracy in unsteady computations has been, and is being, investigated. The basic idea is to maintain the  $\mathcal{LP}$  property in unsteady problems by including the time derivative in the definition of the cell residual  $\phi^T$  (see equation (1.2)):

$$\phi_{s-t}^T = \int_T \left( \frac{\partial u}{\partial t} + \vec{\lambda} \cdot \nabla u \right) d\Omega .$$

Once this has been done, the use of a positive linearity preserving scheme in space-time will guarantee second order accurate monotone solutions also for unsteady computations. This is the idea at the basis of the space-time formulation of the  $\mathcal{RD}$  schemes which are the basis of this project and that will be extensively described in section 2.2. Promising results obtained using this new formulation have been shown in [13] and in [14, 15].

It is important to underline that positive linearity preserving schemes do exist; an overview of their design methods can be found in [16].

## 1.2 Source terms and $\mathcal{LP}$ property

Consider now the following 1D scalar non-homogeneous advection problem:

$$\frac{\partial u}{\partial t} + a \frac{\partial u}{\partial x} = \sigma . \tag{1.3}$$

The 1D version of a  $\mathcal{LP}$  fluctuation splitting scheme is obtained as follows:

$$\phi^e = \int_{x_1^e}^{x_2^e} \left( a \frac{\partial u}{\partial x} - \sigma \right) dx \quad R_{i+=} = \beta_i^e \phi^e , \tag{1.4}$$

where  $x_1^e$  and  $x_2^e$  are the coordinates of the extrema  $i$  and  $i + 1$  of segment  $e$  (see figure 1.1). Any steady solution of (1.3) will be reproduced with second order of accuracy by any scheme

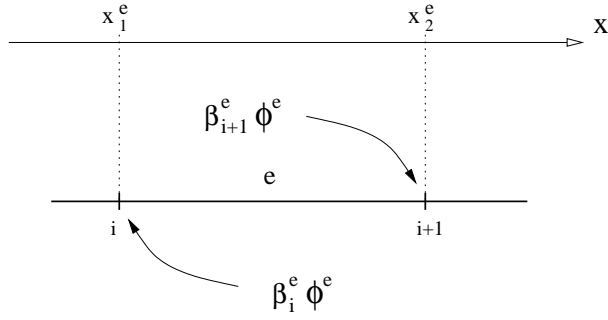


Figure 1.1: 1D  $\mathcal{RD}$  scheme

of the form (1.4) because of the linearity preservation property. A second order positive upwind scheme, for example, is defined by

$$\begin{cases} (\beta_i^e, \beta_{i+1}^e) = \left( \frac{a^-}{a}, \frac{a^+}{a} \right) \\ a^- = \min(a, 0) \\ a^+ = \max(a, 0) \end{cases} . \quad (1.5)$$

What happens if only the advective term is included in the definition of the element residual  $\phi^e$ ? For a steady problem one will have that

$$\phi^e = \int_{x_1^e}^{x_2^e} a \frac{\partial u}{\partial x} dx = \int_{x_1^e}^{x_2^e} \sigma dx \neq 0 ,$$

hence one can say that schemes that are  $\mathcal{LP}$  at steady state for homogeneous problems, lose this property, and hence the second order of accuracy, when applied to in-homogeneous equations, if the source term is not included in the definition of the element residual.

As a consequence of the last statement one would like to extend to the multidimensional case the upwind scheme (1.5). In 2D and 3D, equation (1.3) can be written as

$$\frac{\partial u}{\partial t} + \vec{\lambda} \cdot \nabla u = \Sigma . \quad (1.6)$$

The extension of a linearity preserving scheme to equation (1.6) can be done in the following straightforward way:

$$\phi^T = \int_T \left( \vec{\lambda} \cdot \nabla u - \Sigma \right) d\Omega \quad R_i += \beta_i^T \phi^T .$$

The problem is that most of the  $\mathcal{LP}$  schemes are linear and they are not positive (see section 2.1), hence, in presence of strong gradients of the solution, they usually give non-monotone results. Second order positive schemes do exist, but they are based on a non-linear blending between a linear  $\mathcal{LP}$  scheme and a linear first order scheme, usually the so-called N-scheme (see section 2.1). The N-scheme, being linear and positive, cannot be second order accurate, because of Godunov's theorem (see reference [1]). For this scheme the distribution coefficient

is not defined, but one can compute directly the nodal contribution of an element  $T$  as follows (see section 2.1):

$$\phi_i^N = \max \left( \frac{\vec{\lambda} \cdot \vec{n}_i}{2}, 0 \right) (u_i - u_{in}) , \quad (1.7)$$

where  $\vec{n}_i$  is the inward pointing normal to the edge (surface in 3D) in front of node  $i$  (see figure 2.2) and the state  $u_{in}$  is the so-called inflow state of element  $T$ . Note that the index  $T$  has been dropped in (1.7) to simplify the notation. More details on the schemes will be given in the next chapter, what is important to underline here is that the crucial point in the construction of a positive scheme which is  $\mathcal{LP}$  also in presence of source terms is the extension of (1.7) to non-homogeneous equations. The way in which this has been done will be explained extensively in section 3.1.1.

### 1.3 Conservative Linearization and Quasi-Linear Equations

Consider the following simple 2D scalar non-linear conservation law

$$\frac{\partial u}{\partial t} + \frac{\partial f}{\partial x} + \frac{\partial g}{\partial y} = 0 , \quad (1.8)$$

where the fluxes  $f$  and  $g$  depend in general on the unknown  $u$ . Equation (1.8) can be solved in a fully conservative way with a  $\mathcal{LP}$  scheme computing the residual in the following way:

$$\phi^T = \oint_{\partial T} \vec{\mathcal{F}} \cdot \vec{n} dl \quad R_i^+ = \beta_i^T \phi^T , \quad (1.9)$$

where  $\partial T$  is the boundary of the generic triangle  $T$  of the grid,  $\vec{\mathcal{F}} = (f, g)$  and  $\vec{n}$  is the outward pointing unit normal to  $\partial T$ . Note that

1. The integral in (1.9) can be computed very accurately by choosing the appropriate quadrature rule.
2. The distribution coefficients  $\beta_i^T$  depend usually on the jacobian

$$k_i^T = \frac{\partial f}{\partial u} n_{ix} + \frac{\partial g}{\partial v} n_{iy} , \quad (1.10)$$

where  $\vec{n}_i \equiv (n_{ix}, n_{iy})$  is the inward pointing vector normal to the edge in front of node  $i$ . It is important to underline that  $k_i^T$  for a non-linear equation is in general a function of the unknown  $u$  and that the scheme defined by (1.9) remains conservative, independently on how  $k_i^T(u)$  is computed, as long as the distribution coefficients respect the condition:

$$\sum_{j \in T} \beta_j^T = 1 .$$

The scalar  $k_i^T$  is usually called inflow parameter.

The problem with scheme (1.9) is that it is linear and hence, being  $\mathcal{LP}$ , it cannot be positive. So non-monotone solutions are obtained in presence of discontinuities. As already mentioned speaking about the discretization of the source terms, the construction of a second order scheme which is also monotone is based on a non linear blending between a second order linear  $\mathcal{LP}$  scheme, which is non-positive, with a first order positive scheme. The first order scheme usually used in the computations is an extension of the N-scheme (equation (1.7)) where the product  $\vec{\lambda} \cdot \vec{n}_i$  is substituted by the parameter  $k_i^T$  of equation (1.10) evaluated in some averaged state. The problem is that the scheme obtained in this way is conservative provided that the cell residual is computed using the quasi-linear form of equation (1.8), as follows

$$\phi^T = \sum_{j \in T} \hat{k}_j^T u_j ,$$

where  $\hat{k}_j^T$  indicates the inflow parameter evaluated in an average state  $\hat{u}^T$  such that the identity

$$\sum_{j \in T} \hat{k}_j^T u_j = \oint \vec{F} \cdot \vec{n} dl ,$$

holds at a discrete level. For example for the inviscid Burger's equation one has  $(f, g) = (\frac{u^2}{2}, u)$ , and, if linear variation of the unknown over each element is assumed, a conservative N-scheme is obtained if all the jacobians are evaluated in the average state:

$$\hat{u}^T = \frac{1}{3} \sum_{v=1,3} u_v .$$

When such a conservative linearization exists, it is usually called a Roe linearization. For the Euler equations a Roe linearization is obtained by computing the arithmetic average of the values at the vertices of an element  $T$  of the Roe parameter  $\mathbf{Z}$  given by

$$\mathbf{Z} = \sqrt{\rho} [1, u, v, H]^t ,$$

where  $\rho$  is the fluid density,  $u$  and  $v$  are the  $x$  and  $y$  velocity components and  $H$  is the total enthalpy. Since not all the systems of equations admit such a linearization one should ideally use always a contour integral for the evaluation of the flux balance of each element (equation (1.9)) in order to be conservative. An the other hand, the necessity of using the N-scheme to build a non-linear positive and  $\mathcal{LP}$  blended scheme forces to use the quasi-linear form of the equations. In the course of this project a new technique has been developed which allows to rewrite the N-scheme in a way compatible with the evaluation of the flux balance through a contour integral. In section 3.2.1 details about this new formulation of the schemes will be given together with some consequences and future developments.

## 1.4 Physical and Numerical Modeling of Two-Phase Flow

Two-Phase flows are encountered in wide variety of engineering applications ranging from power generation and conversion to biological flows. The understanding of the physics of

two-phase flows and the capability of predicting the performances of multi-phase systems are crucial to control and to design them. In the recent years, the use of the so-called Two-Fluid models to analyze two-phase flows is becoming more and more common among the scientific community. The reason for this is that these models are obtained directly from the single phase Navier-Stokes equations through an averaging process, hence their mathematical derivation is exact. Furthermore, they are able to handle real non-equilibrium effects since the mechanical and thermal variables of each phase are described as distinct fields. The most general formulation of the Two-Fluid equations for a liquid-gas system is the following [17]:

### Mass Conservation

$$\frac{\partial (\alpha_k \rho_k)}{\partial t} + \nabla \cdot (\alpha_k \rho_k \vec{u}_k) = \sigma_k^M, \quad k = l, g$$

### Momentum Conservation

$$\frac{\partial (\alpha_k \rho_k \vec{u}_k)}{\partial t} + \nabla \cdot (\alpha_k \rho_k \vec{u}_k \otimes \vec{u}_k) + \alpha_k \nabla p_k = \nabla \cdot (\alpha_k \boldsymbol{\tau}_k) + \vec{F}_k^{\text{ext}} + \vec{F}_k^{\text{int}} + \sigma_k^M \vec{u}_k^{\text{int}}, \quad k = l, g$$

### Energy Conservation

$$\begin{aligned} \frac{\partial (\alpha_k \rho_k E_k)}{\partial t} + p_k \frac{\partial \alpha_k}{\partial t} + \nabla \cdot (\alpha_k \rho_k \vec{u}_k H_k) = \nabla \cdot (\alpha_k \boldsymbol{\tau}_k \cdot \vec{u}_k) + \\ \vec{F}_k^{\text{ext}} \cdot \vec{u}_k + \vec{F}_k^{\text{int}} \cdot \vec{u}_k + \nabla \cdot (\alpha_k \mathbf{q}_k) + \sigma_k^Q + \sigma_k^M \left( h_k^{\text{int}} + \frac{\vec{u}_k^{\text{int}2}}{2} \right), \quad k = l, g \end{aligned}$$

where  $\alpha_k$  is the *void fraction* or *volume fraction* of phase  $k$ ,  $\rho_k$  its density,  $\vec{u}_k$  its velocity,  $p_k$  its pressure,  $E_k$  and  $H_k$  its total energy and enthalpy,  $\boldsymbol{\tau}_k$  its stress tensor,  $\mathbf{q}_k$  the heat flux and  $\vec{F}_k^{\text{ext}}$  an external force acting on the phase, usually the gravity force. The terms  $\sigma_k^M$ ,  $\vec{F}_k^{\text{int}}$ ,  $\sigma_k^Q$ ,  $\vec{u}_k^{\text{int}}$  and  $h_k^{\text{int}}$  represent the interface exchange of mass, momentum and heat between the phases, the interface velocity and enthalpy of phase  $k$ . All these terms come from the averaging process of the equations and must be somehow modeled. Unfortunately no unique model exists and one usually resorts to some engineering assumptions that simplify the system giving a *computable model* for the simulations. Moreover the use of high resolution upwind schemes to discretize the Two-Fluid equations turns out to be often very difficult and usually an *ad-hoc* re-formulation of the numerical methods is needed [18]. Here the work previously done at the von Karman Institute [5, 19] will be followed. In particular, the model used in the computations is the simple single pressure isentropic-mechanical equilibrium model used in [5]. In this model the flow of the two phases is assumed to be isentropic and the pressure of the two phases to be equal, hence no energy equations are solved. A strong mechanical coupling between the phases is assumed, leading to the hypothesis  $\vec{u}_l = \vec{u}_g = \vec{u}$ . Moreover the model is inviscid and of course no phase change is considered<sup>1</sup>. The final form of the equations is (see chapter 5 and appendix E for more details):

### Mass Conservation

$$\frac{\partial (\alpha_k \rho_k)}{\partial t} + \nabla \cdot (\alpha_k \rho_k \vec{u}) = 0, \quad k = l, g$$

---

<sup>1</sup>It would require the modeling of the thermal evolution of each phase and hence the hypothesis of isentropic flow should be dropped

## Mixture Momentum Conservation

$$\frac{\partial(\rho\vec{u})}{\partial t} + \nabla \cdot (\rho\vec{u} \otimes \vec{u}) + \nabla p = \vec{F}^{\text{ext}}$$

where  $\rho = \alpha_g \rho_g + \alpha_l \rho_l$  is the so-called mixture density. Note that because of the hypothesis of equal velocities, only the mixture momentum equation needs to be solved. Differently from most of the Two-Fluid models (see [5, 18, 19]) this model is always hyperbolic and well posed in the limiting single-phase cases. This will allow to perform simulations involving well known problems with strong phase separation. Note also that, although the system of equation is written in a strong conservative form, no Roe linearization exists for it. This is the typical case in which the new conservative formulation developed here should be used, but, unfortunately, because of the limited time, the space-time approach could be applied only to the same non-conservative formulation used in [5]. Note also that the two-phase flow simulations performed here are to be intended as simple tests for the new theoretical developments and not as real applications.

The outline of the report is the following: in chapter 2 the steady  $\mathcal{RD}$  schemes will be described, recalling where necessary details regarding their implementation for the solution of the Euler equations. In the same chapter the new space-time approach will be illustrated with particular attention to technical problems related to the space-time meshing. Chapter 3 will be devoted to the new theoretical developments regarding the discretization of the source terms and the treatment of conservation. Boundary conditions and time integration will be described in chapter 4 while chapter 5 will contain the results obtained on well documented steady and unsteady test-cases. The report will be closed by some conclusions and future developments.

# Chapter 2

## Residual Distribution Schemes

This chapter is devoted to the illustration of the Residual Distribution Schemes. In a first part the steady schemes will be recalled together with the most important properties that characterize them. References will be given for a more detailed description. In the second part of the chapter the space-time approach will be analyzed with some emphasis on the space-time meshing issues.

### 2.1 $\mathcal{RD}$ Schemes for Steady Hyperbolic Problems

#### 2.1.1 $\mathcal{RD}$ Schemes for Scalar Advection

Consider a simple homogeneous scalar advection equation

$$\frac{\partial u}{\partial t} + \vec{\lambda} \cdot \nabla u = 0 ;$$

discretize the 2D or 3D physical domain  $\Omega$  with an unstructured mesh composed of triangles (resp. tetrahedra) and assume that the unknown  $u$  varies linearly in space, like in the standard linear finite element method. In formulas

$$u = \sum_{i \in \Omega} N_i u_i ,$$

where  $u_i$  indicates the nodal value of the unknown and  $N_i$  is the linear tent-shaped interpolation function (see figure 2.1).

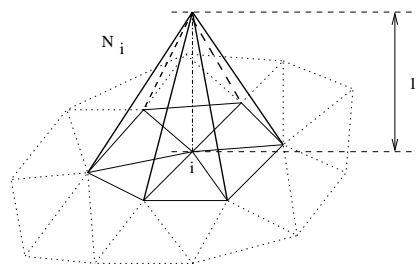


Figure 2.1: Tent-shaped interpolation function  $N_i$

The *fluctuation* or *residual* of an element  $T$  is defined as the integral of the advective fluxes, namely

$$\phi^T = \int_T \vec{\lambda} \cdot \nabla u \, d\Omega_T = - \int_T \frac{\partial u}{\partial t} \, d\Omega_T . \quad (2.1)$$

Define now the so-called *inflow parameter* of node  $j$  in cell  $T$  as the following quantity:

$$k_j^T = \frac{1}{d} \vec{\lambda} \cdot \vec{n}_j^T , \quad (2.2)$$

where  $d$  is the number of spatial dimensions and  $\vec{n}_j^T$  is the inward pointing vector, perpendicular to the edge (face in 3D) in front of node  $j$  and scaled by its length (surface in 3D), as illustrated in figure 2.2.

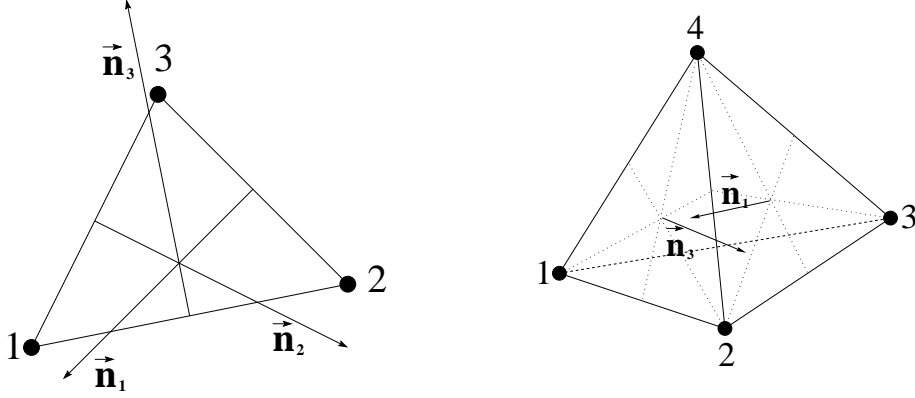


Figure 2.2: 2D and 3D grid geometry

It can be easily shown that the fluctuation  $\phi^T$  can be computed as the following weighted average of the element nodal values

$$\phi^T = \sum_{j \in T} k_j^T u_j .$$

The idea at the basis of the residual distribution schemes is that the evolution of the nodal values of the unknown is determined by a fraction of the fluctuation of each element containing that specific node. In particular, the global nodal residual is obtained by assembling the contribution coming from all the elements surrounding the node. In formulas:

$$R_i = \sum_{T \in \Delta_i} \phi_i^T = \sum_{T \in \Delta_i} \beta_i^T \phi^T = \sum_{T \in \Delta_i} \sum_{j \in T} \beta_i^T k_j^T u_j ,$$

being  $\Delta_i$  the set of elements containing node  $i$  and  $\beta_i^T$  the so-called *distribution coefficient*. Once the nodal residual is assembled, the solution can be marched forward in time until convergence to steady state is reached. A very simple update formula is obtained if explicit forward Euler time integration is used:

$$u_i^{n+1} = u_i^n - \frac{\Delta t}{S_i} R_i , \quad (2.3)$$

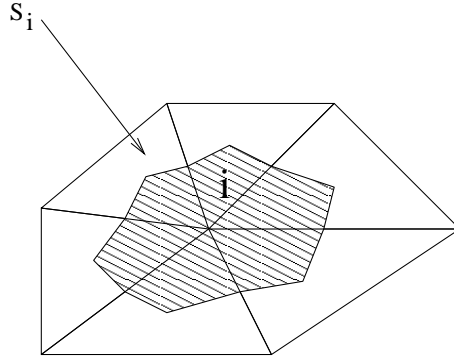


Figure 2.3: Median Dual Cell in 2D

where  $S_i$  is the area of the so-called median dual cell of node  $i$ , obtained joining the gravity centers of all the elements surrounding node  $i$  with the midpoints of the edges meeting at the node, as depicted in figure 2.3 for the 2D case. Note that:

1. For consistency and conservation the element-to-node residual contributions must respect the constraint

$$\sum_{j \in T} \phi_j^T = \phi^T \quad \rightarrow \quad \sum_{j \in T} \beta_j^T = 1. \quad (2.4)$$

2. The nodal residual can be computed using the very compact stencil of nearest neighbors, which allows an easy implicit and parallel implementation.

The design of the schemes involves the choice of the distribution coefficients or the definition of the element-to-node contribution  $\phi_j^T$ . The most important design principles are based on the following properties:

**Multidimensional Upwinding ( $\mathcal{MU}$ )** A multidimensional upwind scheme does not send any portion of the element fluctuation to upstream nodes. In formulas:

$$k_j^T < 0 \quad \rightarrow \quad \phi_j^T = 0, \quad \beta_j^T = 0. \quad (2.5)$$

**Positivity ( $\mathcal{P}$ )** The positivity property ensures that monotone solutions are always obtained. For a positive scheme the new value of the unknown  $a$  can be written as a convex sum of its old values in the surrounding nodes, i.e.

$$u_i^{n+1} = \sum c_{ij} u_j^n, \quad c_{ij} > 0. \quad (2.6)$$

For the simple update formula (2.3) condition (2.6) becomes (see reference [1]):

$$\beta_i^T k_j^T < 0, \quad \Delta t < \frac{S_i}{\sum_{T \in \Delta_i} \beta_i^T k_i^T}.$$

**Linearity Preservation ( $\mathcal{LP}$ )** A linearity preserving scheme is a scheme whose distribution coefficients are bounded. In particular for a linearity preserving scheme one has that

$$\lim_{\phi^T \rightarrow 0} \phi_j^T = \lim_{\phi^T \rightarrow 0} \beta_j^T \phi^T = 0 .$$

It can be shown [1] that a linearity preserving scheme is able to reproduce exactly steady linear solutions, hence the  $\mathcal{LP}$  property is equivalent to second order of accuracy at steady state.

A more detailed description of the properties which can be used for the design of the schemes can be found in [1]. In the same reference the proof of the extension of Godunov's theorem to the fluctuation splitting schemes can be found. The above-mentioned theorem states that *linear schemes cannot be positive and linearity preserving at the same time*. Unfortunately, most of the basic schemes are linear and hence, to have a second order positive scheme, some non-linearity must be introduced. Here we will not follow [1] where a review of some techniques to obtain non-linear second order schemes is made, but we will more closely follow the work reported in [3, 16, 20].

In particular a non-linear scheme could be defined from the following blending:

$$(\phi_i^T)^{\mathcal{P}, \mathcal{LP}} = (1 - \theta) (\phi_i^T)^{\mathcal{LP}} + \theta (\phi_i^T)^{\mathcal{P}} , \quad (2.7)$$

where the blending coefficient  $\theta$  should be defined in such a way that in correspondence of smooth solutions, where  $\phi_T \approx 0$ , one has  $\theta = 0$ , while in correspondence of strong gradients or discontinuities, one has  $\theta = 1$ . In this way the  $\mathcal{LP}$  property will be preserved by the blending, although in presence of sharp variations of the solution monotone results are guaranteed by the stabilizing contribution of the  $\mathcal{P}$  scheme. Information and details about possible choices of the blending factor and their relation with the work made in [1] can be found in [20], while in [3, 16] a review of the design principles of blended schemes for the solution of the Euler equations is made. In the course of this project the following blending factor has been used in all the computations:

$$\theta = \frac{|\phi^T|}{\sum_{j \in T} |(\phi_j^T)^{\mathcal{P}}|} . \quad (2.8)$$

It can be easily seen from definition (2.8) that at convergence, whenever one has that  $\phi_T = 0$ , the blended scheme defined by (2.7) becomes actually the second order  $\mathcal{LP}$  scheme. On the other hand, although there is no formal proof of the positivity of such a blended scheme, numerical evidence indicates that this property actually holds.

## Definition of the Schemes

Now that the basic ideas behind the fluctuation splitting schemes have been given, it remains to specify how the element residual is actually distributed. The number of schemes that have been designed and tested in the past years is relatively large. For an overview one can refer to [1]. Here the following schemes have been used<sup>1</sup>:

---

<sup>1</sup> $\mathcal{LP}$  stands for Linearity Preserving,  $\mathcal{P}$  stands for Positive,  $\mathcal{MU}$  stands for Multidimensional Upwind and  $\mathcal{L}$  stands for Linear

**LDA scheme** ( $\mathcal{LP}, \mathcal{L}, \mathcal{MU}$ ) The LDA scheme is defined by

$$\phi_i^{LDA} = \beta_i^{LDA} \phi_i^T \quad , \quad \beta_i^{LDA} = \frac{k_i^+}{\sum_{j \in T} k_j^+} \quad ,$$

with  $k_i^+ = \max(k_i^T, 0)$ . Note that the index  $T$  has been dropped where non-necessary, to simplify the notation.

**N scheme** ( $\mathcal{P}, \mathcal{L}, \mathcal{MU}$ ) The N scheme is defined by

$$\phi_i^N = k_i^+ (u_i - u_{in}^T) \quad , \quad u_{in} = \frac{\sum_{j \in T} k_j^- u_j}{\sum_{j \in T} k_j^-} \quad ,$$

with  $k_i^- = \min(k_i^T, 0)$ . The state  $u_{in}^T$  is the so-called *inflow state*.

**B scheme** ( $\mathcal{P}, \mathcal{LP}, \mathcal{MU}$ ) The blended scheme is defined by

$$\phi_i^B = (1 - \theta) \phi_i^{LDA} + \theta \phi_i^N \quad , \quad \theta = \frac{|\phi_i^T|}{\sum_{j \in T} |\phi_j^N|} \quad .$$

A geometrical interpretation of the schemes is available in [1, 2], while the proof of their properties can be found in [1, 20].

## Remarks

1. The schemes defined above of course are applied also to non-linear equations where either  $\vec{\lambda} = \vec{\lambda}(u)$  or  $\vec{\lambda} = \nabla_u \vec{\mathcal{F}}$ , being  $\nabla_u = (\vec{1}_x, \vec{1}_y, \vec{1}_z) \frac{\partial}{\partial u}$ , and  $\vec{\mathcal{F}}$  is a vector of conservative fluxes. In the last case, in particular, the use of the N scheme is possible only if a linearization of the jacobians such that

$$\oint_{\partial T} \vec{\mathcal{F}} \cdot \vec{n} \, dl = \int_T \nabla \cdot \vec{\mathcal{F}} \, d\Omega = \Omega_T \widehat{\nabla_u \vec{\mathcal{F}}} \cdot \nabla u \quad ,$$

is available. Note that in the last equation  $\nabla u$  is constant, since  $u$  is assumed to be linear, and  $\vec{n}$  is the outward pointing unit normal to the boundary of  $T$ . The reason of this is that the distribution coefficient of the N scheme cannot be explicitly defined and hence a truly conservative formulation of the type

$$\phi_i^T = \beta_i^T \oint_{\partial T} \vec{\mathcal{F}} \cdot \vec{n} \, dl$$

cannot be used.

2. The positivity of the N scheme (and hence of the B scheme) is obtained, in case of a time marching procedure like (2.3), under the time-step constraint:

$$\Delta t < \frac{S_i}{\sum_{T \in \Delta_i} k_i^+} \quad . \quad (2.9)$$

Of course this is not true anymore if an implicit time integration strategy is used<sup>2</sup>.

---

<sup>2</sup>In any case, the steady state solution  $u^*$  satisfies  $\min_{j \in \Delta_i} u_j^* < u_i^* < \max_{j \in \Delta_i} u_j^*$

## 2.1.2 Matrix Schemes for Hyperbolic Systems

Consider the hyperbolic system

$$\frac{\partial U}{\partial t} + \sum_{i=1}^d A_i \frac{\partial U}{\partial x_i}, \quad (2.10)$$

where  $U$  is the vector of the unknown,  $d$  is the number of space dimensions and the  $A_i$ 's are constant matrices such that  $\sum_{i=1}^d A_i \xi_i$  is diagonalizable with real eigenvalues and real and independent eigenvectors for every  $\vec{\xi} \equiv (\xi_1, \dots, \xi_d)$  in  $\mathbf{R}^d$ . In order to solve system (2.10) discretize the space domain  $\Omega$  with an unstructured grid and assume that the vector  $U$  varies linearly in space, namely

$$U = \sum_{i \in \Omega} N_i U_i, \quad (2.11)$$

where  $U_i$  represents the value of the unknown at node  $i$  and the  $N_i$ 's are the Galerkin tent shaped linear test function (see figure 2.1). Define the residual of an element  $T$  (triangle in 2D and tetrahedron in 3D) as

$$\Phi^T = \int_T \sum_{i=1}^d A_i \frac{\partial U}{\partial x_i} d\Omega = - \int_T \frac{\partial U}{\partial t} d\Omega.$$

For the hypotheses made on the matrices  $A_i$ , it is possible to define the following multidimensional generalizations of the inflow parameters (2.2) and of their sign:

$$K_j^T = \frac{1}{d} \sum_{i=1}^d A_i n_i^j, \quad K_j^\pm = R_j \Lambda_j^\pm L_j, \quad (2.12)$$

being  $\vec{n}^j$  the vector normal to the edge (face in 3D) in front of node  $j$  and scaled by its length (resp. surface),  $R_j$  and  $L_j$  the matrices of the right and left eigenvectors of  $K_j^T$ ,  $\Lambda^+ = \mathbf{diag}_{k=1, \dots, d} [\max(\lambda_k, 0)]$  and  $\Lambda^- = \mathbf{diag}_{k=1, \dots, d} [\min(\lambda_k, 0)]$  with  $\lambda_k$   $k$ -th eigenvalue of  $K_j^T$ . Thanks to the hypothesis of linear variation of  $U$ , it can be easily shown that the cell residual can be computed as

$$\Phi^T = \sum_{j \in T} K_j^T U_j. \quad (2.13)$$

Exactly like in the scalar case, the global nodal residual is obtained assembling portions of the fluctuation of the elements surrounding it. In formulas:

$$\Phi_i^T = \mathbf{B}_i^T \Phi^T, \quad \mathbf{R}_i = \sum_{T \in \Delta_i} \mathbf{B}_i^T \Phi^T = \sum_{T \in \Delta_i} \sum_{j \in T} \mathbf{B}_i^T K_j^T U_j. \quad (2.14)$$

The matrix  $\mathbf{B}_i^T$  is called the *distribution matrix*, and the class of schemes defined by (2.14) are usually referred to as the *matrix schemes*.

Once the nodal residual has been assembled, the solution can be marched forward in time toward the steady state. If explicit forward Euler time integration is used, one has:

$$U_i^{n+1} = U_i^n - \frac{\Delta t}{S_i} \mathbf{R}_i = U_i^n - \frac{\Delta t}{S_i} \sum_{T \in \Delta_i} \sum_{j \in T} \mathbf{B}_i^T K_j^T U_j. \quad (2.15)$$

As in the scalar case, the properties of the method are fully determined by the distribution criterion. For an optimal design of the schemes is then of primary importance to be able to generalize properties of the scalar distribution to the system case. The set of criteria on which the choice of the distribution criteria is based are the following:

**Multidimensional Upwinding ( $\mathcal{MU}$ )** In the case of hyperbolic systems the  $\mathcal{MU}$  property must be intended in a *characteristic* sense. The idea is that if the eigenvalue  $\lambda_k^i$  of  $K_i^T$  is negative, then the  $k$ -th characteristic field of node  $i$  is not updated. Mathematically this implies that the nodal residual must be locally proportional to the positive part of  $K_i^T$ , namely

$$\Phi_i^T = \mathbf{B}_i^T \Phi^T \propto K_i^+ .$$

**Positivity ( $\mathcal{P}$ )** Following [2], in order to generalize this property to the matrix schemes, the update formula (2.15) is rewritten as

$$\frac{U_i^{n+1} - U_i^n}{\Delta t} S_i + \sum_m C_{lm} (U_l^n - U_m^n) = 0 .$$

The scheme will be said positive if all the matrices  $C_{lm}$  are non-negative, i.e. their eigenvalues are all positive or zero.

**Linearity Preservation ( $\mathcal{LP}$ )** Simply as in the scalar case, a scheme is said to be linearity preserving if

$$\lim_{\Phi^T \rightarrow 0} \Phi_j^T = \lim_{\Phi^T \rightarrow 0} \mathbf{B}_j^T \Phi^T = 0 .$$

**Invariance for Similarity Transformations ( $\mathcal{IST}$ )** This is a very important property for the design of the schemes. Consider a set of variables  $W$ , defined by

$$\partial W = \frac{\partial W}{\partial U} \partial U ,$$

the invariance property requires that the following relation between the residual expressed in the old set of variables and the one expressed in the new one:

$$R_i^U = \frac{\partial U}{\partial W} R_i^W .$$

From the last equation one deduces for the distribution matrices [2]

$$\mathbf{B}_i^W = \frac{\partial W}{\partial U} \mathbf{B}_i^U \frac{\partial U}{\partial W} , \quad \mathbf{B}_i^U = \frac{\partial U}{\partial W} \mathbf{B}_i^W \frac{\partial W}{\partial U} .$$

The importance of this property is that it allows to compute the residual in the set of variables more convenient<sup>3</sup> and then transform it to the original variables, being sure that the final result will be exactly the as as if the residual were computed directly in the original set of variables.

---

<sup>3</sup>For example the one that symmetrizes the matrices of the system or reduces their entries

Like in the scalar case, no linear schemes that have both the  $\mathcal{LP}$  property and the  $\mathcal{P}$  property exist. In this work, a second order positive scheme has been used, which is defined by the following non-linear blending of a linear positive scheme and a linear linearity preserving scheme:

$$(\Phi_i^T)^{\mathcal{P}, \mathcal{LP}} = (I - \Theta) (\Phi_i^T)^{\mathcal{LP}} + \Theta (\Phi_i^T)^{\mathcal{P}} \quad , \quad \Theta_{ij} = \delta_{ij} \frac{|\Phi_T]_j|}{\sum_{k \in T} |[(\Phi_i^T)^{\mathcal{P}}]_j|}$$

Also for this scheme, like for the one defined by (2.7) and (2.8), no analytical proof of positivity is available. Strong numerical evidence is available, though, that it produces monotone solutions also in presence of strong discontinuities.

A different class of blended schemes have been recently developed by Abgrall for the solution of the Euler equations, that are designed using a more analytical approach. The reader interested can refer to reference [16].

### Definition of the Schemes

In this project, the schemes used in the computations are a generalization of the scalar schemes presented in the previous section. For a more extensive overview on the matrix schemes, one can refer to [1, 2].

**Matrix LDA scheme ( $\mathcal{LP}$ ,  $\mathcal{L}$ ,  $\mathcal{IST}$ ,  $\mathcal{MU}$ )** The matrix LDA scheme is a formal generalization of its scalar counterpart. Its distribution matrix is given by:

$$\mathbf{B}_i^{LDA} = K_i^+ \left( \sum_{j \in T} K_j^+ \right)^{-1} . \quad (2.16)$$

**Matrix N scheme ( $\mathcal{P}$ ,  $\mathcal{L}$ ,  $\mathcal{IST}$ ,  $\mathcal{MU}$ )** Like the matrix LDA scheme, the matrix N scheme is obtained through a formal extension of its scalar counterpart. Its element-to-node contribution is defined as:

$$\Phi_i^N = K_i^+ (U_i - U_{in}) \quad , \quad U_{in} = \left( \sum_{j \in T} K_j^- \right)^{-1} \sum_{j \in T} K_j^- U_j \quad (2.17)$$

**Matrix B scheme ( $\mathcal{P}$ ,  $\mathcal{LP}$ ,  $\mathcal{IST}$ ,  $\mathcal{MU}$ )** The matrix blended scheme used in the course of this project is defined by:

$$\Phi_i^B = (I - \Theta) \Phi_i^{LDA} + \Theta \Phi_i^N \quad , \quad \Theta_{ij} = \delta_{ij} \frac{|\Phi_T]_j|}{\sum_{k \in T} |[\Phi_i^N]_j|}$$

For a more detailed description of the properties of the matrix schemes and for the proof of some of their properties, the interested reader can refer to [1, 2, 3, 16].

## Remarks

1. Of course the matrix schemes can be used to solve a system of non-linear equations. In particular they are used to solve the system of the Euler equations which, in 3D, can be written in the form

$$\frac{\partial U}{\partial t} + \frac{\partial F(U)}{\partial x} + \frac{\partial G(U)}{\partial y} + \frac{\partial H(U)}{\partial z} = 0, \quad (2.18)$$

where  $U$  is the vector of the conserved variables  $U = [\rho, \rho u, \rho v, \rho w, \rho E]^t$  and the vector  $\vec{F} = (F, G, H)$  represents the conservative fluxes. Although for the LDA scheme system (2.18) can be solved fully conservatively computing the cell residual as

$$\Phi^T = \oint_{\partial T} \vec{F} \cdot \vec{n} \, dl, \quad (2.19)$$

one usually rewrites the equations in a quasi-linear form, since the use of the N scheme, and hence of the B scheme, obliges to do that. In particular, the cell fluctuation is still computed using (2.13) where now

$$K_i^T = \hat{K}_i^T = \frac{\partial F(\hat{U})}{\partial U} n_{ix} + \frac{\partial G(\hat{U})}{\partial U} n_{iy} + \frac{\partial H(\hat{U})}{\partial U} n_{iz},$$

where, for conservation, the average state  $\hat{U}$  has to be the Roe average obtained through the computation of the conserved variables in correspondence of the arithmetic average of the nodal values of Roe's parameter vector

$$\mathbf{Z} = \sqrt{\rho} [1, u, v, w, H]^t. \quad (2.20)$$

In the framework of residual distribution schemes, this linearization is known as the Struijs-Deconinck-Roe linearization. For the proof of the fact that the relation

$$\oint_{\partial T} \vec{F} \cdot \vec{n} \, dl = \sum_{j \in T} \hat{K}_j^T U_j$$

actually holds at the discrete level, one can refer to [1, 2, 3, 21]. Here it is of primary importance to underline that not for all the system of conservation laws a Roe-type linearization exist. As a consequence, the possibility to compute  $\Phi^T$  using (2.19), even in conjunction with the N scheme, turns out to be very appealing.

2. For the matrix N scheme, of course, one cannot write down directly the positivity condition, but has to take into account the characteristic formulation of the Multidimensional Upwinding. In particular, by doing it, one ends up with the time-step restriction<sup>5</sup>

$$\Delta t < \frac{S_i}{\sum_{T \in \Delta_i} \max_{k=1, \dots, N_{equations}} (\lambda_k^+)_T},$$

where  $N_{equations}$  is the number of equations, and hence of eigenvalues, of the system.

---

<sup>4</sup>Density, x-momentum, y-momentum, z-momentum, Total Energy

<sup>5</sup>Of course not if an implicit time-integration strategy is used

3. From (2.16) and (2.17) it can be seen that to use the matrix LDA scheme and the matrix N scheme one needs to perform the matrix inversion  $(\sum_{j \in T} K_j^\pm)^{-1}$ . In [2] the proof of the existence of these inverse matrices is given for any hyperbolic system. Some trouble in their computation actually arises for stagnant flows where, in fact, the matrices  $\sum_{j \in T} K_j^\pm$  are singular. Although Abgrall has proven that the  $\mathcal{RD}$  schemes remain well-defined in these degenerate cases, special care is required to treat the singularity.

The informations given on the  $\mathcal{RD}$  schemes as applied to steady problems, far from being complete, are only intended to serve as a basis for the description of the space-time schemes of next section. Additional notions on the general schemes can be found in the references given.

## 2.2 Space-Time $\mathcal{RD}$ Schemes

In this second part of the chapter the new space-time  $\mathcal{RD}$  approach will be described. During the last year, two different space-time formulations of the fluctuation splitting schemes have been developed. Although based on the very same idea, the two approaches differ in the way the extension of the steady schemes to the space-time domain is obtained. In particular, while the group of the von Karman Institute [14, 15] has focused its attention to the use of linear space-time elements, Abgrall and co-workers [13] make use of prismatic elements. The approach used here is the same of [14, 15].

### 2.2.1 Unsteady Scalar Conservation Laws

Consider a scalar hyperbolic conservation law in  $d$  spatial dimensions over the spatial and temporal domain  $\Omega = \Omega_S \times [0, t_{max}]$ :

$$\frac{\partial u}{\partial t} + \nabla \vec{\mathcal{G}} = 0 \quad , \quad \forall (\vec{x}, t) \in \Omega \quad , \quad (2.21)$$

where  $u(\vec{x}, t)$  is the conserved quantity and  $\vec{\mathcal{G}}(u)$  the corresponding flux function. Define the jacobian of the flux function  $\vec{\lambda} = \partial \vec{\mathcal{G}} / \partial u$ . Equation (2.21) can be reformulated in the following space-time approach:

$$\vec{\nabla} \cdot \vec{\mathcal{F}} = 0 \quad , \quad \boldsymbol{\lambda} \cdot \vec{\nabla} u = 0 \quad , \quad (2.22)$$

where  $\vec{\nabla}$  denotes the space-time operator  $\vec{\nabla} = (\nabla, \partial/\partial t)$ ,  $\vec{\mathcal{F}}$  is the space-time flux function  $\vec{\mathcal{F}} = \vec{\mathcal{G}} + u\hat{t}$ , being  $\hat{t}$  the versor of the time coordinate direction, and  $\boldsymbol{\lambda} = \vec{\lambda} + \hat{t}$  is the space-time jacobian of  $\vec{\mathcal{F}}$ .

The basic idea behind the space-time  $\mathcal{RD}$  approach is to solve equation (2.22) using the standard fluctuation splitting schemes, described in the first part of this chapter, on a discretization of the space-time domain  $\Omega$  made of triangles and tetrahedra in one and two spatial dimensions respectively. In particular the discretization procedure will be exactly the same as the one described for the solution of steady problems, except for the fact that now the fluctuation (2.1) will be computed with an integral over a space-time element and the inflow parameter (2.2) will be computed as

$$k_i^T = \frac{1}{d+1} \boldsymbol{\lambda} \cdot \vec{n}_i^T = \frac{1}{d+1} \left( \vec{\lambda} \cdot \vec{n}_i^S + n_i^t \right) \quad , \quad (2.23)$$

where  $d$  is the number of spatial dimensions,  $\vec{n}_i^S$  is the vector containing the spatial coordinates of the vector normal to the boundary face (or edge) which stands in front of node  $i$  in the space-time element  $T$  and scaled by its surface (rep. length), while  $n_i^t$  is the temporal component of this vector that, for the space-time meshes considered in this project (see next subsection on the space-time geometry), is equal to half of the length of the initial 1D segment if  $d = 1$  and one third of the surface of the base triangle in the initial spatial grid, if  $d = 2$ .

Note that if a standard continuous space-time finite element method was to be used, this would lead to a coupling of all the points in the space-time grid, which would be very expensive. This is the reason why most of the finite element methods are based on a continuous representation

in space of the variable, but discontinuous in time. The strength of the space-time  $\mathcal{RD}$  approach lays in the fact that the  $\mathcal{MU}$  property allows to decouple the space-time solution on temporal slabs of thickness  $\Delta t$ , maintaining a continuous variable representation in time. Hence, advancing of one time-step  $\Delta t$ , is equivalent to solve the steady problem (2.22) on the space-time slice  $\Omega_S \times \Delta t$ . Note that if  $d$  is the number of spatial dimensions, the schemes will be applied to a domain with dimension  $d + 1$ . It turns out that if the space-time grid is built in a proper way, the multidimensional upwinding guarantees the temporal decoupling of the space-time slabs automatically. As a consequence, the choice of the grid geometry is of fundamental importance. The next subsection will be fully devoted to the description of the type of space-time grids used for the computations within this project. More details can be found in [14, 15, 22]

### Space-Time Grid Geometry

The grids used in this project contain three levels of nodes and two levels of elements in the time direction, for a reason that will be clear after the analysis that follows.

Denote with  $t_n$ ,  $t_{n+1/2}$  and  $t_{n+1}$  the temporal coordinates of the nodes in the first, second and third layer respectively. For clearness they will be referred to as the *past*, *intermediate* and *future* nodes. Denote with  $\Delta t_1 = t_{n+1/2} - t_n$  the time difference between intermediate and past nodes and with  $\Delta t_2 = t_{n+1} - t_{n+1/2}$  the time difference between future and intermediate nodes. The global time-step is controlled by the parameter  $Q$  defined by

$$Q = \frac{\Delta t_2}{\Delta t_1} . \quad (2.24)$$

**Space-Time Grid for 1D Problems** Given an initial discretization of the 1D space domain, the type of space-time grids that can be built are shown in figure 2.4. It can be seen that both configuration have some nodes in the intermediate level which are staggered in space, in particular they are located in correspondence of the midpoints of the segments in the past level. Note also that in both cases the second layer is obtained just by mirroring the first one and stretching it according to the factor  $Q$ . The configuration on the left is of course computationally more convenient and, in fact, is the one actually used in the simulations. The interest in the second configuration comes from the fact that it can be easily generalized to the case of two spatial dimensions. In order to derive the condition for the decoupling of the space-time slab, one can focus only on the first layer<sup>6</sup>. In particular note that both configurations have a similar topology, in particular they both have two types of triangles: one with two nodes in the past layer and one in the intermediate and the other with two intermediate nodes and one past node. From now on the discussion will focus on the grid configuration on the left in figure 2.4, but, given the similar topology of the two configurations, the same analysis can be applied to configuration on the right in the same picture. Denote with  $E1$  the first type of triangle and with  $E2$  the second one as indicated in figure 2.5. In order to decouple the solution, allowing time marching, no residual must be sent to the past. Using the

---

<sup>6</sup>The decoupling of the past level from the intermediate one already guarantees the preservation of the past solution, allowing a true time-marching solution procedure

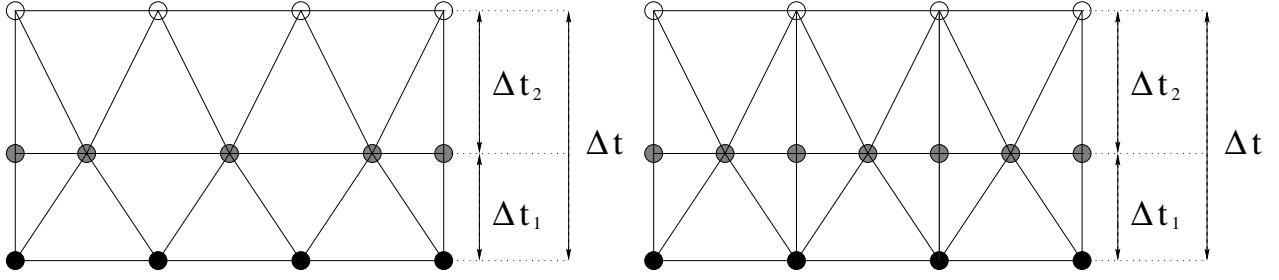


Figure 2.4: Space-time mesh in 1D. Nodes at levels  $n$ ,  $n + 1/2$  and  $n + 1$  are labeled by black, gray and empty circles, respectively.

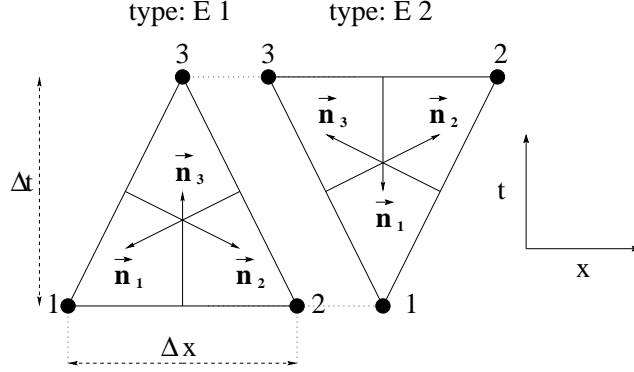


Figure 2.5: Basic triangular elements in the first layer

$\mathcal{MU}$  property, we can obtain this by choosing  $\Delta t_1$  such that the upwind parameter  $k_i^T$  (equation (2.2)) is negative for all the past nodes. In order to do this, it is useful to recall that in one spatial dimension the quasi-linear form of equation (2.22) reduces to

$$(\lambda, 1) \cdot \left( \frac{\partial u}{\partial x}, \frac{\partial u}{\partial t} \right) = 0 \quad , \quad \lambda = \frac{\partial \mathcal{G}}{\partial u} .$$

With the local numbering of figure 2.5, one has that for the triangle of type  $E2$

$$k_1^{E2} = -\frac{\Delta x}{2} < 0 ,$$

for the only past node 1. Hence triangles of this type impose no constraints on the choice of  $\Delta t_1$ . On the other hand for the  $E1$  triangle one has

$$\begin{cases} \vec{n}_1 = \left( -\Delta t_1, \frac{\Delta x}{2} \right) & \rightarrow & k_1^{E1} = -\frac{\lambda \Delta t_1}{2} - \frac{\Delta x}{4} \\ \vec{n}_2 = \left( \Delta t_1, \frac{\Delta x}{2} \right) & \rightarrow & k_2^{E1} = \frac{\lambda \Delta t_1}{2} - \frac{\Delta x}{4} \\ \vec{n}_3 = \left( 0, \frac{\Delta x}{2} \right) & \rightarrow & k_3^{E1} = \frac{\Delta x}{2} \end{cases} ,$$

hence to be sure that both  $k_1^{E1}$  and  $k_2^{E1}$  are negative, one has to respect the constraint:

$$\left( \frac{\Delta t_1 |\lambda|}{\Delta x} \right)_{E1} = CFL_1 \leq \frac{1}{2} . \quad (2.25)$$

Condition (2.25) is called the *local past shield* ( $\mathcal{LPS}$ ) condition, since it guarantees that past nodes are protected from any information coming from the future.

The global time-step  $\Delta t_1$  is computed as the minimum of the local ones, i.e.

$$\Delta t_1 = \min_{E \in E_1} CFL_1 \left( \frac{\Delta x}{2|\lambda|} \right)_E .$$

Obviously the intermediate nodes can be coupled with both past and future nodes, hence there are no restrictions on  $\Delta t_2$  in the second layer. This enables to march in time with arbitrarily large time-steps, keeping unconditional stability if a positive  $\mathcal{RD}$  scheme is used. The global time-step can be written in fact as

$$\Delta t = \Delta t_1 + \Delta t_2 = (1 + Q) \Delta t_1 = (1 + Q) \min_{E \in E_1} CFL_1 \left( \frac{\Delta x}{2|\lambda|} \right)_E ,$$

while for the global  $CFL$  number one gets:

$$CFL = \frac{|\lambda|\Delta t}{\Delta x} = \frac{1 + Q}{2} CFL_1 . \quad (2.26)$$

From equation (2.26) and from the freedom in the choice of the stretching parameter  $Q$ , one deduces that the two layers space-time schemes allow to have very large  $CFL$  numbers, which can be very useful, especially if the spatial grid contains highly refined regions.

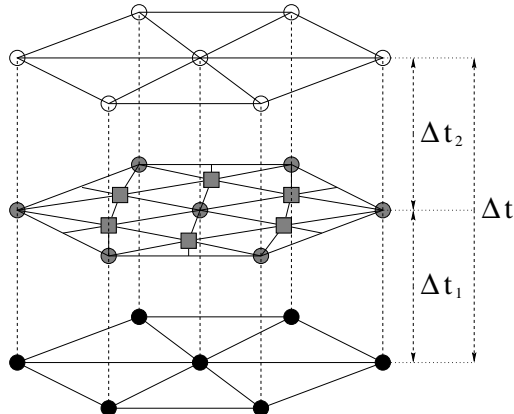


Figure 2.6: Space-time mesh in 2D. Nodes at levels  $n, n + 1/2$  and  $n + 1$  are respectively labeled by black, gray and empty circles. Squares indicate intermediate nodes positioned in the centroid of the triangles of the level  $n$  spatial mesh.

**Space-Time Grid for 2D Problems** As in 1D, starting from a 2D spatial grid, different configurations are possible. The one used here is probably the simplest, although also the more expensive. A similar, but more convenient, approach can be found in [22]. The grid used is a generalization of the right configuration of figure 2.4. A global view

of the nodes configuration can be seen in figure 2.6. As can be seen from this picture, every node in the initial spatial mesh is also present in the intermediate level where new nodes are added in correspondence of the centroids of the triangles of the initial grid. Also in the 2D case the second layer is obtained just by mirroring the first one and stretching it by the stretching factor  $Q$  (2.24). The first layer is composed by three types of elements: the first has three past nodes and one intermediate node, the second has two past nodes and two intermediate ones and the third has one node in the past level and three in the intermediate level. The three element types are highlighted in figure 2.7, where they have been labeled as  $E1$ ,  $E2$  and  $E3$  respectively.

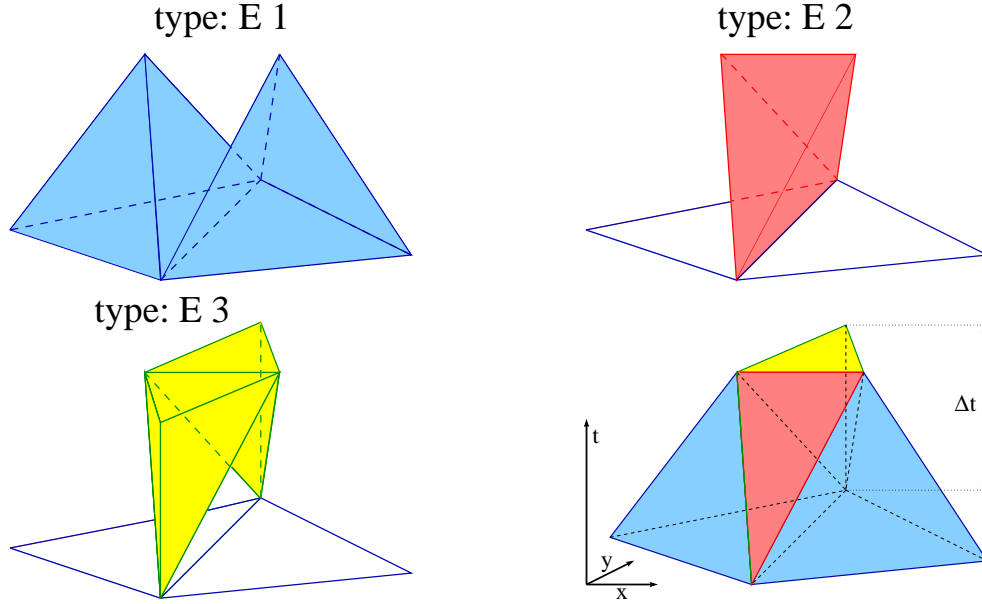


Figure 2.7: Basic tetrahedra used to build the first layer of the space-time mesh in two space dimensions, and schematic view of the mesh.

The  $\mathcal{LPS}$  condition (2.25) can be derived for this case following exactly the same procedure of the 1D case. For the mesh in figure 2.7 the element  $E3$  gives no constraints on  $\Delta t_1$ , while two different conditions are obtained for elements  $E1$  and  $E2$ . Using the notation of figure 2.8 one has (see [14]):

$$\begin{aligned} \max_{j=1,2,3} \left( \frac{k_j^{+,E1} \Delta t_1}{n_j^t} \right) < 1 \\ \max_{j=1,2} \left( \frac{k_j^{+,E2} \Delta t_1}{n_j^t} \right) < 1 \end{aligned} \quad , \quad (2.27)$$

where  $n_j^t$  is the temporal component of the vector normal to the face in front of node  $j$  and scaled by its surface,  $k_j^{+,E1} = \max(0, k_j^{E1})$ ,  $k_j^{+,E2} = \max(0, k_j^{E2})$ ,  $k_j^{E1} = \vec{\lambda} \cdot \vec{n}_j^{123} / 2$  is the spatial inflow parameter corresponding to the base triangle<sup>7</sup> and  $k_j^{E2}$  is the spatial

---

<sup>7</sup> $n_j^{123}$  is the normal to the base edge in front of node  $j$  and scaled by its length,  $\vec{\lambda}$  is the jacobian  $\partial \vec{Q} / \partial u$  (equation (2.21))

inflow parameter of node  $j$  in the triangle  $\Delta^{j34}$  obtained projecting nodes 3 and 4 on the past level and joining them to node  $j$ <sup>8</sup>.

Conditions (2.27) have to be respected simultaneously in all the tetrahedra of type  $E1$  and  $E2$ , hence  $\Delta t_1$  is finally computed as

$$\Delta t_1 = CFL_1 \min \left[ \min_{E \in E_1} \left( \frac{1}{\max_{j=1,2,3} \frac{k_j^{+,E1}}{n_j^t}} \right), \min_{E \in E_2} \left( \frac{1}{\max_{j=1,2} \frac{k_j^{+,E2}}{n_j^t}} \right) \right],$$

with  $CFL_1 < 1$ . The global time-step is then computed as  $\Delta t = (1 + Q)\Delta t_1$  and, like in the 1D case, from the freedom in the choice of the  $Q$  factor, one deduces that arbitrarily large  $CFL$  numbers can be taken retaining unconditional stability if a positive scheme is used.

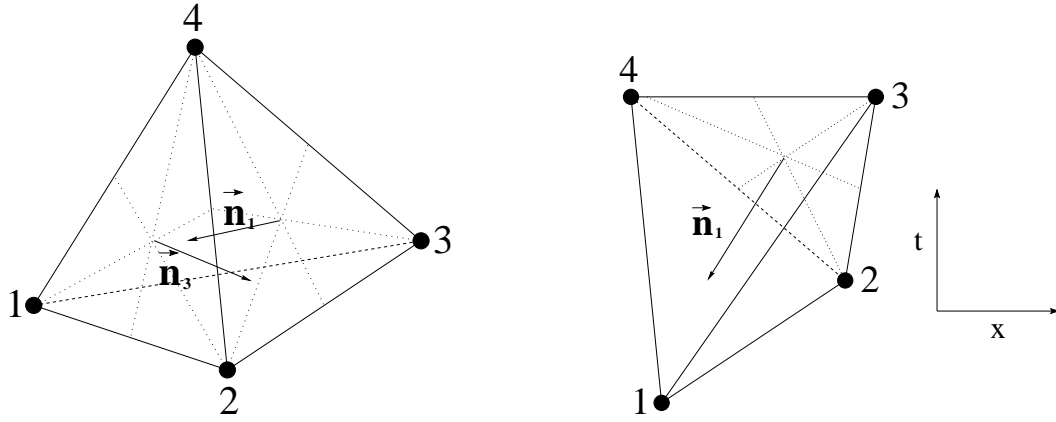


Figure 2.8: Elementary tetrahedra of types E1 (left) and E2 (right)

Once the space-time grid has been built, equation (2.22) is solved using one of the schemes described in section 2.1. In particular, the solution of the algebraic equations obtained applying the schemes to one space-time slab is obtained marching in a pseudo-time  $\tau$  exactly like the solution of steady problems is usually obtained marching in time. This means that, once the space-time residual has been assembled, the solution will be updated until convergence in pseudo-time is reached for the present space-time slab. For example, using forward Euler time integration, one ends with

$$u_i^{\tau+1} = u_i^\tau - \frac{\Delta \tau}{S_i} R_i,$$

where  $S_i$  is the surface of the space-time median dual cell of node  $i$  and  $R_i$  is a space-time residual.

---

<sup>8</sup> $k_j^{E2} = \vec{\lambda} \cdot \vec{n}_j^{j34} / 2$ , with  $\vec{n}_j^{j34}$  normal to the projected edge  $\bar{34}$  in the past plane and pointing toward node  $j$ .  $\vec{\lambda}$  is the same as in the previous footnote

## 2.2.2 Unsteady Hyperbolic Systems

Consider now a hyperbolic system of conservation laws

$$\frac{\partial U}{\partial t} + \nabla \cdot \vec{\mathcal{G}} = 0 \quad , \quad \forall (\vec{x}, t) \in \Omega = \Omega_S \times [0, t_{max}] \quad , \quad (2.28)$$

where  $U$  is the vector of conserved variables and  $\vec{\mathcal{G}}(U)$  is the vector of the conservative fluxes. Equation (2.28) can also be written in the quasi-linear form

$$\frac{\partial U}{\partial t} + \sum_{k=1, \dots, d} \frac{\partial \mathcal{G}^k}{\partial U} \frac{\partial U}{\partial x_k} \quad ,$$

where  $d$  is the number of spatial dimensions and the matrices  $\partial \mathcal{G}^k / \partial U$  are the jacobian of the fluxes. Like in the scalar case, the space-time formulation of the system can be introduced, which, with the notation of equation (2.22), reads

$$\vec{\nabla} \cdot \vec{\mathcal{F}} = 0 \quad , \quad \left( \frac{\partial \mathcal{G}^1}{\partial U}, \dots, \frac{\partial \mathcal{G}^d}{\partial U}, I \right) \cdot \vec{\nabla} U \quad , \quad (2.29)$$

where  $\vec{\mathcal{F}} = \vec{\mathcal{G}} + U\hat{t}$  is the space-time flux vector and  $I$  is the identity matrix. The unsteady solution of system (2.28) is then obtained marching in time by solving at each time-step the space-time steady problem (2.29) using standard  $\mathcal{RD}$  matrix schemes on a space-time slab  $\Omega_S \times \Delta t$ . Of course also in the system case the fluctuation of an element is computed as a space-time integral, while the inflow matrices  $K_i^T$  (2.12) are substituted by

$$K_i^T = \frac{1}{d+1} \left( \sum_{k=1, \dots, d} \frac{\partial \mathcal{G}^k}{\partial U} n_i^{x_k} + I n_i^t \right) \quad , \quad (2.30)$$

where  $n_i^{x_k}$  is the  $k$ -th spatial component of the vector normal to the boundary face in front of node  $i$  in the space-time element  $T$ , scaled by its surface (or length if  $d = 1$ ) and  $n_i^t$  is its temporal component. The matrices with sign  $K_i^\pm$  can be computed straightforwardly as [14] (see equation 2.12):

$$K_i^\pm = \frac{1}{d+1} R_i (\Lambda_i^\pm + I n_i^t) L_i \quad , \quad (2.31)$$

where  $\Lambda_i$ ,  $R_i$  and  $L_i$  come from the eigenvalue decomposition of  $\sum_{k=1, \dots, d} \frac{\partial \mathcal{G}^k}{\partial U} n_i^{x_k}$ .

Of course, care must be taken in building the space-time grid and in imposing the  $\mathcal{LPS}$  condition. In particular in the 1D case, the  $|\lambda|$  of equation (2.25) is substituted by the largest wave-speed associated to the characteristic form of the equations<sup>9</sup>, while in the 2D case the spatial inflow parameters in equation (2.27) are replaced by the largest positive eigenvalue of the corresponding spatial inflow matrix. Also in the case of the solution of a system of equations, the solution of one time-step is obtained by marching in a pseudo-time according to

$$U_i^{\tau+1} = U_i^\tau - \frac{\Delta \tau}{S_i} \mathbf{R}_i \quad .$$

---

<sup>9</sup>Largest eigenvalue of the jacobians. For example for the Euler equations one uses  $\|\vec{u}\| + a$ , where  $\vec{u}$  is the velocity vector and  $a$  is the speed of sound

## Remarks

1. Although not explicitly proven, the use of a linearity preserving space-time scheme should guarantee second order of accuracy in space and time. This is a consequence of the fact that the  $\mathcal{LP}$  property guarantees that solutions which are linear in space-time will be reproduced exactly.
2. The pseudo-time marching procedure, if done in an explicit way, imposes a constraint on the  $\Delta\tau$ . As for steady computations, in fact, the N matrix scheme will be positive under the condition

$$\Delta\tau < \frac{S_i}{\sum_{T \in \Delta_i} \max_{k=1, \dots, N_{equations}} (\lambda_k^+)_T},$$

where now  $\lambda_k$  is an eigenvalue of the inflow matrix  $K_i^T$  of equation (2.30)<sup>10</sup>.

3. As noted in [14], once a Roe-type linearization is known for the system, it can be used also for the space-time jacobians. In particular, in all the Euler computation performed in the course of this project, the Struijs-Deconinck-Roe linearization has been used to linearize the jacobians on each space-time element.
4. Equation (2.31) shows one of the important properties of the space-time schemes: as already remarked, the use of the LDA matrix scheme and of the N matrix scheme requires the inversion of the matrices  $\sum_{j \in T} K_j^\pm$ . Even if the spatial jacobians of the system are singular in stagnation regions, the space-time inflow matrices are still regular there because of the additional term  $In_i^t$ . This allows to simulate flows with large regions of zero or vanishing velocity without any problem. Examples of such computations can be found in [14].

---

<sup>10</sup>In the scalar case condition (2.9) must be applied, using the space-time inflow parameter (2.23)

# Chapter 3

## New Developments for $\mathcal{RD}$ Schemes: Source Terms and Conservation

This chapter describes the new theoretical results obtained in the course of this project. First the consistent source term discretization used in the computations will be described, showing its consistency with the 1D approach pioneered by Roe [23] and later further developed (see [24, 25] for example) and its extension to second order accuracy. In the second half of the chapter it will be shown how the same idea used to discretize the source terms can be used to build a first order conservative N scheme which does not need any Roe-type linearization. Possible developments of the approach are also discussed. It is important to stress the generality of the theory described in this chapter that remains valid whenever  $\mathcal{RD}$  schemes are used to solve a hyperbolic system of equations.

### 3.1 $\mathcal{RD}$ Schemes for Non-Homogeneous Equations

Most of the discretization techniques currently used nowadays for the approximation of the convective fluxes of systems of conservation laws are based on some kind of upwinding procedure. The use of such kind of discretization finds its reasons in arguments of physical nature, related to the way informations propagate in the flow, and of numerical nature, related to the stability of the methods. Although at a first glance not physically evident, the upwinding should be extended also to the source terms eventually present in the equations. The reason for this is intuitively explained by the following simple 1D example: consider the scalar problem

$$\frac{\partial u}{\partial t} + a \frac{\partial u}{\partial x} = \sigma \quad , \quad a > 0 .$$

Discretizing this equation with the upwind scheme given in the introduction (equation (1.5)) one obtains at steady state

$$a (u_i - u_{i-1}) - \frac{\Delta x}{2} (\sigma_i + \sigma_{i-1}) = 0 ,$$

which is clearly a centered, and hence second order accurate, approximation of the steady equation around the cell-center  $i + 1/2$ . A more detailed and convincing analysis can be

found in [24, 25], where the authors show the enhanced accuracy and consistency obtained by upwinding the source terms on a variety of 1D and 2D problems.

In the context of  $\mathcal{RD}$  schemes, the crucial point is how to derive a multidimensional extension of the first order upwind scheme. This extension has been obtained within this project and is described in the next section.

### 3.1.1 An N-Scheme for Non-Homogeneous Equations

Consider the scalar non-homogeneous problem

$$\frac{\partial u}{\partial t} + \vec{\lambda} \cdot \nabla u = \Sigma . \quad (3.1)$$

For simplicity we will focus on the problem of finding a steady solution of (3.1) with given boundary conditions using a fully multidimensional upwind discretization. Define the following parameter:

$$i_j^+ = \begin{cases} \frac{k_j^+}{k_j^T} & \text{if } k_j^T \neq 0 \\ 0 & \text{if } k_j^T = 0 \end{cases} ,$$

where  $k_j^T$  and  $k_j^+$  are the inflow parameter (2.2) and its positive part. Define the *reduced value* of the source term in the node  $i$  on the element  $T$ ,  $\Sigma_i^*$ , as its nodal value multiplied by the surface (volume in 3D) of the element  $\Omega_T$  and divided by its number of vertices, namely

$$\Sigma_i^* = \frac{\Omega_T}{d+1} \Sigma_i .$$

Compute the source term fluctuation

$$\phi^\Sigma = \int_T \Sigma \, d\Omega , \quad (3.2)$$

where the last integral can be approximated with any quadrature rule.

#### PROPOSITION 1

The multidimensional upwind  $\mathcal{RD}$  scheme defined by

$$\phi_j^{N,\Sigma} = i_j^+ [k_j^T (u_j - u_{in}) + \Sigma_j^* - \Sigma_{in}^*] , \quad (3.3)$$

with

$$\Sigma_{in}^* = \frac{\sum_{l \in T} i_l^+ \Sigma_l^* + \phi^\Sigma}{\sum_{l \in T} i_l^+} , \quad u_{in} = \frac{\sum_{l \in T} k_l^- u_l}{\sum_{l \in T} k_l^-} ,$$

is fully conservative, in the sense that

$$\sum_{l \in T} \phi_l^{N,\Sigma} = \int_T (\vec{\lambda} \cdot \nabla u - \Sigma) \, d\Omega = \phi^T - \phi^\Sigma .$$

**Proof:** The proof of this proposition is obtained in a straightforward way just by computing the sum of the element-to-node contributions:

$$\begin{aligned} \sum_{l \in T} \phi_l^{N, \Sigma} &= \sum_{l \in T} i_l^+ [k_l^T (u_l - u_{in})] + \sum_{l \in T} i_l^+ (\Sigma_l^* - \Sigma_{in}^*) = \\ &= \sum_{l \in T} k_l^+ (u_l - u_{in}) + \sum_{l \in T} i_l^+ \Sigma_l^* - \sum_{l \in T} i_l^+ \Sigma_l^* - \phi^\Sigma = \phi^T - \phi^\Sigma . \end{aligned}$$

Note that different definitions of the reduced value of the source term could be used, but it must be kept in mind that the residual sent to each node must respect the following dimensional scaling

$$i_j^+ (\Sigma_j^* - \Sigma_{in}^*) \propto \int_T \Sigma \, d\Omega \quad \rightarrow \quad \Sigma_j^* \propto \Omega_T \Sigma .$$

In this project, the source term fluctuation (3.2) has been computed with the second order accurate formula

$$\phi^\Sigma = \frac{\Omega_T}{d+1} \sum_{l \in T} \Sigma_l = \sum_{l \in T} \Sigma_l^* ,$$

and hence

$$\Sigma_{in}^* = \frac{\sum_{l \in T} (i_l^+ + 1) \Sigma_l^*}{\sum_{l \in T} i_l^+} .$$

### Extension to Systems

The matrix version of scheme (3.3) is obtained formally extending all the definition given for the scalar case. In particular, given the hyperbolic non-homogeneous system

$$\frac{\partial U}{\partial t} + \sum_{k=1, \dots, d} A_k \frac{\partial U}{\partial x_k} = S ,$$

define the matrix parameter

$$I_j^+ = K_j^+ (K_j^T)^{-1} ,$$

and the local nodal reduced value of the source term

$$S_i^* = \frac{\Omega_T}{d+1} S_i .$$

Compute the source term fluctuation

$$\Phi^S = \int_T S \, d\Omega .$$

#### PROPOSITION 2

*The multidimensional upwind matrix scheme defined by*

$$\Phi_j^{N, S} = I_j^+ [K_j^T (U_j - U_{in}) + S_j^* - S_{in}^*] , \quad (3.4)$$

with

$$S_{in}^* = \left( \sum_{l \in T} I_l^+ \right)^{-1} \left( \sum_{l \in T} I_l^+ S_l^* + \Phi^S \right) , \quad U_{in} = \left( \sum_{l \in T} K_l^- \right)^{-1} \left( \sum_{l \in T} K_l^- U_l \right)$$

is fully conservative, in the sense that

$$\sum_{l \in T} \Phi_l^{N,S} = \int_T \left( \sum_{k=1, \dots, d} A_k \frac{\partial U}{\partial x_k} - S \right) d\Omega = \Phi^T - \Phi^S .$$

**Proof:** Proceeding like in the scalar case:

$$\begin{aligned} \sum_{l \in T} \Phi_l^{N,\Sigma} &= \sum_{l \in T} I_l^+ [K_l^T (U_l - U_{in})] + \sum_{l \in T} I_l^+ (S_l^* - S_{in}^*) = \\ &= \sum_{l \in T} K_l^+ (U_l - U_{in}) + \sum_{l \in T} I_l^+ S_l^* - \sum_{l \in T} I_l^+ S_l^* - \Phi^S = \phi^T - \phi^S . \end{aligned}$$

In all the computations made the source term residual has been computed as

$$\phi^S = \frac{\Omega_T}{d+1} \sum_{l \in T} S_l = \sum_{l \in T} S_l^* , \quad (3.5)$$

so that

$$S_{in}^* = \left( \sum_{l \in T} I_l^+ \right)^{-1} \sum_{l \in T} (I_l^+ + I) S_l^* ,$$

where  $I$  is the identity matrix.

Results obtained on steady and unsteady tests with the matrix version of the scheme are reported in chapter 5, showing the robustness and reliability of the approach.

### 3.1.2 A $\mathcal{LP}$ Scheme for Non-Homogeneous Equations

Once the first order monotone  $\mathcal{RD}$  scheme to discretize non-homogeneous equations is available, a second order non-linear blended scheme can be easily built as follows

**Scalar Non-Homogeneous Equations :**

$$\phi_i^B = (1 - \theta) \beta_i^{\mathcal{LP}} (\phi^T - \phi^\Sigma) + \theta \phi_i^{N,\Sigma} , \quad \theta = \frac{|\phi^T - \phi^\Sigma|}{\sum_{l \in T} |\phi_l^{N,\Sigma}|} .$$

**Non-Homogeneous Hyperbolic Systems :**

$$\Phi_i^B = (I - \Theta) \mathbf{B}_i^{\mathcal{LP}} (\Phi^T - \Phi^S) + \Theta \Phi_i^{N,S} , \quad \Theta_{ij} = \delta_{ij} \frac{|\Phi^T - \Phi^S|_j}{\sum_{l \in T} |\Phi_l^{N,S}|_j} .$$

Accurate results obtained on several inviscid problems are reported in chapter 5. Note that in all the computations involving the B scheme, the LDA scheme has been used as  $\mathcal{LP}$  scheme.

## Remarks

1. Although not explicitly done here, the proof of the existence of the matrices  $\left(\sum_{j \in T} K_j^+\right)^{-1}$  for any hyperbolic system, reported in [2], can be naturally extended to the matrices  $\left(\sum_{j \in T} I_j^+\right)^{-1}$  needed for the application of scheme (3.4).
2. Consider a 1D system of conservation laws written in quasi-linear form

$$\frac{\partial U}{\partial t} + A(U) \frac{\partial U}{\partial x} = S .$$

Referring to figure A.1 the 1D first order upwind finite volume scheme used in [24] and in [25] can be written for a uniformly spaced 1D grid as

$$\frac{U_i^{n+1} - U_i^n}{\Delta t} \Delta x = -(\mathbf{F}_{i+1/2}^n - \mathbf{F}_{i-1/2}^n) + \Sigma_{i+1/2}^n + \Sigma_{i-1/2}^n , \quad (3.6)$$

where the numerical flux functions  $\mathbf{F}_{i\pm 1/2}^n$  are given by

$$\mathbf{F}_{i\pm 1/2}^n = \hat{A}_{i\pm 1/2} \frac{U_i + U_{i\pm 1}}{2} - \frac{1}{2} |\hat{A}_{i\pm 1/2}| \Delta U_{i\pm 1/2} ,$$

being  $\hat{A}_{i\pm 1/2}$  the matrix  $A$  computed in some average state. The source term contribution coming from the interface  $i \pm 1/2$  is computed as

$$\Sigma_{i\pm 1/2}^n = \frac{I \mp \mathbf{sgn}(\hat{A}_{i\pm 1/2})}{2} S_{i\pm 1/2}^n \Delta x , \quad (3.7)$$

being  $S_{i\pm 1/2}^n$  the value of the source term at the interface, usually approximated with second order of accuracy as

$$S_{i\pm 1/2}^n = \frac{S_i^n + S_{i\pm 1}^n}{2} .$$

The matrix  $\mathbf{sgn}(\hat{A}_{i\pm 1/2})$  in equation (3.7) is the *sign* of matrix  $\hat{A}_{i\pm 1/2}$ , defined by

$$|\hat{A}_{i\pm 1/2}| = \mathbf{sgn}(\hat{A}_{i\pm 1/2}) \hat{A}_{i\pm 1/2} \quad , \quad |\hat{A}_{i\pm 1/2}| \mathbf{sgn}(\hat{A}_{i\pm 1/2}) = \hat{A}_{i\pm 1/2} , \quad (3.8)$$

and computed as

$$\mathbf{sgn}(\hat{A}_{i\pm 1/2}) = \hat{R}_{i\pm 1/2} \mathbf{sgn}(\hat{\Lambda}_{i\pm 1/2}) \hat{L}_{i\pm 1/2} \quad , \quad \mathbf{sgn}(\hat{\Lambda}_{i\pm 1/2}) = \mathbf{diag}_{k=1, \dots, N_{equations}} \left( \frac{\lambda_k}{|\lambda_k|} \right) ,$$

where  $\hat{R}_{i\pm 1/2}$  and  $\hat{L}_{i\pm 1/2}$  are the matrices of the right and left eigenvectors of  $\hat{A}_{i\pm 1/2}$  and  $\lambda_k$  is the  $k$ -th eigenvalue of  $\hat{A}_{i\pm 1/2}$ .

A very interesting property of scheme (3.4) is given by the following

### PROPOSITION 3

*The  $N$  scheme defined by (3.4) is consistent with the  $\mathcal{RD}$  formulation of the 1D finite volume scheme (3.6).*

The proof is reported in appendix A.

## 3.2 A New Approach for Conservative $\mathcal{RD}$ Schemes Based on the N Scheme

As already said, in the framework of the  $\mathcal{RD}$  schemes, the use of the first order positive N scheme is of crucial importance to handle discontinuous solutions retaining monotonicity. Unfortunately this is possible only if a conservative Roe-type linearization is available for the jacobian of the fluxes, which is not always the case. In this section an alternative formulation of the scheme based on the same idea used for the upwind discretization of the source terms will be presented. This new formulation relies on a computation of the integral of the fluxes over an element through a contour integration and is always conservative. A particular section will be devoted to the description of the integration rules used to perform the contour integration and also to the future developments that the technique could allow.

### 3.2.1 A Conservative N-Scheme for General Systems of Conservation Laws

Consider the following general non-linear system of conservation laws in  $d$  space dimensions

$$\frac{\partial U}{\partial t} + \nabla \cdot \vec{\mathcal{F}} = 0, \quad (3.9)$$

where  $\vec{\mathcal{F}} = (\vec{F}_{x_1}, \dots, \vec{F}_{x_d})$  is the vector of the conservative fluxes. Define the fluctuation of an element  $T$  as the following integral

$$\Phi^T = \oint_{\partial T} \vec{\mathcal{F}} \cdot \vec{n} \, dl, \quad (3.10)$$

where  $\vec{n}$  is the unit vector normal to  $\partial T$  and pointing outside of  $T$ . The following property can be proven

**PROPOSITION 4**

*The  $\mathcal{RD}$  scheme defined by*

$$\Phi_i^{N,c} = K_i^+ (U_i - U_c) \quad , \quad U_c = \left( \sum_{j \in T} K_j^+ \right)^{-1} \left( \sum_{j \in T} K_j^+ U_j - \Phi^T \right), \quad (3.11)$$

*is conservative independently of the type of average used to compute the cell jacobian  $K_i^T$ , i.e.*

$$\sum_{j \in T} \Phi_j^{N,c} = \oint_{\partial T} \vec{\mathcal{F}} \cdot \vec{n} \, dl.$$

**Proof:** The proof of the last proposition is easily obtained as follows

$$\sum_{j \in T} \Phi_j^{N,c} = \sum_{j \in T} K_j^+ U_j - \left( \sum_{j \in T} K_j^+ \right) U_c = \sum_{j \in T} K_j^+ U_j - \sum_{j \in T} K_j^+ U_j + \Phi^T = \Phi^T,$$

and hence

$$\sum_{j \in T} \Phi_j^{N,c} = \oint_{\partial T} \vec{\mathcal{F}} \cdot \vec{n} \, dl.$$

### 3.2.2 A Conservative $\mathcal{LP}$ Scheme for General Systems of Conservation Laws

Once a first order monotone conservative scheme is in hand, the second order monotone non-linear blended scheme can be built as

$$\Phi_i^B = (I - \Theta)\mathbf{B}_i^{\mathcal{LP}}\Phi^T + \Theta\Phi_i^{N,c} \quad , \quad \Theta_{ij} = \delta_{ij} \frac{|\Phi_j^T|}{\sum_{l \in T} |(\Phi_l^{N,c})_j|} \quad ,$$

where  $\Phi^T$  is computed according to (3.10). In all the computations performed here  $\mathbf{B}_i^{\mathcal{LP}} = \mathbf{B}_i^{LDA}$ .

Chapter 5 contains a number of steady and unsteady tests performed to verify the properties of the new conservative formulation. In particular, several computations have been performed on problems involving the solution of the Euler equations in order to compare the new treatment of conservation with the more classic one based on the use of the Struijs-Deconinck-Roe linearization. Although the *conservative* N scheme (3.11) cannot be proven to be positive, it has shown monotone perfect shock capturing properties, at least in the tests considered here. Unfortunately, because of time restrictions, the new technique has not been tried for the Two-Phase flow model, for which the same non-conservative formulation used in [5] as been adopted.

### 3.2.3 Contour Integration

In order to have a conservative computation of the fluxes, an appropriate quadrature rule must be used to approximate integral (3.10). In this work two different formulas have been used: a second order formula (Trapezium rule) and a third order one based on Simpson's rule. In particular consider an element  $T$  whose nodes are locally numbered from zero to  $w$ , where  $w$  is the number of coordinates<sup>1</sup>. The integral of the fluxes can be computed using the second order trapezium rule as follows:

$$\oint_{\partial T} \vec{\mathcal{F}} \cdot \vec{n} \, dl = \sum_{s \in \partial T} \sum_{i \in s} \frac{1}{w} \vec{\mathcal{F}}_i \cdot \vec{n}_s \quad ,$$

where  $i$  is a vertex belonging to the side  $s$  of  $\partial T$  and  $\vec{n}_s$  is the vector normal to side  $s$ , pointing outwards and scaled by its surface (length if  $T$  is a triangle). One can easily show that

$$\oint_{\partial T} \vec{\mathcal{F}} \cdot \vec{n} \, dl = \sum_{j \in T} \frac{1}{w} \vec{\mathcal{F}}_j \cdot \vec{n}_j^T \quad , \quad (3.12)$$

where  $\vec{n}_j^T$  is the vector normal to the side in front of node  $j$  of element  $T$ , pointing inwards and scaled by the surface (length if  $T$  is a triangle) of the side. The proof of this statement is reported in appendix C.1.

---

<sup>1</sup>If  $d$  is the number of space dimensions, one has  $w = d$  for a steady computation, while  $w = d + 1$  for a space-time computation

Unfortunately, the use of a second order formula turned out to be not enough for some computations. In particular, the steady Euler tests involving a bow-shock blew-up even with the  $N^c$  scheme. The reason for this can be probably found in the fact that the computation of the integral of the fluxes through a Roe averaging process of the jacobians yields an exact formula, at the discrete level, assuming that the Roe parameter (see equation (2.20)) varies linearly over an element. The question is then what is the quadrature formula that one should use to match the accuracy obtained through Roe averaging. The formula used in this work to overcome the difficulties in the bow shock computations is based on Simpson's rule. For the steady 2D case it reads:

$$\oint_{\partial T} \vec{\mathcal{F}} \cdot \vec{n} \, dl = \sum_{s \in \partial T} \left( \frac{1}{6} \vec{\mathcal{F}}_{i_s^1} + \frac{2}{3} \vec{\mathcal{F}}_{m_s} + \frac{1}{6} \vec{\mathcal{F}}_{i_s^2} \right) \cdot \vec{n}_s ,$$

where  $i_s^1$  and  $i_s^2$  are the extrema of the edge  $s$ , while  $m_s$  is its middle-point. It can be easily shown that the previous formula can be rewritten as (see appendix C.2)

$$\oint_{\partial T} \vec{\mathcal{F}} \cdot \vec{n} \, dl = \sum_{j \in T} \frac{1}{3} \left( \frac{1}{2} \vec{\mathcal{F}}_j - 2 \vec{\mathcal{F}}_{m_j} \right) \cdot \vec{n}_j^T , \quad (3.13)$$

where now  $m_j$  is the middle-point of the edge in front of node  $j$  in  $T$  and  $\vec{n}_j^T$  is the same of (3.12). The use of the last formula allowed to run steady simulations involving strong curved shocks, but still the results are not fully satisfactory. The use of more accurate formulas of the Gaussian type is probably one of the solutions to be investigated. Note that in order to use formula (3.13) a proper way of evaluating the flux vector in the middle-point of the edges must be found. Here different possibilities have been tried, but the best results have been obtained with

$$\vec{\mathcal{F}}_{m_j} = \vec{\mathcal{F}}(U_{m_j}) = \vec{\mathcal{F}} \left( \frac{U_i + U_k}{2} \right) ,$$

where  $i$  and  $k$  are the two nodes belonging to  $T$  different from  $j$  and  $U$  is the vector of conservative variables.

Finally in all the steady computations only Simpson's rule has been used, while the trapezium rule was used in all the unsteady problems considered, where the additional diffusion due to the space-time approach (see chapter 5) seemed to guarantee monotone solutions even with the second order formula. As a matter of fact for both steady and unsteady computations the use of higher order formulas will be a *must* if strong and non-uniform discontinuities have to be handled.

## Remarks

1. The possibility of using averaged states different from the Roe one, even if it exists for the system we are interested to solve, gives the possibility to choose the one that possibly improves the resolution of certain features of the flow. For example for the Euler equations the number of possibilities is very large<sup>2</sup> and an investigation of this

---

<sup>2</sup>Averaged Conservative Variables, Averaged Primitive Variables, Averaged Entropy (or Symmetrizing) Variables, Averaged Characteristic Variables etc.

aspect has to be done in the future. Here for reasons of efficiency and simplicity, a simple arithmetic average of the primitive variables has been used to linearize the jacobians

2. The new approach allows in principle to evaluate the fluxes with any accuracy, if the appropriate integration formula is adopted. Hence one could think of designing higher order  $\mathcal{RD}$  schemes based on a quadratic or even cubic representation of the variables. Although some attempts in this direction have been already made [27], the way in which the cell residual should be distributed is at the moment an open question.
3. An important issue, when performing computations with systems, is to be able to compute the nodal residual in the set of variables more convenient. This is allowed for the traditional schemes by the  $\mathcal{IST}$  property (see section 2.1.2). In appendix B the proof of the following important proposition is given

PROPOSITION 5

*The schemes defined by equations (3.4) and (3.11) are  $\mathcal{IST}$ .*

4. It can be easily proven that the traditional formulation of the N scheme based on the Deconinck-Struijs-Roe linearization can be obtained as a special case of the new treatment of conservation proposed here. In order to do this, denote with  $\hat{K}_i^T$  the inflow matrix evaluated in the Roe state of the element  $T$  and set  $\Phi^T = \sum_{j \in T} \hat{K}_j^T U_j$  in equation (3.11). Recalling the definition of  $U_{in}$  given in equation (2.17), one can write:

$$\begin{aligned}
 U_c = \left( \sum_{j \in T} \hat{K}_j^+ \right)^{-1} \sum_{j \in T} (\hat{K}_j^+ - \hat{K}_j^T) U_j = \\
 - \left( \sum_{j \in T} \hat{K}_j^+ \right)^{-1} \sum_{j \in T} \hat{K}_j^- U_j = \left( \sum_{j \in T} \hat{K}_j^- \right)^{-1} \sum_{j \in T} \hat{K}_j^- U_j = U_{in} . \quad (3.14)
 \end{aligned}$$

Note that the relation  $K_j^T = K_j^+ + K_j^-$  has been used in the last equation. As a consequence of equation (3.14), the new N scheme reduces to the original one if the Deconinck-Struijs-Roe linearization is used and if the cell fluctuation  $\Phi^T$  is computed using the quasi-linear formulation of the system. Hence, the new approach is more general.



# Chapter 4

## Boundary Conditions and Time Integration

This is the last chapter describing the theoretical aspects related to the computations performed within the project. The first section will give all the details on the type of boundary conditions used in the simulations, in particular the *characteristics-based* approach used for wall, sub-sonic inlet and sub-sonic outlet boundary treatment will be analyzed. In the second part, the simple time-stepping procedure implemented will be briefly recalled.

### 4.1 Characteristics-Based B.C.s

Given a hyperbolic system of conservation laws, it is known that for well-posedness of the problem the number of physical conditions to be imposed at each boundary of the spatial domain  $\Omega$ , depends on the number of characteristics that locally enter  $\Omega$  [28]. In particular each in-going wave is associated to a positive eigenvalue  $\lambda_j$  of the jacobian

$$C = \sum_{k=1, \dots, d} \frac{\partial \vec{\mathcal{F}}_k}{\partial U} n_{x_k} ,$$

evaluated at the boundary  $\partial\Omega$  (see sketch on the left in figure 4.1). Recall that  $\partial \vec{\mathcal{F}}_k / \partial U$  is the jacobian matrix of the  $k$ -th component of the vector of the fluxes and  $U$  is the vector of conserved variables. The vector  $\vec{n}_\Omega = (n_{x_1}, \dots, n_{x_d})$  is the unit vector locally orthogonal to the boundary  $\partial\Omega$ , pointing inside  $\Omega$ . For the systems of equations considered in this project, the eigenvalues of  $C$  can be written, without any loss of generality, as follows:

$$\begin{aligned} \lambda_1 &= \vec{u} \cdot \vec{n}_\Omega \\ \lambda_2 &= \vec{u} \cdot \vec{n}_\Omega \\ \lambda_3 &= \vec{u} \cdot \vec{n}_\Omega + a \\ \lambda_4 &= \vec{u} \cdot \vec{n}_\Omega - a \end{aligned} ,$$

where  $a$  is the local value of the speed of sound and  $\vec{u}$  is the velocity vector. Depending on the sign of these eigenvalues, different configurations can be encountered. From a physical point of view, they can be classified in

**Supersonic Inlet**  $\vec{u} \cdot \vec{n}_\Omega > 0$  and  $|\vec{u} \cdot \vec{n}_\Omega| > a$ : all the eigenvalues are positive, hence all the characteristics enter the domain. Four conditions must be imposed

**Supersonic Outlet**  $\vec{u} \cdot \vec{n}_\Omega < 0$  and  $|\vec{u} \cdot \vec{n}_\Omega| > a$ : all the eigenvalues are negative, hence all the characteristics leave the domain. No conditions have to be imposed.

**Subsonic Inlet**  $\vec{u} \cdot \vec{n}_\Omega > 0$ , but  $|\vec{u} \cdot \vec{n}_\Omega| < a$ : there are three waves going in the domain, while one wave is leaving it. Three conditions Must be imposed.

**Subsonic Outlet**  $\vec{u} \cdot \vec{n}_\Omega < 0$ , but  $|\vec{u} \cdot \vec{n}_\Omega| < a$ : there are three waves going out of the domain, while one wave is entering it. Only one condition can be imposed.

**Wall**  $\vec{u} \cdot \vec{n}_\Omega = 0$ : two eigenvalues are zero, hence the correspondent characteristics are locally parallel to the boundary. No conditions can be imposed for these waves. One condition has to be set for the wave associated to the only positive eigenvalue  $\lambda_3 = a$ .

The right picture in figure 4.1 summarizes the five situations listed above.

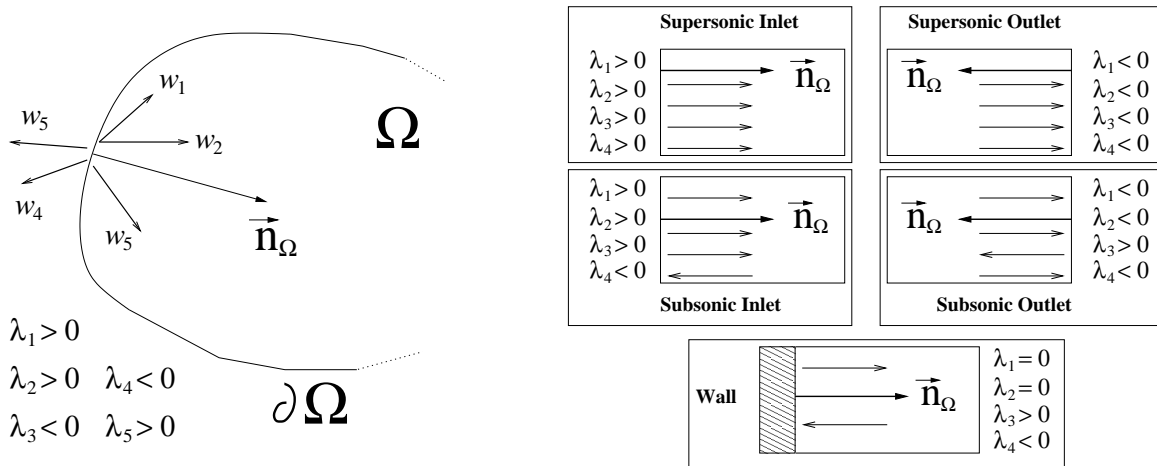


Figure 4.1: In-going and outgoing waves at the boundaries and boundary conditions

From the computational point of view, one would like to translate the informations coming from the local wave propagation phenomena described by the system, in algebraic equations to couple with the equations obtained from the spatial discretization. In particular, since the  $\mathcal{RD}$  discretization technique used in this project relies on the knowledge of the nodal values of the unknowns, a procedure that allows to impose the boundary conditions directly on the nodes belonging to the boundaries of the computational domain seems to be the most indicated. The technique actually used here is based on what in [1] has been called strong formulation of the boundary conditions.

Consider then the boundary node  $i$  of figure 4.2. The unit vector locally normal to the computational boundary  $\partial\Omega$  can be computed as the average of the inward pointing vectors

normal to the edges of the boundary triangles containing  $i$ ,  $T_1$  and  $T_2$ , weighted by their length, i.e.

$$\vec{n}_i = \frac{\vec{n}_{T_1} + \vec{n}_{T_2}}{\|\vec{n}_{T_1}\| + \|\vec{n}_{T_2}\|},$$

where  $\|\vec{n}_{T_j}\|$  is equal to the length of the boundary edge of  $T_j$ . Once the components of the normal  $\vec{n}_i$  are known, one is able to compute the jacobian  $C_i = \sum_k (\partial \vec{\mathcal{F}}_k / \partial U) n_{ix_k}$  and its eigenvalue decomposition. The procedure used to impose the boundary conditions is then the following

1. Compute the inner nodal residual  $\mathbf{R}_i$ , coming from the spatial discretization;
2. Compute the provisional increment of the nodal variables associated to the inner residual:

$$\delta U_i = -\tilde{\mathbf{R}}_i$$

3. Compute the corrective boundary residual  $\mathbf{R}_i^*$  as the linear combination

$$\mathbf{R}_i^* = \sum_{\lambda_k^i > 0} \beta^k \mathbf{r}^k, \quad (4.1)$$

where  $\mathbf{r}^k$  is the right eigenvector associated to the positive eigenvalue of the jacobian  $C_i$ ,  $\lambda_k^i$  and the coefficients  $\beta^k$  are computed analytically such that the solution computed as

$$U_i^{n+1} = U_i^n + \delta U_i - \mathbf{R}_i^*$$

verifies the required boundary condition;

4. Update the nodal residual with the corrective residual  $\mathbf{R}_i^*$  before the nodal update.

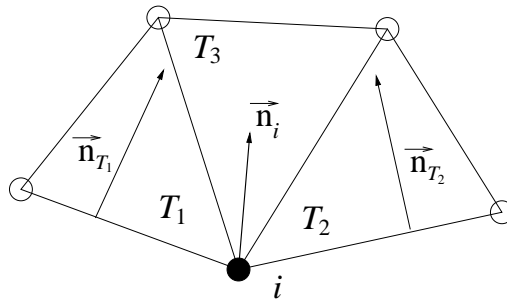


Figure 4.2: Nodal normal at the boundary

Note that the provisional residual  $\tilde{\mathbf{R}}_i$  is actually the spatial residual  $\mathbf{R}_i$  (see equation (2.15)) multiplied by the factor  $\Delta t/S_i$ . The same multiplication factor must be taken into account in the computation of the  $\beta^k$  coefficients to avoid inconsistencies. Generally speaking the conditions that can be imposed with this technique can be chosen freely, keeping in mind that their number cannot be greater than the number of positive eigenvalues  $\lambda_k^i$ . The conditions imposed in the computations performed can be summarized as follows

**Supersonic Outlet** Since there are no positive eigenvalues, no conditions are imposed, i.e. the new solution in nodes belonging to a boundary through which there is a supersonic outlet is determined only from the inner residual.

**Supersonic Inlet** All the characteristics enter the domain, hence the whole vector of variables should be imposed. Practically speaking this condition can be imposed simply by setting to zero the nodal residual.

**Wall** In inviscid computations only the impermeability condition can be guaranteed at the wall, i.e. one can require that  $\vec{u}_i \cdot \vec{n}_i = 0$  in the new solution. Note that in this case only one positive eigenvalue is present and hence only one coefficient  $\beta^w$  is needed in (4.1). Defining the normal velocity  $u_\perp = u_i n_{ix} + v_i n_{iy}$ , the coefficient can be computed imposing one of the two following conditions:

$$u_\perp^{n+1} = 0 \quad \text{or} \quad \Delta u_\perp^{n+1} = u_\perp^{n+1} - u_\perp^n = 0 .$$

The computation of  $\beta^w$  is reported in appendix D for the 2D Euler equations.

**Subsonic Outlet** Also in this case only one condition can be imposed. In particular, only one coefficient  $\beta^a$  is needed in (4.1) and it is computed requiring

$$p_i^{n+1} = p_{out}(t^{n+1}) \quad \text{or} \quad \Delta p_i = p_i^{n+1} - p_i^n = 0 ,$$

where  $p$  is the pressure and  $p_{out}(t)$  is a given function of the time. Also for this condition the full computation of  $\beta^a$  is given in appendix D for the 1D Euler equations.

**Subsonic Inlet** In this case three conditions must be imposed, and hence three coefficients  $\beta^1$ ,  $\beta^2$  and  $\beta^3$  are needed in (4.1). Of course several possibilities are available for the choice of the physical conditions to set. Here, for the Euler equations, following [1, 2], the conditions chosen are given by

$$\Delta T_{0i} = T_{0i}^{n+1} - T_{0i}^n = 0 , \quad \Delta p_{0i} = p_{0i}^{n+1} - p_{0i}^n = 0 , \quad \Delta \left( \frac{v_i}{u_i} \right) = \left( \frac{v_i}{u_i} \right)^{n+1} - \left( \frac{v_i}{u_i} \right)^n = 0$$

or

$$T_{0i}^{n+1} = T_0^* , \quad \tilde{p}_{0i}^{n+1} = \tilde{p}_0^* , \quad \Delta \left( \frac{v_i}{u_i} \right) = \left( \frac{v_i}{u_i} \right)^{n+1} - \left( \frac{v_i}{u_i} \right)^n = 0 ,$$

where  $T_0$  is the total temperature,  $p_0$  is the total pressure,  $v/u$  is the tangent of the flow angle,  $T_0^*$  is a prescribed value of the total temperature and  $\tilde{p}_0$  is a modified total pressure defined by

$$\tilde{p}_0 = \left( \frac{p_0}{p} \right)^{-\frac{1}{\gamma}} p_0 ,$$

being  $\gamma = 1.4$  the ratio of the specific heat coefficients. A different set of conditions have been implemented for the Two-Phase flow model (see chapter 5):

$$\Delta(\rho u)_i = (\rho u)_i^{n+1} - (\rho u)_i^n = 0 , \quad \Delta(\rho v)_i = (\rho v)_i^{n+1} - (\rho v)_i^n = 0 , \quad \Delta\alpha_{gi} = \alpha_{gi}^{n+1} - \alpha_{gi}^n = 0 ,$$

where  $\rho$  is the mixture density and  $\alpha_g$  is the void fraction of the gas phase. The procedure used to compute the coefficients for the Euler equations is described in appendix D, where also their final expression is given. In the same appendix the expression of  $\beta^1$ ,  $\beta^2$  and  $\beta^3$  for the Two-Phase Flow model is given, while for their computation the reader can refer to [5].

## Remarks

1. Note that the boundary conditions treatment described applies indifferently to steady computations and to space-time computations as well. In particular, in the space-time case, the unit nodal normal to the space-time boundary given by the past plane is always given by  $\vec{n}_i = (0, 0, 1)$ , while all the eigenvalues reduce to  $\lambda_k^i = 1 > 0$ , hence, consistently with the  $\mathcal{LPS}$  condition derived in the previous chapter, the past plane is a supersonic inlet-like boundary for which no residual must be computed. On the other hand, for the future plane one has  $\lambda_k^i = -1 < 0$  for all the eigenvalues, hence no boundary conditions must be imposed on the future plane that is a supersonic outlet-like boundary. As a consequence, there is no difference in the boundary treatment of steady and space-time computations.
2. The boundary conditions used in this project can be easily applied also if an implicit time-stepping procedure is used. In particular, the jacobian of the algebraic system  $\mathbf{J}_{ij} = \partial \mathbf{R}_i / \partial U_j$  will be modified with the following entry:

$$\mathbf{J}_{ij} += \sum_{\lambda_k^i > 0} \left( \frac{\partial \beta^k}{\partial U_j} \mathbf{r}^k + \beta^k \frac{\partial \mathbf{r}^k}{\partial U_j} \delta_{ij} \right) .$$

Since the  $\beta^k$  coefficient can be expressed as (see appendix D)

$$\beta^k = \mathbf{D}^k(U_i) \cdot \mathbf{R}_i + c^k(U_i) ,$$

where the vector  $\mathbf{D}^k$  and the scalar  $c^k$  depend only on  $U_i$ , one ends with

$$\mathbf{J}_{ij} += \sum_{\lambda_k^i > 0} \left( \frac{\partial \mathbf{D}_i^k}{\partial U_j} \cdot \mathbf{R}_i \delta_{ij} \mathbf{r}^k + \mathbf{D}_i^k \cdot \frac{\partial \mathbf{R}_i}{\partial U_j} \mathbf{r}^k + \frac{\partial c_i^k}{\partial U_j} \delta_{ij} \mathbf{r}^k + \beta^k \frac{\partial \mathbf{r}^k}{\partial U_j} \delta_{ij} \right) ,$$

where  $\partial \mathbf{R}_i / \partial U_j$  has been already computed to assemble the jacobian entry related to the inner residual. Thus, the jacobian entries related to the boundary conditions can be written as a linear combination of the entries related to the inner discretization, which are already known at this stage of the computation, plus informations related only to the actual value of the variables in node  $i$ , still allowing a nodal treatment of the boundary conditions. Note that  $\mathbf{D}_i^k = \mathbf{D}^k(U_i)$  and  $c_i^k = c^k(U_i)$  are known analytically, hence no numerical differentiation is necessary.

## 4.2 Local Time-Stepping Technique

The time<sup>1</sup> integration technique used for the computations is based on the very simple forward Euler formulas already given (equation (2.15)). In particular, since is only for steady solutions that we are seeking for<sup>2</sup>, a local nodal time-step is used to have a faster convergence, namely

$$U_i^{n+1} = U_i^n - \frac{\Delta t}{S_i} \mathbf{R}_i .$$

Since for the positivity of the N scheme one has to impose

$$\Delta t_i < \frac{S_i}{\sum_{T \in \Delta_i} \max_{k=1, \dots, N_{equations}} (\lambda_k^+)_T} ,$$

the time-stepping formula actually coded is

$$U_i^{n+1} = U_i^n - \frac{\nu}{\sum_{T \in \Delta_i} \max_{k=1, \dots, N_{equations}} (\lambda_k^+)_T} \mathbf{R}_i ,$$

with  $\nu < 1$ .

---

<sup>1</sup>Pseudo-time in the case of space-time computations

<sup>2</sup>Be it in time or in pseudo-time

# Chapter 5

## Results

In this chapter the results obtained on a series of well known steady and unsteady test-cases are reported and commented. Note that, since different systems of equations have been considered, it seemed more convenient not to write one chapter devoted to the presentation of the equations, but to describe briefly the basic equations in this chapter. To avoid confusion, most of the informations regarding the characteristics analysis of the models and their eigenstructure are given in appendix E. The outline of the chapter is the following: The first section contains the results obtained on the Euler equations. Solutions of unsteady and steady problems are discussed and compared, when possible, to analytical or reference solutions. In the second section the Two-Fluid Model is briefly presented and the solutions of some classic Two-Phase unsteady problems is shown.

### 5.1 Euler Equations

The system of the 2D Euler equations describes the motion of an inviscid non conductive material. They can be written in conservative form and in a cartesian frame of reference as

$$\frac{\partial}{\partial t} \begin{bmatrix} \rho \\ \rho u \\ \rho v \\ \rho E \end{bmatrix} + \frac{\partial}{\partial x} \begin{bmatrix} \rho u \\ \rho u^2 + p \\ \rho uv \\ \rho uH \end{bmatrix} + \frac{\partial}{\partial y} \begin{bmatrix} \rho v \\ \rho uv \\ \rho v^2 + p \\ \rho vH \end{bmatrix} = 0, \quad (5.1)$$

where  $\rho$  is the fluid density,  $p$  its pressure,  $\vec{u} = (u, v)$  its velocity,  $E$  and  $H$  the total energy and enthalpy. The system is closed by the state equation

$$p = (\gamma - 1)\rho \left( E - \frac{u^2 + v^2}{2} \right)$$

and by the definition of total enthalpy

$$H = E + \frac{p}{\rho}.$$

Introducing the vector of primitive variables  $P = [\rho \ u \ v \ p]^t$ , the system can be rewritten in the quasi-linear form

$$\frac{\partial P}{\partial t} + \mathbf{A}_P \frac{\partial P}{\partial x} + \mathbf{B}_P \frac{\partial P}{\partial y} = 0,$$

with  $\mathbf{A}_P$  and  $\mathbf{B}_P$  given by

$$\mathbf{A}_P = \begin{bmatrix} u & \rho & 0 & 0 \\ 0 & u & 0 & 1/\rho \\ 0 & 0 & u & 0 \\ 0 & \rho a^2 & 0 & u \end{bmatrix}, \quad \mathbf{B}_P = \begin{bmatrix} v & 0 & \rho & 0 \\ 0 & v & 0 & 0 \\ 0 & 0 & v & 1/\rho \\ 0 & 0 & \rho a^2 & v \end{bmatrix},$$

where  $a = \sqrt{\gamma p/\rho}$  is the local speed of sound. Since the system is hyperbolic, the matrix  $C = \mathbf{A}_P n_x + \mathbf{B}_P n_y$  is diagonalizable with a complete set of real eigenvalues and linearly independent eigenvectors and its eigenstructure is given in appendix E. Although different forms of system (5.1) with additional source terms have been considered, the flux vectors and the jacobian matrices of the system used to compute the upwind matrices (2.12) are always the ones just presented. In the paragraph relative to each test-case these different forms of the equations will be given, showing their relation with (5.1).

### 5.1.1 Unsteady Computations

#### A Mach 3 Wind Tunnel with a Forward Facing Step

This is a very famous test-case proposed by Colella and Woodward in [29]. It consists of a supersonic flow entering a channel that contains a forward facing step. The initial solution consists of a uniform Mach 3 flow. At the very beginning, a shock develops in front of the step and detaches from it growing and then reflecting on the upper and lower walls of the channel. The test was performed solving the space-time formulation of system (5.1) with the non-linear blended scheme. What usually causes some difficulties in the solution of this problem is the upper corner of the step which is a geometrical singularity. In [29] this problem is solved with a very particular treatment of the unknowns stored in the computational cells close to the singular point. Here no modifications of the scheme have been introduced to handle the singularity.

The effect of the presence of the singular point can be two-fold. Roe-type schemes usually show an unphysical expansion shock in correspondence of corner. The reason of this can be qualitatively understood considering the following analysis:

A 1D Roe-type scheme can be written in finite volume formulation as

$$U_i^{n+1} = U_i^n - \frac{\Delta t}{\Delta x} (H_{i+1/2} - H_{i-1/2}),$$

where the numerical flux function  $H_{i+1/2}$  is defined by

$$H_{i+1/2} = \frac{F_i + F_{i+1}}{2} - \frac{1}{2} R |\Lambda| L (U_{i+1} - U_i), \quad (5.2)$$

where  $F$  is the vector of the conservative fluxes,  $R$  and  $L$  are the matrices of the right and left eigenvectors of its jacobian and  $|\Lambda|$  is the diagonal matrix of the absolute values of the eigenvalues of the jacobian. In 1D  $\Lambda$  is given by

$$|\Lambda| = \begin{bmatrix} |u| & 0 & 0 \\ 0 & |u - a| & 0 \\ 0 & 0 & |u + a| \end{bmatrix}.$$

At the transonic point the eigenvalue  $|u - a|$  is zero, hence no numerical dissipation is added from the scheme along the corresponding characteristic field. In some configurations this causes the preservation of discontinuous data and hence the appearance of what is usually called a transonic expansion shock. An example of such a phenomenon is given on the left of figure 5.1, where the solution of this problem obtained in [7] using standard  $\mathcal{RD}$  schemes with the consistent mass matrix is reported at time  $t = 0.5$ . The discontinuity at the corner is clearly visible. On the right of the same picture, the solution obtained here on the same mesh used in [7] at the same physical time is shown. As it can be seen from the picture, apart from being globally more diffusive, the solution obtained with the space time schemes does not contain any transonic shock. The reason of this can be understood considering the space-time version of the 1D Roe scheme presented above. In (5.2) the vector of the conservative fluxes would be substituted by the vector of the space-time fluxes whose jacobian matrix will have eigenvalues given by

$$\Lambda^{s-t} = \begin{bmatrix} un_x + n_t & 0 & 0 \\ 0 & un_x + n_t - a|n_x| & 0 \\ 0 & 0 & un_x + n_t + a|n_x| \end{bmatrix},$$

from which is clear that at the transonic point the scheme still provides some numerical dissipation associated to  $|(un_x + n_t - a|n_x|)^{\text{transonic}}| = |n_t|$ . This extra diffusion is enough to dissipate the expansion shock.

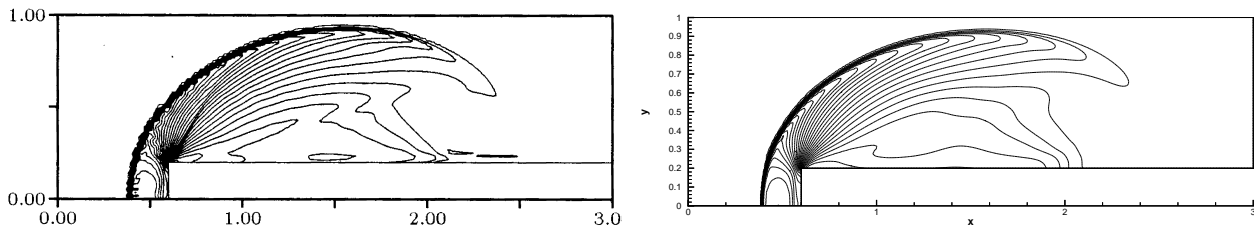


Figure 5.1: Expansion at the Singular Point,  $t = 0.5$ . Left: Solution From [7], Right: Solution Obtained with the Space-Time Approach

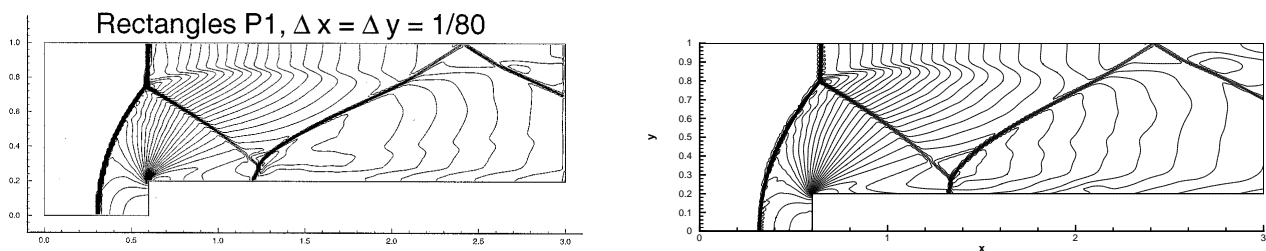


Figure 5.2: Unphysical Mach Stem on the Lower Wall,  $t = 4.0$ . Left: Solution from [30], Right: Solution Obtained with the Space-Time Approach

Very often, the presence of the corner causes a completely different behavior of the solution. On the left of figure 5.2 is reported the solution of this problem obtained in [30] with a Discontinuous Galerkin Method at time  $t = 4.0$ . On the right in the same figure the result obtained here on the grid used in [7] is shown. A Mach stem on the lower wall is clearly visible in both results. The presence of the Mach reflection can be explained with the a great amount of spurious numerical dissipation that causes the appearance of an unphysical entropy layer. The entropy production at the corner is clearly visible in figure 5.3 where the entropy contours of the solutions obtained here at times  $t = 0.5$  and  $t = 1.5$  are reported.

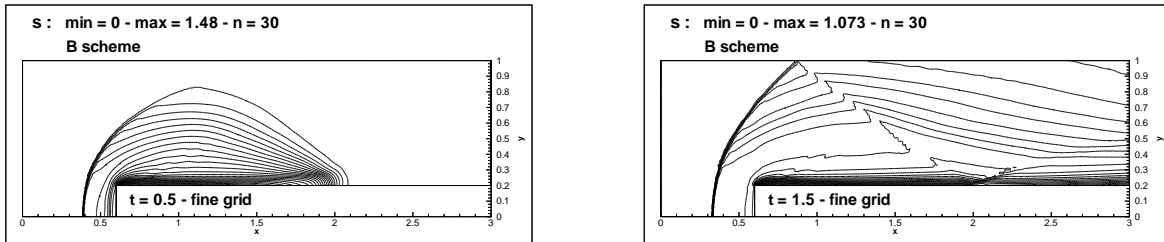


Figure 5.3: Entropy Production at the Corner

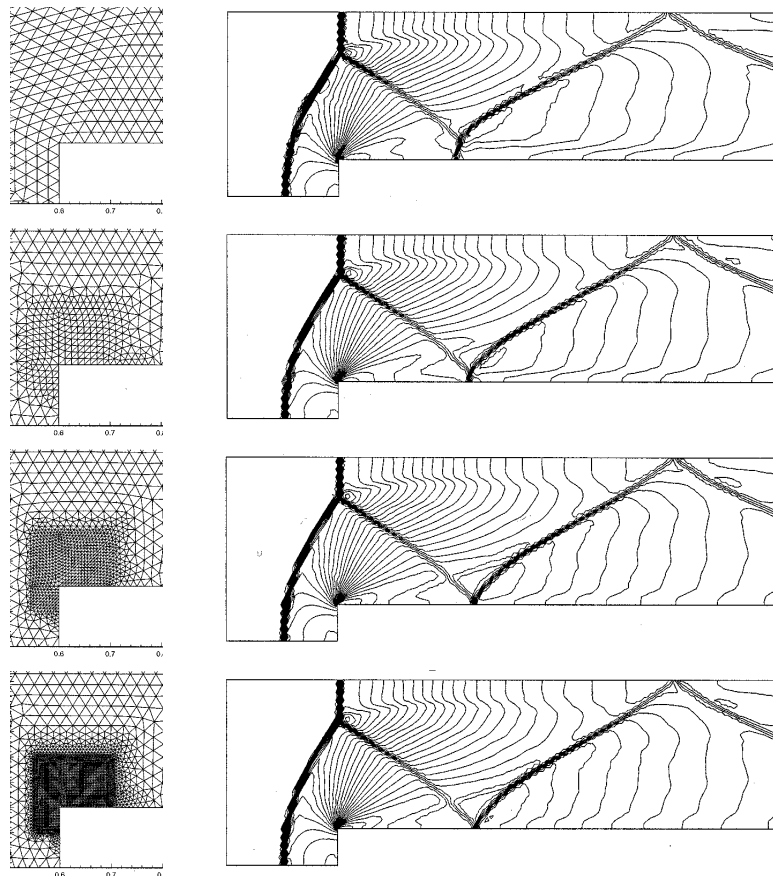


Figure 5.4: Effect of the Progressive Grid Refinement Around the Corner (from [30])

An effective way to cure this problem is suggested in [30]: refine the grid locally around the singular point so that the false entropy layer is contained within a few cells and does not pollute the solution downstream. The effect of the progressive refinement of the mesh as reported in [30] is shown in figure 5.4. Here a similar technique was used. The top of figure 5.5 shows a close-up view of the grid around the singular point with and without refinement and below the improvement obtained in the solution at  $t = 4.0$ . Although a small Mach reflection is still visible, due to the very localized refinement of the grid<sup>1</sup>, the improvement in non-negligible.

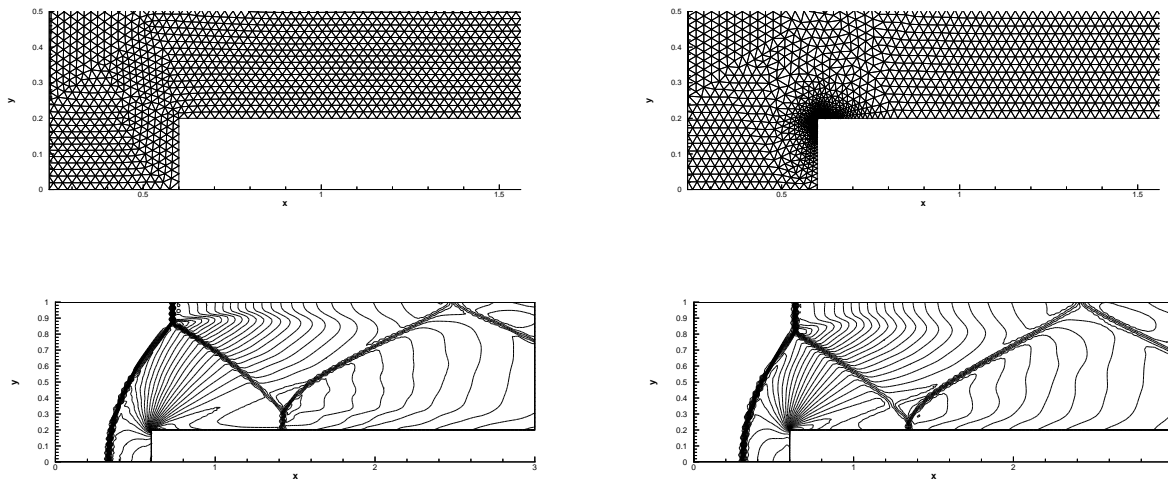


Figure 5.5: Grid Refinement Around the Corner and Improvement of the Solution

Once the problem with the corner has been solved, a fine version of the refined mesh of figure 5.5 has been used to compare with reference [29]. In particular, the reference solutions reported in [29] have been obtained with a third order PPM scheme on a uniform cartesian grid with  $\Delta x = \Delta y = 1/80$ . The mesh used here contains 38740 triangles and 19715 nodes, with a characteristic mesh-size  $h = 1/80$  and a refined mesh-size around the corner  $h_c = 1/1000$ . The computation is made with the second order non-linear blended scheme. Taking advantage of the double-layer space-time approach the physical  $CFL$  number was fixed as  $CFL = h_c/h$  in order to have an effective  $CFL_e \approx 1$  in the uniform grid-size region. In figures 5.6 and 5.7 a few snap-shots of the time evolution of the density computed here are reported together with the reference solution. Note that the agreement is very good, also considering that the method used in the reference is third order accurate while the space-time computations cannot be more than second order accurate in space. A main difference can be found in the resolution of the contact discontinuity coming from the triple point which appears very much smeared in the present solution. On the other hand, the space-time computations show a very clean and monotone capturing of the discontinuities.

---

<sup>1</sup>The typical size of the elements of the grid is  $h = 1/40$ , while very close to the corner it goes down to  $h_c = 10^{-3}$ . Despite of the small mesh-size around the corner, an entropy layer still develops due to the small region of refinement

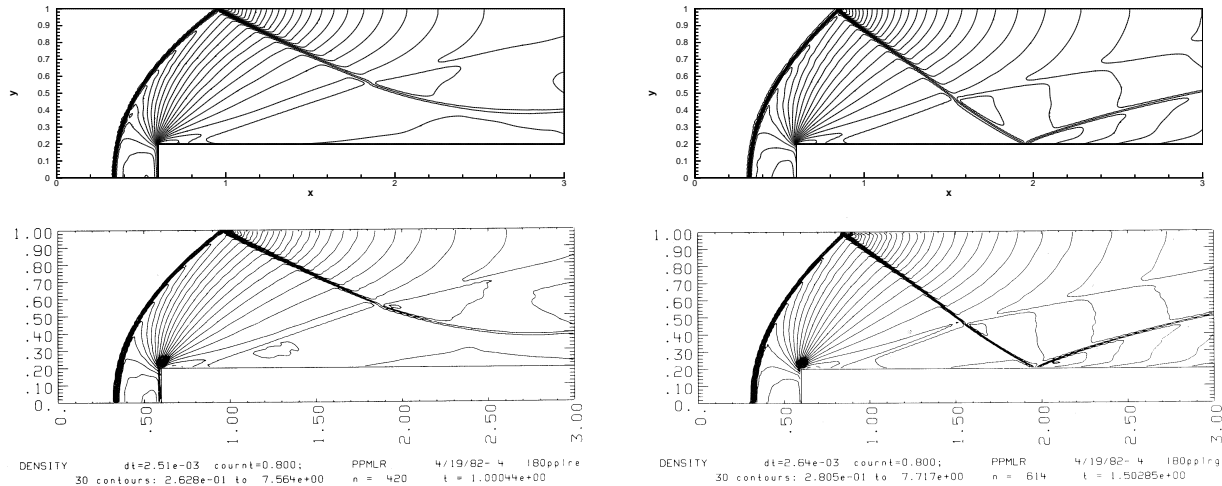


Figure 5.6: Mach 3 Wind Tunnel with a Step, Solutions at  $t = 1.0$  and  $t = 1.5$ . Top: Present, Bottom: Reference Solution [29]

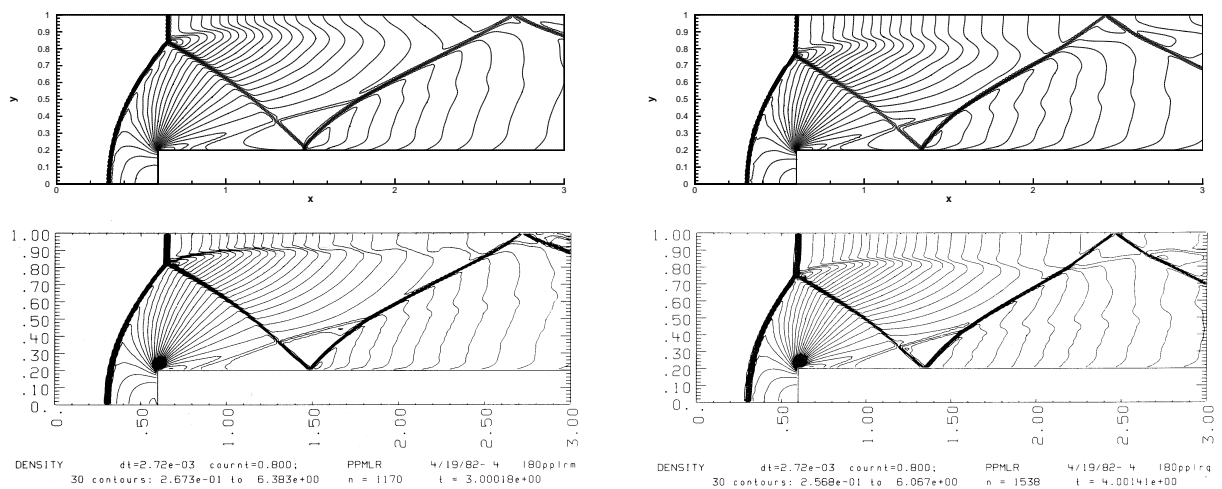


Figure 5.7: Mach 3 Wind Tunnel with a Step, Solutions at  $t = 3.0$  and  $t = 4.0$ . Top: Present, Bottom: Reference Solution [29]

This problem has been used as a test for the new treatment of conservation described in chapter 3. The space-time blended scheme fully based on a flux computation done through contour integration of the vector of the fluxes has been tested. Figure 5.8 shows the solution obtained with the new approach at  $t = 4.0$  on the intermediate refined grid of figure 5.5 and on the fine grid. Comparing the plots of figure 5.8 with the ones in figures 5.5 and 5.7 no visible difference in the solutions can be seen. The solution is still very clean and completely monotone, which shows the robustness of the approach. Furthermore, all the shocks are in the correct position, indicating that the scheme is still fully conservative. This very promising result will be confirmed by the more severe tests presented in the following sections.

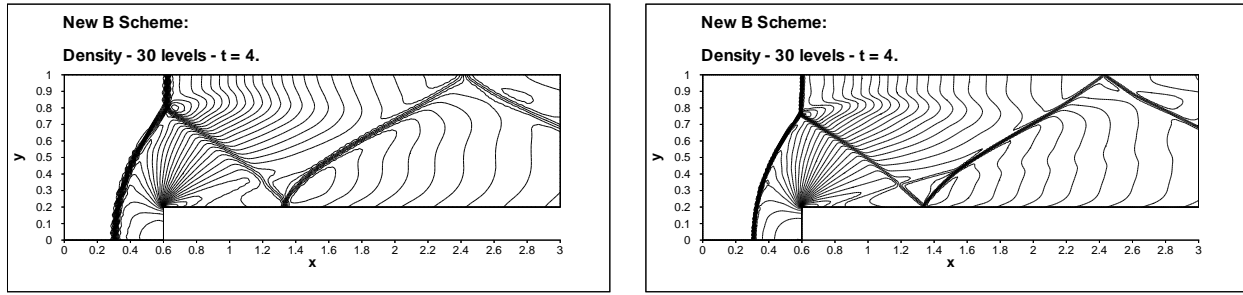


Figure 5.8: Mach 3 Wind Tunnel with a Step: Solution at  $t = 4.0$  Obtained with the B Scheme Based on the New Treatment of Conservation

### Transonic Flow in a Channel with a Bump with Oscillating Back-Pressure

This problem was proposed for the first time by Bölcs and co-workers in [31] and later on re-computed by Hwang and Liu in [32] and by Rogiest in [33]. It consists of a channel whose length is equal to 2 and whose height is equal to 1 with a sinusoidal bump on the upper wall. The initial solution is a Mach 0.675 flow with a transonic shock on the bump. Starting from this solution a sinusoidal outlet pressure is imposed. In particular, according to [33], the following law for the outlet pressure is fixed:

$$p_{\text{out}} = \frac{1}{\gamma M_{\infty}^2} \left[ 1 + 0.12 \left( 1 + \frac{\gamma - 1}{2} M_{\infty}^2 \right)^{\frac{\gamma}{\gamma - 1}} \sin(\omega t) \right], \quad (5.3)$$

with  $M_{\infty} = 0.675$  and  $\omega = 0.792$ . The problem was solved here using the space-time formulation of system (5.1) and the subsonic inlet and outlet boundary conditions of chapter 4. The grid and the initial steady solution computed with the space-time blended scheme are reported in figure 5.9. Starting from the solution of figure 5.9 the unsteady outlet pressure (5.3) was imposed. Taking advantage of the two-layers approach, the  $\Delta t$  was fixed such that one period of outlet pressure oscillation corresponded to 200 physical time-steps. The unsteady evolution of the Mach number is shown in figures from 5.10 to 5.17, compared with the results of [33].

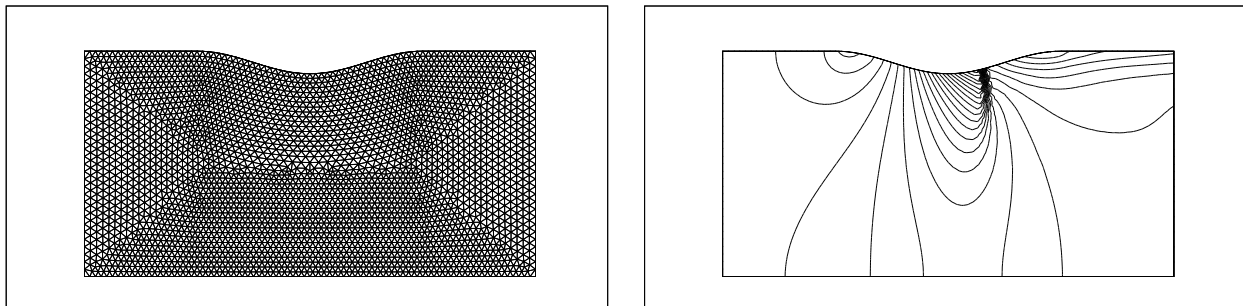


Figure 5.9: Transonic Channel: Grid (left) and Mach Contours of the Initial Solution (right)

Figure 5.10 shows the solutions after the first cycle, when the value of the outlet pressure is equal to the stationary one and is increasing. The shock, which already exists on the upper wall, is moving toward the exit of the channel and it starts to reach the lower wall. In the solution of figure 5.11 the shock has reached the lower wall and it starts to react to the increasing outlet pressure raise. The delay between the instant in which the pressure starts to increase and the one in which the shock feel the pressure increase is due to the finite speed of propagation of sound. Some time after (figures 5.12 and 5.13), although the pressure is decreasing, the shock is moving upstream and deforming. Again the finite speed of sound is responsible for this time lag. At times  $t = 24\pi/8\omega$  and  $t = 26\pi/8\omega$  the flow is subsonic throughout the channel, as it can be seen in figures 5.14 and 5.15. The pressure minimum is reached at  $t = 28\pi/8\omega$  when a weak shock is already present on the upper wall (figure 5.16). The end of the second cycle is shown in figure 5.17, where the flow pattern of figure 5.10 is restored.

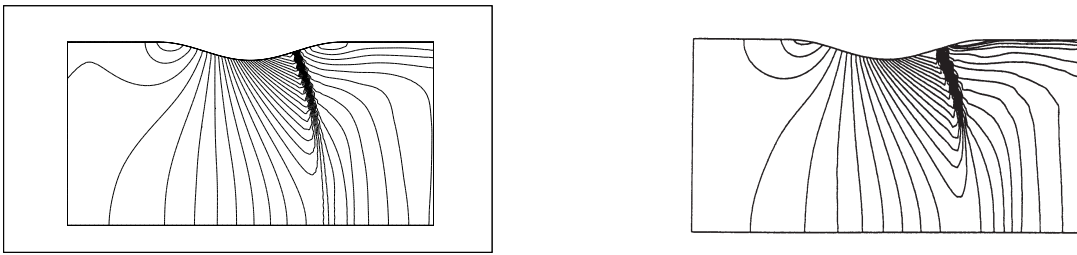


Figure 5.10: Transonic Channel: Unsteady Solution,  $\omega t = 2\pi$ . Left: Present, Right: [33]

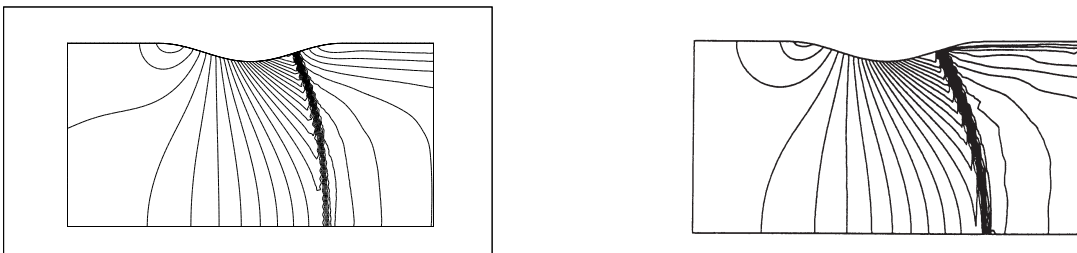


Figure 5.11: Transonic Channel: Unsteady Solution,  $\omega t = 18\pi/8$ . Left: Present, Right: [33]

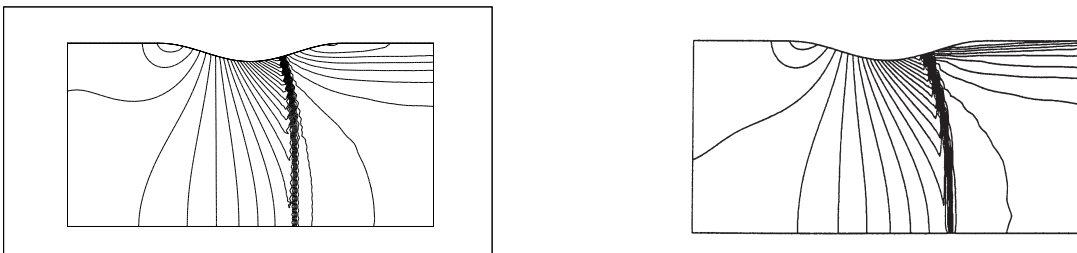


Figure 5.12: Transonic Channel: Unsteady Solution,  $\omega t = 20\pi/8$ . Left: Present, Right: [33]

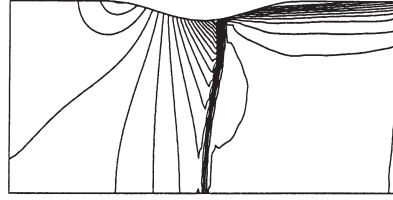
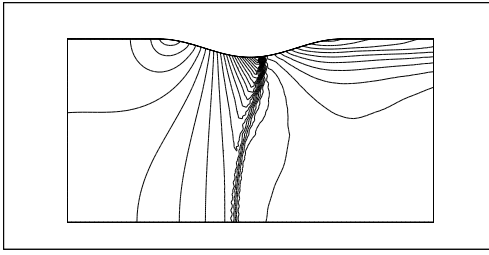


Figure 5.13: Transonic Channel: Unsteady Solution,  $\omega t = 22\pi/8$ . Left: Present, Right: [33]

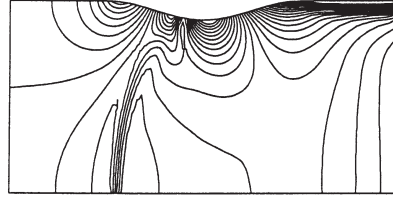
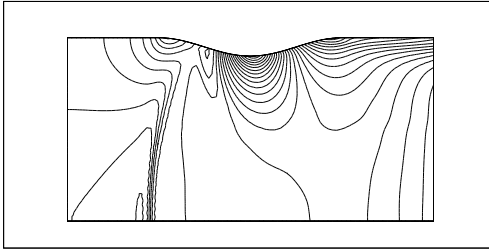


Figure 5.14: Transonic Channel: Unsteady Solution,  $\omega t = 24\pi/8$ . Left: Present, Right: [33]

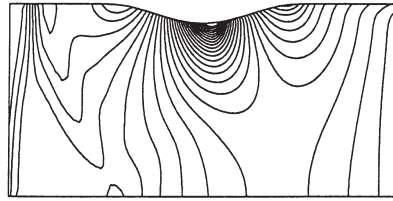
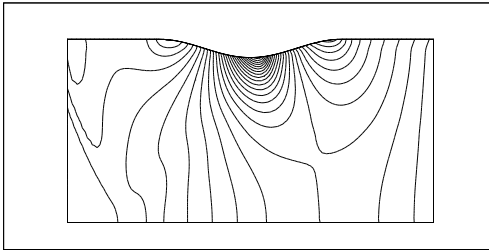


Figure 5.15: Transonic Channel: Unsteady Solution,  $\omega t = 26\pi/8$ . Left: Present, Right: [33]

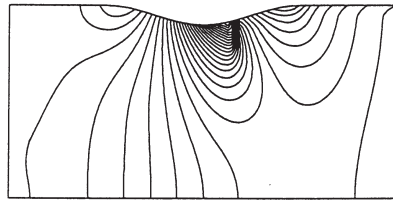
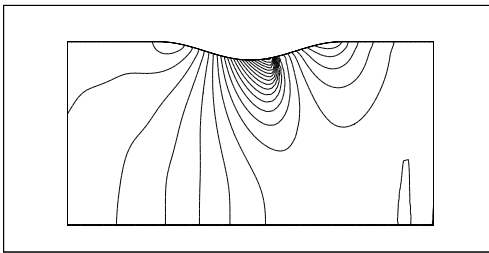


Figure 5.16: Transonic Channel: Unsteady Solution,  $\omega t = 28\pi/8$ . Left: Present, Right: [33]

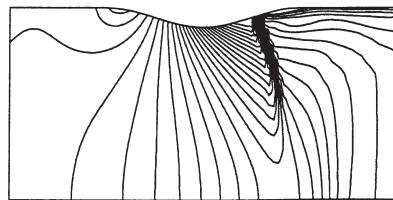
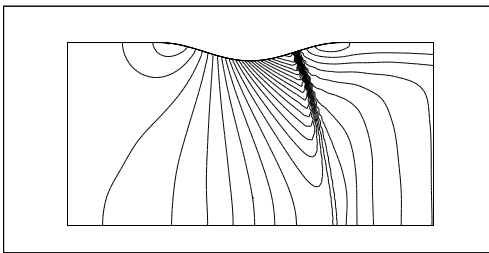


Figure 5.17: Transonic Channel: Unsteady Solution,  $\omega t = 4\pi$ . Left: Present, Right: [33]

The comparison between the solution obtained here and the reference one shows a good agreement, considering that both are obtained numerically. What is interesting to note is that the space-time schemes seem to have a small advancing phase shift with respect to the finite volume method used in the reference. Figures 5.11, 5.12 and 5.13 clearly show that the shock, especially on the lower wall, is situated more upstream in the space-time solution than in the finite volume one, as if one was looking at a later time solution. Same thing for the smooth flow patterns of figures 5.14 and 5.15, which seem identical in the result obtained here and in the reference one, apart from a consistent space, and hence time, shift. One element to take into account could be the grid used in the computations, but in [33] a structured  $79 \times 30$  grid was used, while the mesh of figure 5.9 contains 3162 nodes which is a bit more than the number of cells used in the reference, although reasonably close to it. A different explanation could be that the space-time approach itself might introduce a phase error when applied to non-linear periodic problems. Other tests reported in this chapter will show the same type of advancing phase error, which deserves further investigation. As far as the present test-case is concerned, a computation on a finer grid could be performed to verify if the apparent advancing phase error is still present.

### A Cylindrical 1D Riemann Problem with a Source Term

To test the accuracy of the new source terms discretization, a cylindrical 1D Riemann problem similar to the one proposed in [34] has been solved. Consider the physical state described in figure 5.18: an initial circular discontinuity in pressure and density located in the center of the physical domain on top of a static background<sup>2</sup>.

The idea is to use the 1D radial version of the axisymmetric Euler equations to simulate the time evolution of such a system.

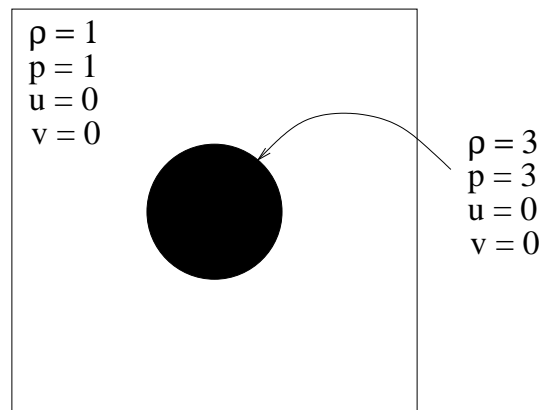


Figure 5.18: Initial Physical State for the Cylindrical Riemann Problem

---

<sup>2</sup>Zero velocity everywhere

The 2D axisymmetric Euler equations can be written as

$$\frac{\partial}{\partial t} \begin{bmatrix} \rho \\ \rho u_x \\ \rho u_r \\ \rho E \end{bmatrix} + \frac{\partial}{\partial x} \begin{bmatrix} \rho u \\ \rho u_x^2 + p \\ \rho u_x u_r \\ \rho u_x H \end{bmatrix} + \frac{\partial}{\partial r} \begin{bmatrix} \rho u_r \\ \rho u_x u_r \\ \rho u_r^2 + p \\ \rho u_r H \end{bmatrix} = S, \quad S = -\frac{1}{r} \begin{bmatrix} \rho u_r \\ \rho u_x u_r \\ \rho u_r^2 \\ \rho u_r H \end{bmatrix}, \quad (5.4)$$

being  $x$  the axis of symmetry,  $u_x$  the component of the velocity parallel to the axis and  $u_r$  the radial component of the velocity. Considering again figure 5.18, the  $x$  axis would be the one perpendicular to the page and the radial would be the one starting from the center of the circular discontinuity and going toward the external region of the domain. Note that system (5.4) can be seen as system (5.1) with the addition of the source term  $S$  which accounts for the effects of the axisymmetry. In particular, assuming  $u_x = 0$  and  $\partial/\partial x = 0$  everywhere, one ends with

$$\frac{\partial}{\partial t} \begin{bmatrix} \rho \\ \rho u_r \\ \rho E \end{bmatrix} + \frac{\partial}{\partial r} \begin{bmatrix} \rho u_r \\ \rho u_r^2 + p \\ \rho u_r H \end{bmatrix} = S, \quad S = -\frac{1}{r} \begin{bmatrix} \rho u_r \\ \rho u_r^2 \\ \rho u_r H \end{bmatrix}, \quad (5.5)$$

which is nothing else than the system of the 1D Euler equation, with the source term  $S$ . Finally the definition of the Riemann problem is: solve system (5.5) with the initial state

$$\begin{cases} [\rho \ u_r \ p] = [3 \ 0 \ 3] & \text{if } r < r_0 \\ [\rho \ u_r \ p] = [1 \ 0 \ 1] & \text{if } r > r_0 \end{cases}.$$

The problem is that, since no analytical solution is available for such a test-case, one needs to build a reference solution. The approach used here is the following: Solve the real 2D Riemann problem described in figure 5.18 on a fine isotropic mesh with the 2<sup>nd</sup> order blended scheme and at the same time solve the 1D Riemann problem with the source term on a very fine 1D mesh using the blended scheme and the new source term treatment. Note that one could simply use the 1D second order solution on the fine mesh as a reference, but the comparison with the 2D solution will further verify the reliability of the 1D result. For symmetry reasons, the 2D computation was run only on one quarter of the physical domain using an isotropic Delaunay mesh with 20000 triangles and 10201 nodes. A close-up view of the mesh is given in figure 5.19.

Note that a 2D Riemann problem has been already proposed as a test-case in [14], but in that case the initial discontinuity was taken to be square-shaped, so that on the symmetry lines<sup>3</sup> a pure 1D Riemann problem was recovered. In this case one would expect, given the symmetry of the problem and the isotropic mesh, to have the same distribution of the variables along any ray going through the origin of the domain. The 2D solution at  $t = 0.4$  is shown in figure 5.20 in terms of density and pressure contours. It can be noted that the solution presents a reasonable cylindrical symmetry, considering that in the mesh no preferential orientation of the edges of the triangles do exist.

---

<sup>3</sup>Parallel to the edges of the initial discontinuity

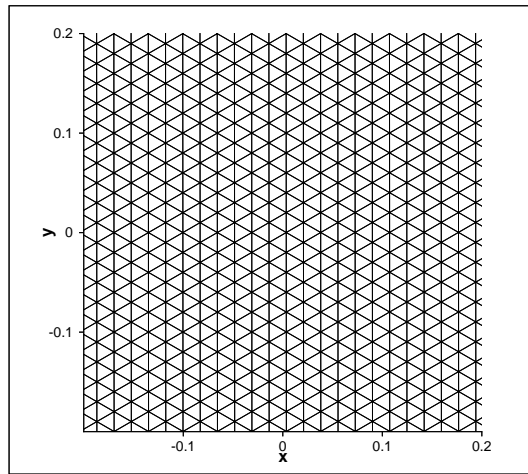


Figure 5.19: Close-up View of the Isotropic Mesh used for the Cylindrical Riemann Problem

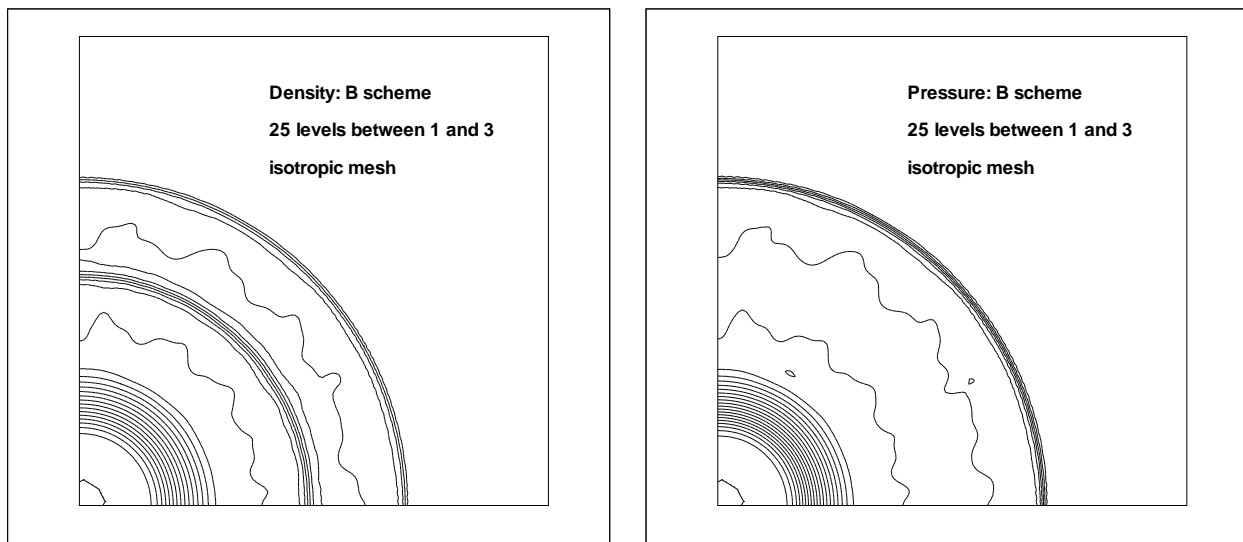


Figure 5.20: Cylindrical Riemann Problem:  $t = 0.4$ , B scheme. Left: density, Right: pressure

The 1D solution was computed using 4001 nodes and then compared with cuts of the 2D solution along rays going through the origin of the circular discontinuity, at different angles. The comparison is shown in figure 5.21, where the 1D solution is the solid line and the 2D results are plotted with symbols. Several conclusions can be drawn from the comparison. The agreement between 1D and 2D results indicates that the 1D model is correct and the 1D solution can be indeed considered as a reference given the agreement with the multidimensional one. Furthermore, comparing the plots at different angles one realizes that a very small deviation from cylindrical symmetry is present in the 2D solution.

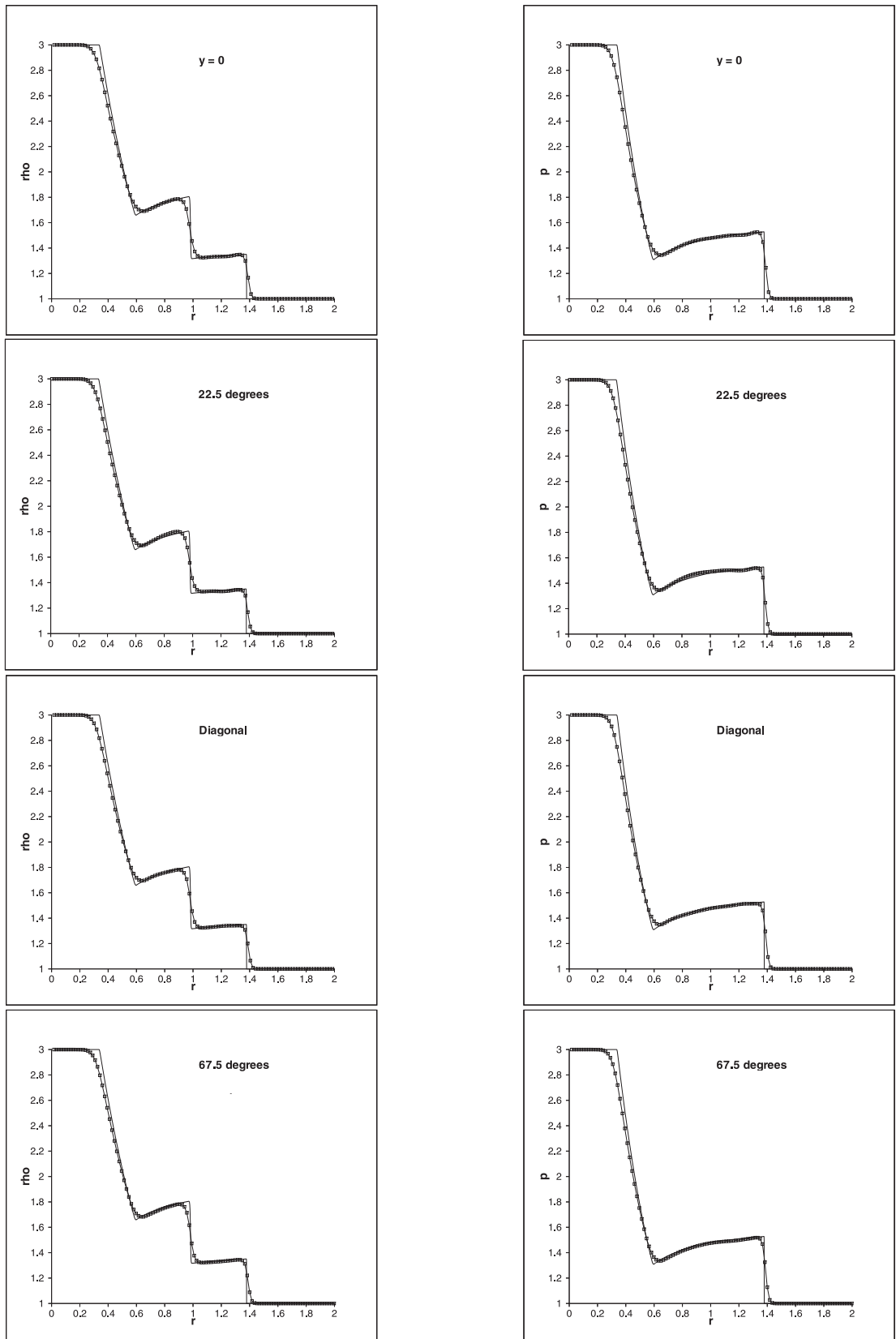


Figure 5.21: Cylindrical Riemann Problem: Comparison of the 1D Solution (solid line) with cuts of the 2D Solution Along Rays at Different Angles (symbols)

Once a reference solution has been obtained, the new source term discretization has been tested on this new 1D Riemann problem. In particular, the N scheme and the blended scheme with the consistent treatment of the source term have been used to solve the problem on different meshes and the results have been compared to the reference solution. The results are summarized in figures from 5.22 to 5.24.

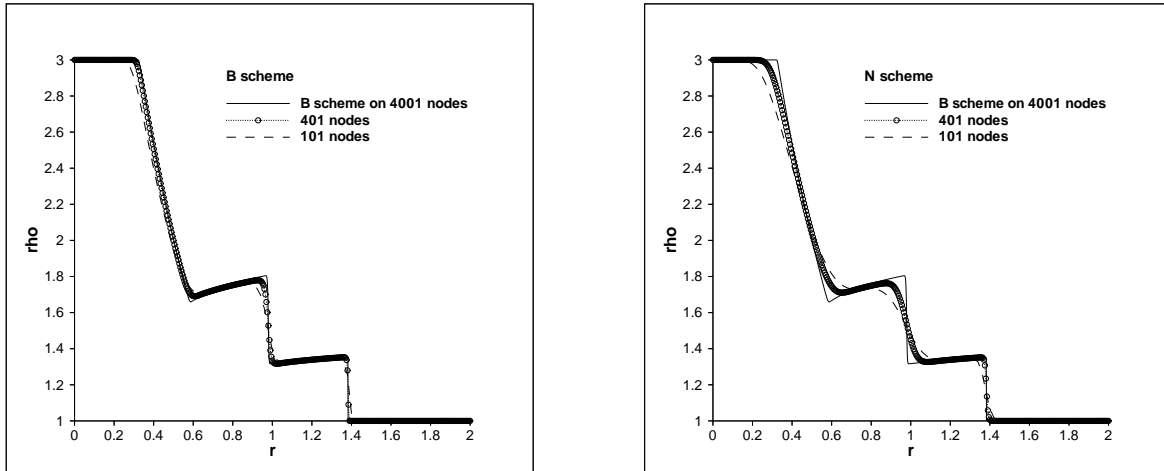


Figure 5.22: 1D Cylindrical Riemann Problem:  $t = 0.4$ , density. Left: B scheme, Right: N scheme

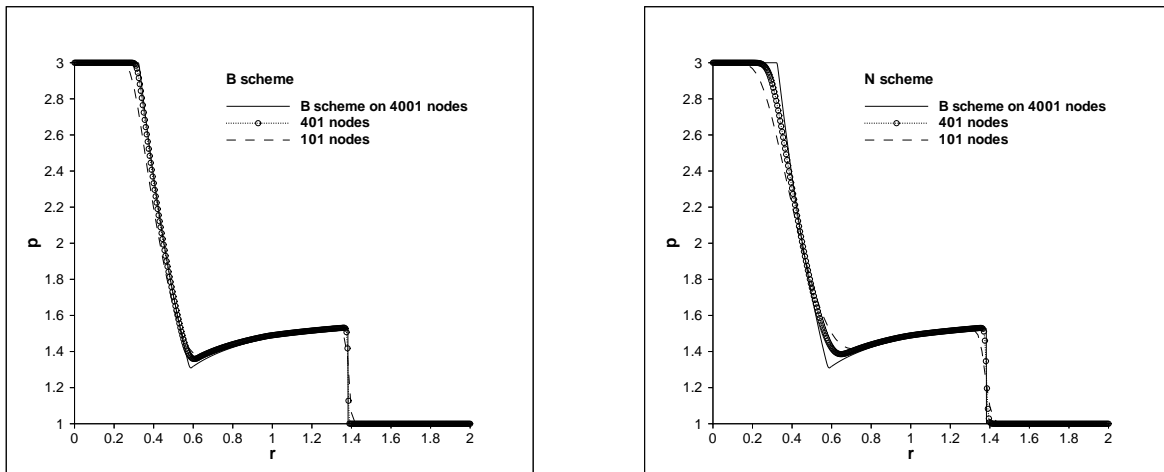


Figure 5.23: 1D Cylindrical Riemann Problem:  $t = 0.4$ , pressure. Left: B scheme, Right: N scheme

From the pictures is clear that the B scheme behaves as a typical 2<sup>nd</sup> order scheme while the N scheme is indeed only first order. This difference is confirmed by the direct comparison of the two schemes given in figure 5.25. The conclusion one draws from this test is that indeed the new source term treatment works and it is robust enough to handle discontinuous solutions. In addition, the blending of the  $\mathcal{LP}$  LDA scheme with the N scheme with the inclusion in both of the consistent discretization of the source terms gives a blended scheme which is indeed monotone and gives a sharper resolution of the discontinuities, typical of a second order scheme.

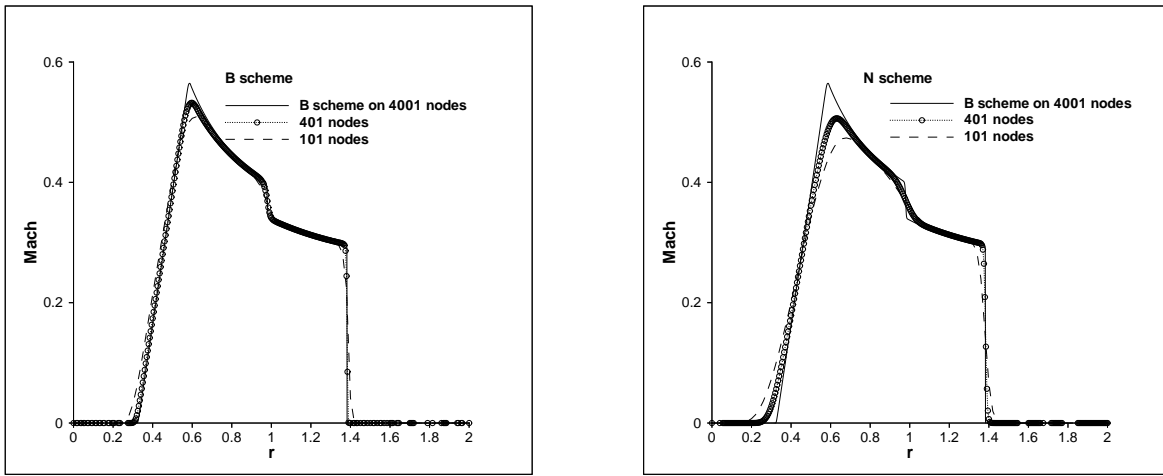


Figure 5.24: 1D Cylindrical Riemann Problem:  $t = 0.4$ , Mach. Left: B scheme, Right: N scheme

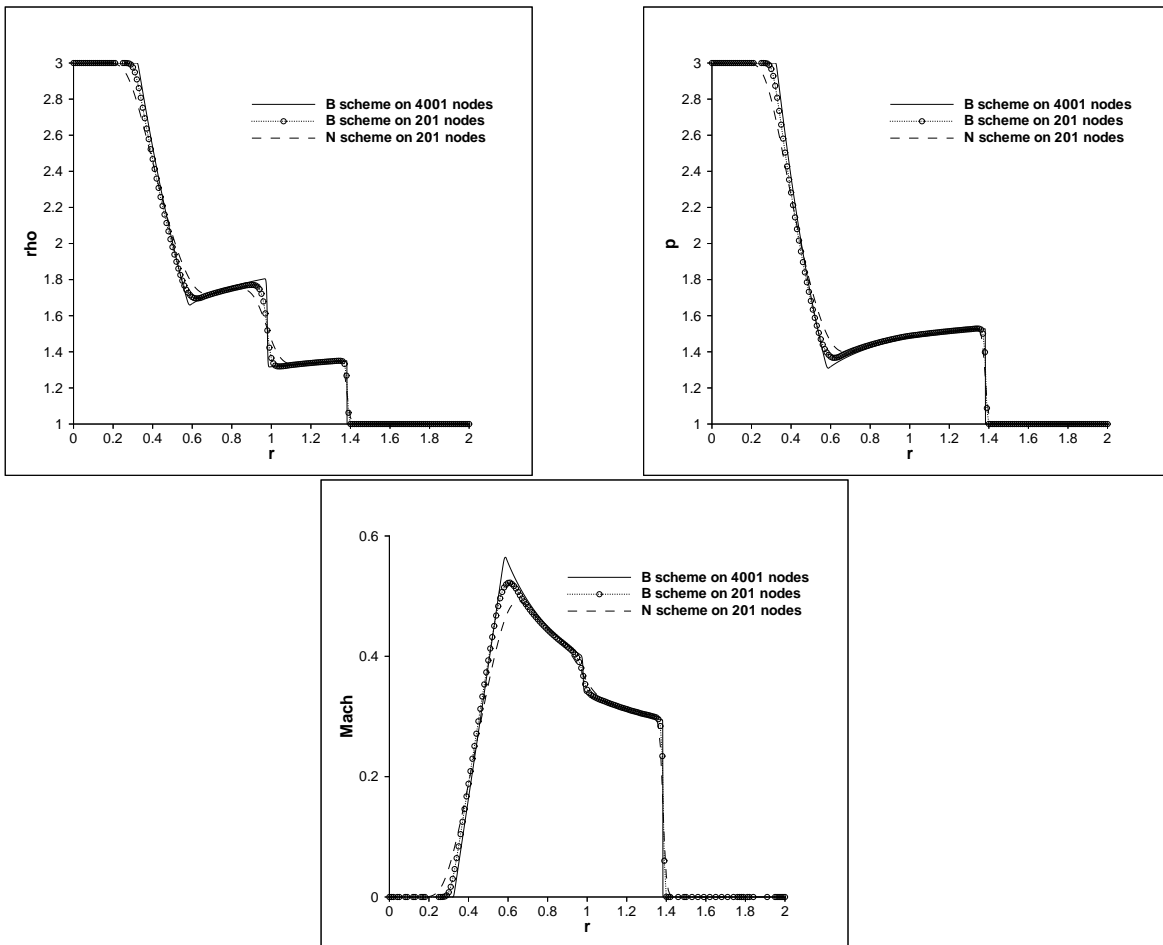


Figure 5.25: 1D Cylindrical Riemann Problem: comparison between N and B schemes both with the new consistent treatment of the source term

## 5.1.2 Steady Computations

### Steady Quasi-1D Nozzle Flows

A typical 1D test-case with a source term is obtained considering the so-called quasi-1D Euler equations, that is, the 1D Euler equations in which one takes into account the variation with the  $x$  coordinate of the area crossed by the fluid. Indicating with  $A = A(x)$  the variation of the cross-sectional area, the system of equation reads

$$\frac{\partial}{\partial t} \begin{bmatrix} \rho A \\ \rho u A \\ \rho E A \end{bmatrix} + \frac{\partial}{\partial x} \begin{bmatrix} \rho u A \\ (\rho u^2 + p) A \\ \rho u H A \end{bmatrix} = S, \quad S = \begin{bmatrix} 0 \\ p \frac{\partial A}{\partial x} \\ 0 \end{bmatrix}.$$

Defining the modified density  $\rho' = \rho A$  and modified pressure  $p' = pA$  the equations can be rewritten as

$$\frac{\partial}{\partial t} \begin{bmatrix} \rho' \\ \rho' u \\ \rho' E \end{bmatrix} + \frac{\partial}{\partial x} \begin{bmatrix} \rho' u \\ \rho' u^2 + p' \\ \rho' u H \end{bmatrix} = S', \quad S' = \begin{bmatrix} 0 \\ \frac{p'}{A} \frac{\partial A}{\partial x} \\ 0 \end{bmatrix},$$

while the equation of state becomes

$$p' = (\gamma - 1)\rho' \left( E - \frac{u^2}{2} \right).$$

It is clear that if the modified density and pressure are used as primitive variables, the quasi-1D Euler equations can be considered as the 1D Euler equations with the addition of a source term which accounts for the variation of the cross-sectional area. The advantage of this approach is that it allows to perform simulations of flows through 1D channels of arbitrary geometry, by simply adding to the equations a source term and by imposing the proper initial and boundary conditions. In particular, here the same 1D nozzle geometry used in [35] was used in the computations, for which the area variation, plotted in figure 5.26, can be analytically expressed as

$$A(x) = \begin{cases} 1 + \frac{3}{2} \left[ 1 - \frac{x+5}{5} \right]^2 & \text{if } -5 \leq x \leq 0 \\ 1 + \frac{1}{2} \left[ 1 - \frac{x+5}{5} \right]^2 & \text{if } 0 \leq x \leq 5 \end{cases}.$$

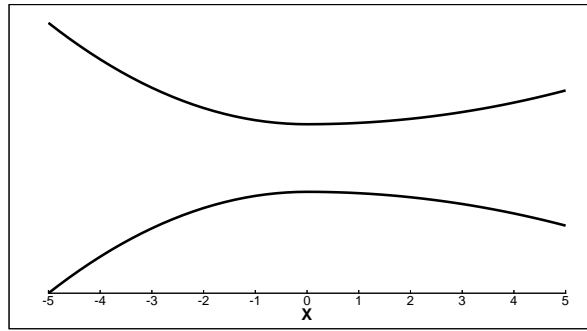
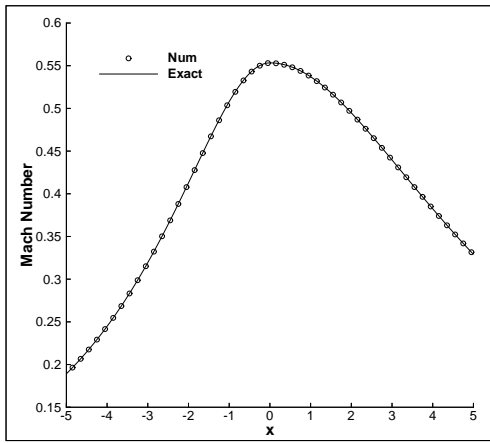
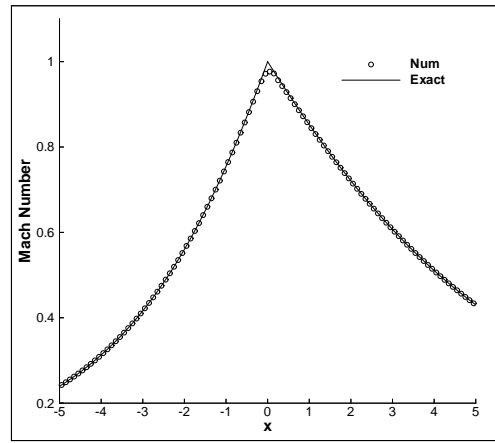


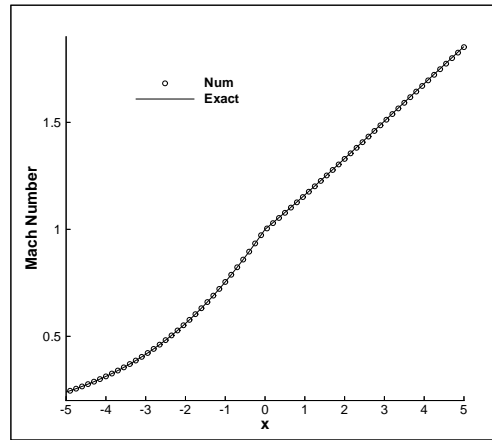
Figure 5.26: Cross-Sectional Area Variation for the Quasi-1D Nozzle Flow Simulations



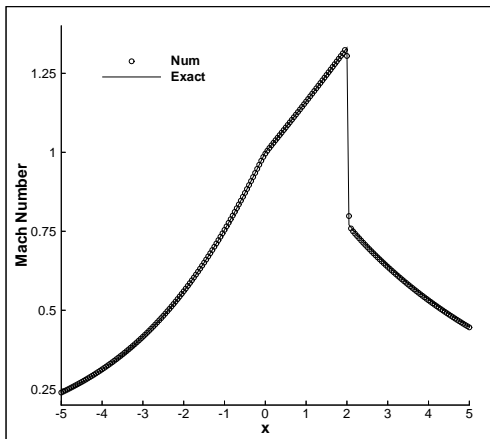
(a)



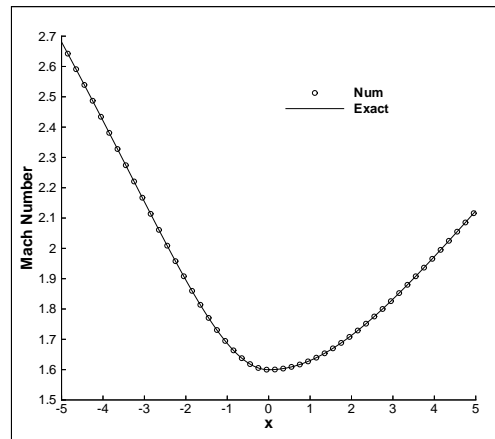
(b)



(c)



(d)



(e)

Figure 5.27: Steady Quasi-1D Euler: Mach Number distribution along the nozzle. (a) Fully Subsonic, (b) Choked Subsonic, (c) Adapted, (d) Transonic Shock, (e) Fully Supersonic

For steady quasi-1D flows, a simple procedure to compute the exact solution exists based on the isentropic flow relations and on the Rankine-Hugoniot shock conditions. This technique, extensively explained in [35], was used here to compute the exact solution for five different

cases: fully subsonic flow, choked subsonic flow, adapted flow, a flow with a transonic shock and a supersonic flow. Once the exact solution was known, the exact total temperature and pressure at the inlet have been used to impose the inlet boundary condition for the subsonic cases and the same has been done for the outlet pressure. Note that the boundary treatment is crucial especially for the subsonic outlet, since the shock position and the appearance of the choking condition are very sensitive to the variation of the outlet pressure. Since it is well known that a pure 1D upwind discretization with a consistent upwinding of the source term yields a second order solution (see references [23, 24, 25]), and in order to further test the new multidimensional upwind source term treatment, the computations were run with the space-time blended scheme, starting from a uniform flow, and marching in time until a steady state was reached in terms of the  $L_2$  norm of the density residual<sup>4</sup>. The final result of the computations on 201 points are presented in terms of Mach number distribution along the nozzle and are plotted in figure 5.27 together with the exact solution. The agreement is remarkable.

### Jets Interaction

This is the first of a series of steady tests performed to verify the robustness and the reliability of the new discretization techniques proposed in chapter 3. In particular, the new treatment of conservation has been compared on this problem to the traditional approach based on the Deconinck-Struijs-Roe linearization of the jacobians of the system. The steady matrix schemes described in section 2.1.2 have been used and Simpson's rule has been used for the contour integration. The test is taken from [1] and it consists of the interaction of two horizontal supersonic jets which are suddenly brought into contact. The upper stream is characterized by  $M_{up} = 4$ ,  $\rho_{up} = 0.5$  and  $p_{up} = 0.25$ , while for the lower stream one has:  $M_{low} = 2.4$ ,  $\rho_{low} = 1.0$  and  $p_{low} = 1.0$ . The domain is a  $1 \times 1$  square. The interaction of the two jets produces a shock wave in the low pressure jet and an expansion fan in the high pressure one. A contact discontinuity develops in the middle. The mesh used is a  $100 \times 100$  diamond grid. In figure 5.28 the description of the problem and a zoom of the mesh used in the computation are reported.

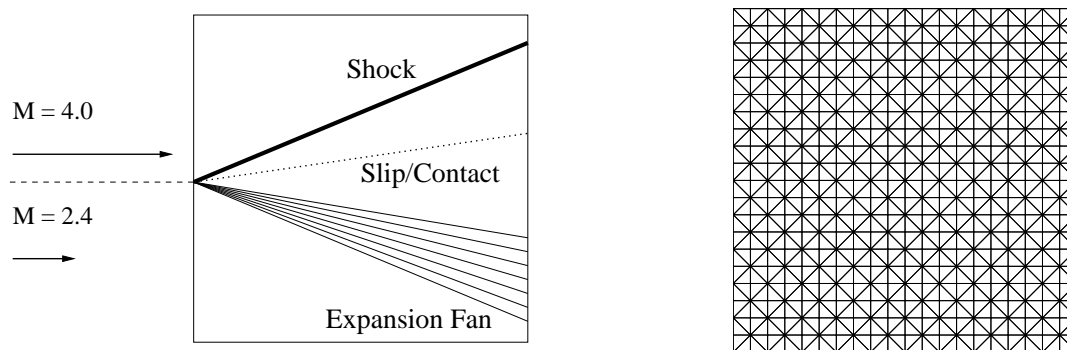


Figure 5.28: Jets Interaction Problem: Problem Description and Zoom of the grid

---

<sup>4</sup>Practically speaking, the computation was stopped when  $\frac{\sum_{i=1, \dots, \text{nodes}} (\rho_i^{n+1} - \rho_i^n)^2}{\text{nodes}}$  was smaller than a fixed threshold  $\epsilon \approx 10^{-7} \div 10^{-8}$ , where  $n$  indicates the physical time level

The results obtained with the schemes based on the new treatment of conservations are reported in figure 5.29 in terms of density contours. The correct reproduction of the physics can be seen from the picture. The outlet Mach number distribution is then compared in figure 5.30 with the one obtained on the same mesh and using the traditional formulation of the schemes based on the computation of the integral of the fluxes using the Roe averaged quasi-linear form of the equations.

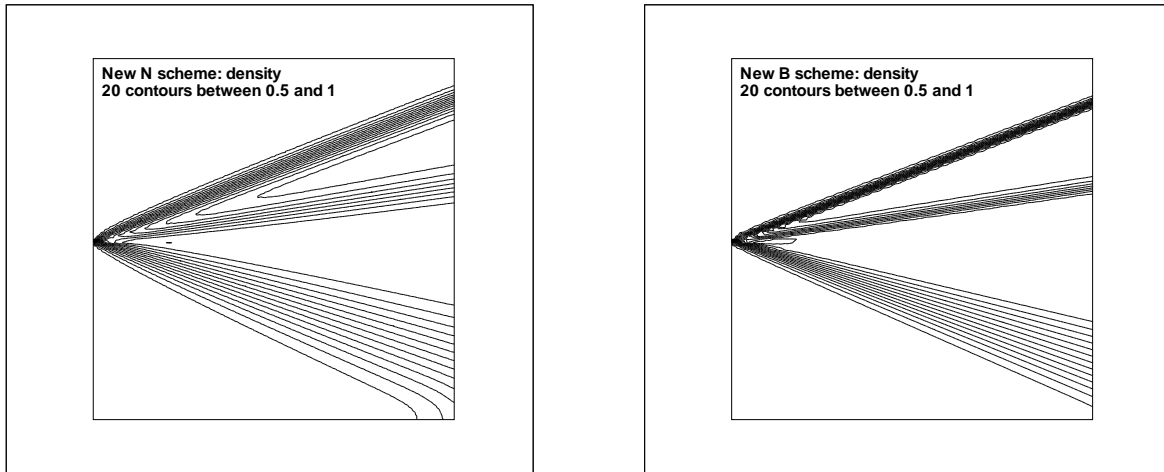


Figure 5.29: Jets Interaction Problem: Solution obtained with the new schemes. Left: N scheme, Right: B scheme

Both the new N scheme and B scheme have been tested and compared with their original version. First, from the density isolines, one can recognize the complete monotone behavior of the schemes based on the new treatment of conservation and the sharp resolution of the discontinuities obtained with the blended scheme which seems indeed second order. The comparison with the original schemes based on the Deconinck-Struijs-Roe averaging shows perfect agreement.

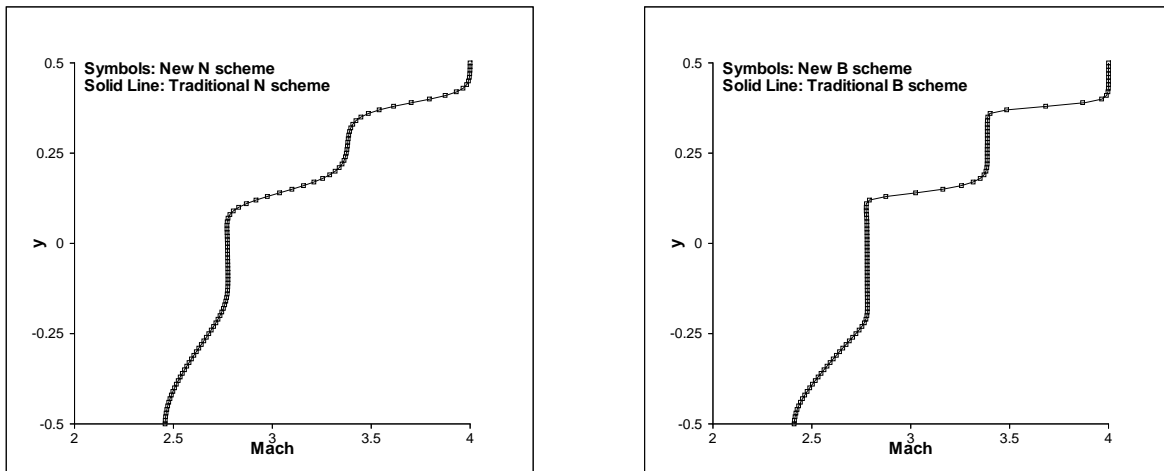


Figure 5.30: Jets Interaction Problem: Comparison with Roe Averaging, Outlet Mach Number. Left: N scheme, Right: B scheme

## Scramjet Inlet

This problem is also taken from [1] and consists of a supersonic inlet of a scramjet. The inlet Mach number is  $M_{in} = 3.6$ , the upper wall is a symmetry line and the outlet flow is still supersonic. The N and B schemes based on the new treatment of conservation were tested and compared with their analogous based on Roe averaging. Figure 5.31 shows a detail of the grid used for the computations containing 7056 nodes and 13383 triangles, while the Mach isolines of the solutions obtained with the new N and B schemes are given in figure 5.32.

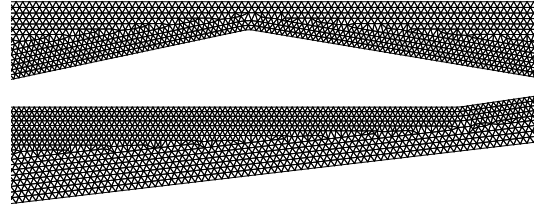


Figure 5.31: Scramjet Inlet. Particular of the Grid

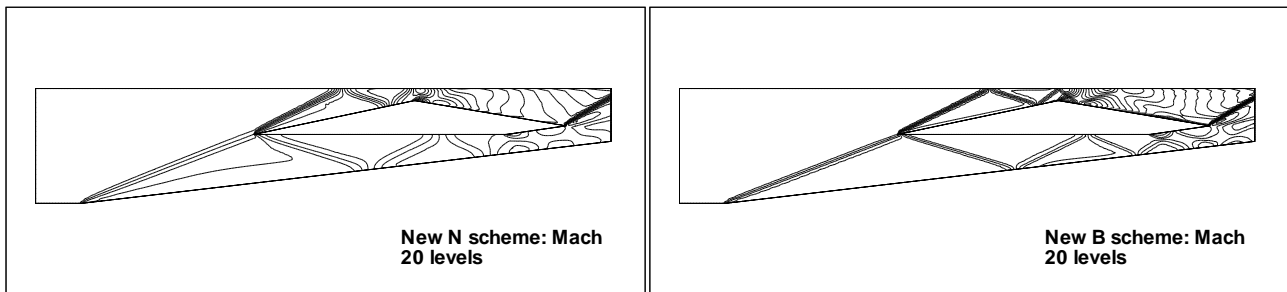


Figure 5.32: Scramjet Inlet: Mach Number Isolines. Left: new N Scheme, Right: new B Scheme

Both solutions show a good prediction of the compression of the flow through the series of shocks reflecting between the symmetry line and the wedge and the better resolution of the B scheme is clear. Moreover, the solutions are both monotone. The distribution of density pressure and Mach number along the symmetry line were compared with the ones computed with the classical N and B scheme based on the Deconinck-Struijs-Roe Linearization on the same grid. The comparison is shown in figures 5.33, 5.34 and 5.35. The agreement between the solutions obtained with the different approaches is almost perfect.

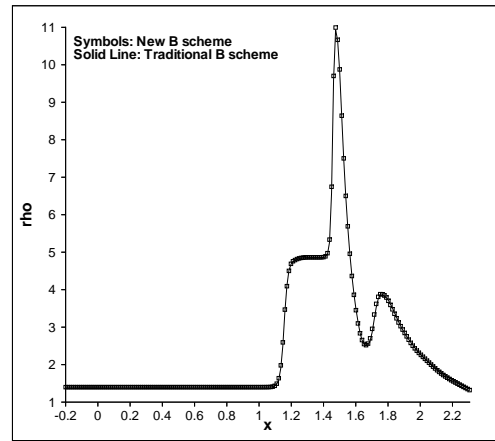
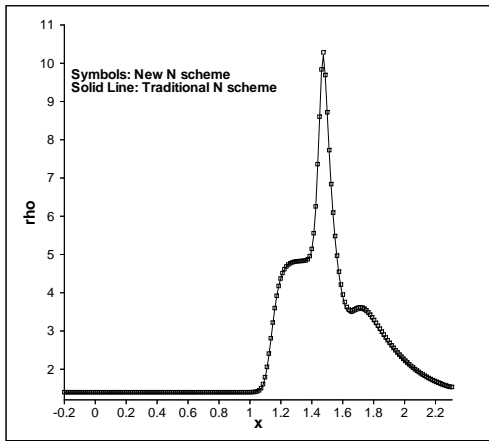


Figure 5.33: Scramjet Inlet: density along the symmetry line, comparison with Roe averaging. Left: N scheme, Right B scheme. Symbols: New Approach, Solid: Roe Average

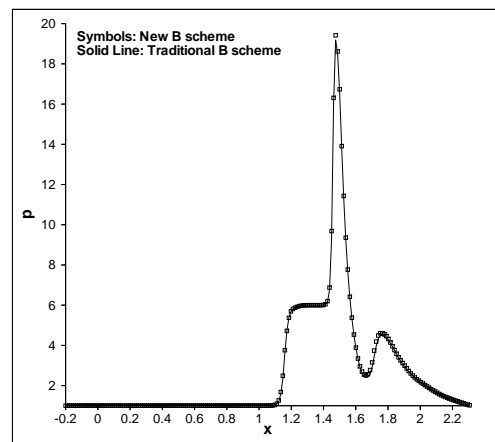
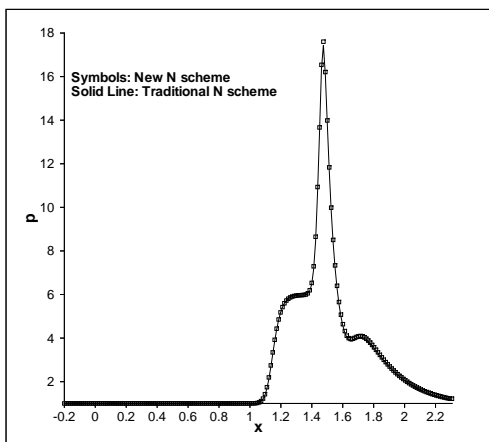


Figure 5.34: Scramjet Inlet: pressure along the symmetry line, comparison with Roe averaging. Left: N scheme, Right B scheme. Symbols: New Approach, Solid: Roe Average

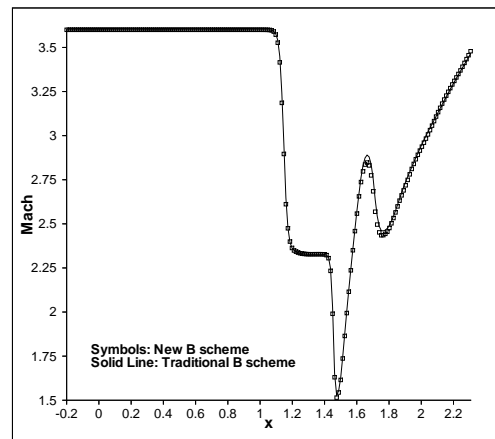
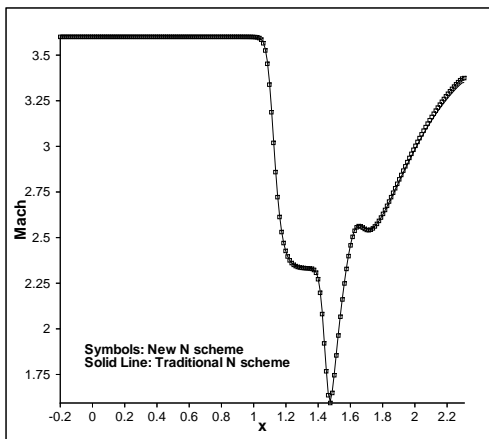


Figure 5.35: Scramjet Inlet: Mach number along the symmetry line, comparison with Roe averaging. Left: N scheme, Right B scheme. Symbols: New Approach, Solid: Roe Average

## Mach 10 Flow Around a Cylinder

In order to further test the robustness of the new N scheme based on the contour integration of the fluxes with Simpson's rule, a Mach 10 bow shock over a cylinder was computed. The grid used is a quite fine Delaunay mesh containing 12085 nodes and 23740 triangles. Given the symmetry of the problem, only the upper half of the flow was simulated. The solution obtained with the new approach is compared with the results obtained with the original N scheme in figure 5.36 in terms of Mach and pressure isolines. In particular, the two solutions are plotted one on top of the other with different colors.

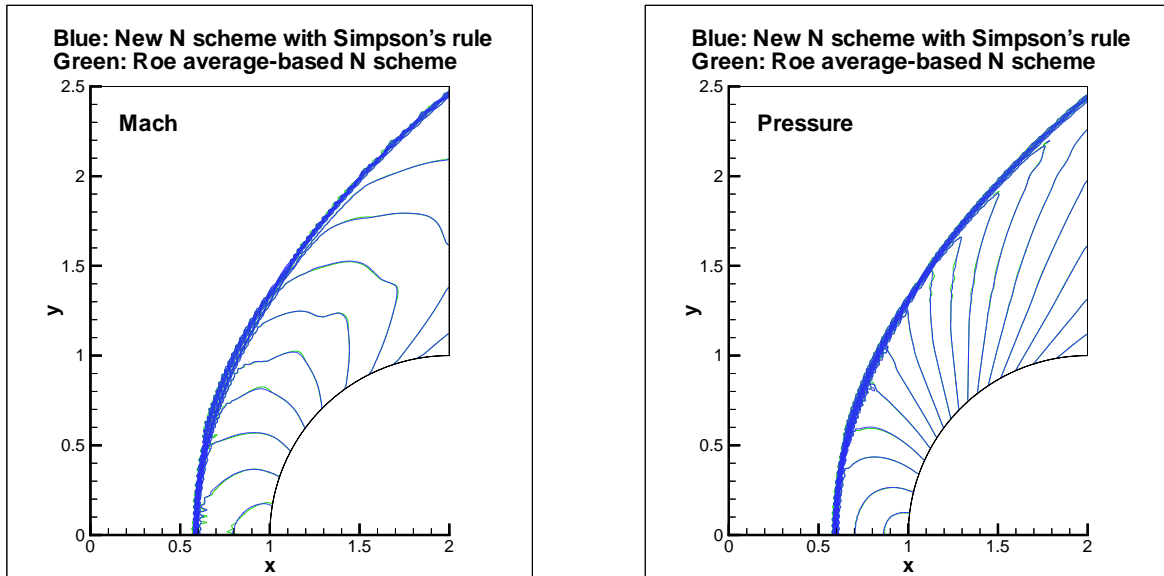


Figure 5.36: Mach 10 Flow Over a Cylinder: comparison with Roe averaging

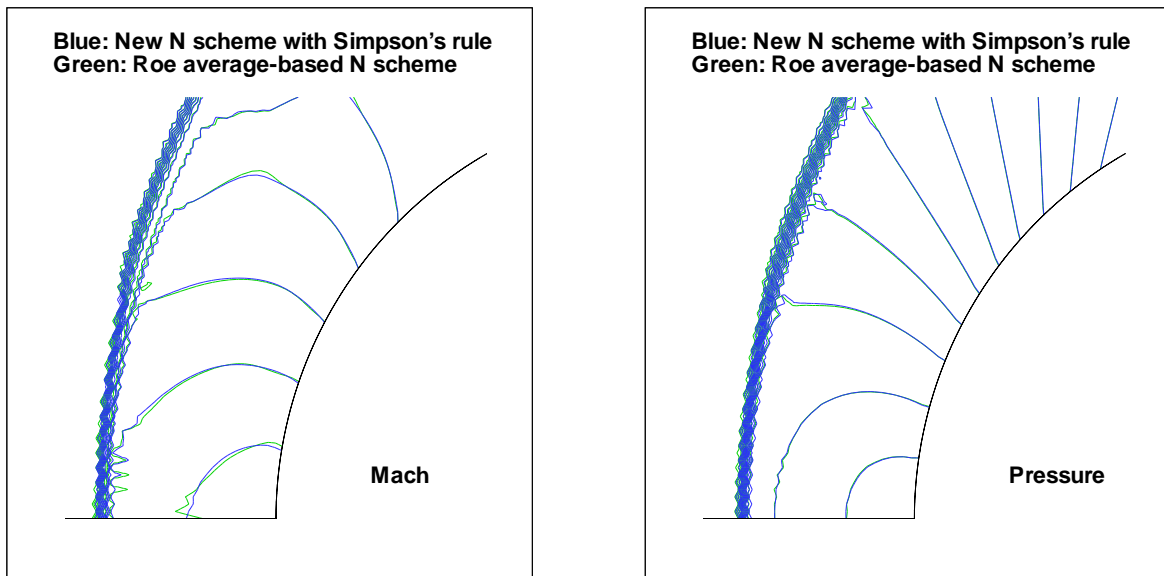


Figure 5.37: Mach 10 Flow Over a Cylinder: Stagnation point

A closer view of the stagnation point is also reported in figure 5.37. As it can be seen from the pictures, one can hardly distinguish the two solutions. The conclusion is that the N scheme based on the new treatment of conservation and contour integration with Simpson's rule is as much robust and reliable as the one based on Roe averaging is. This is confirmed by the comparison of pressure and Mach number distribution along the symmetry line shown in figure 5.38.

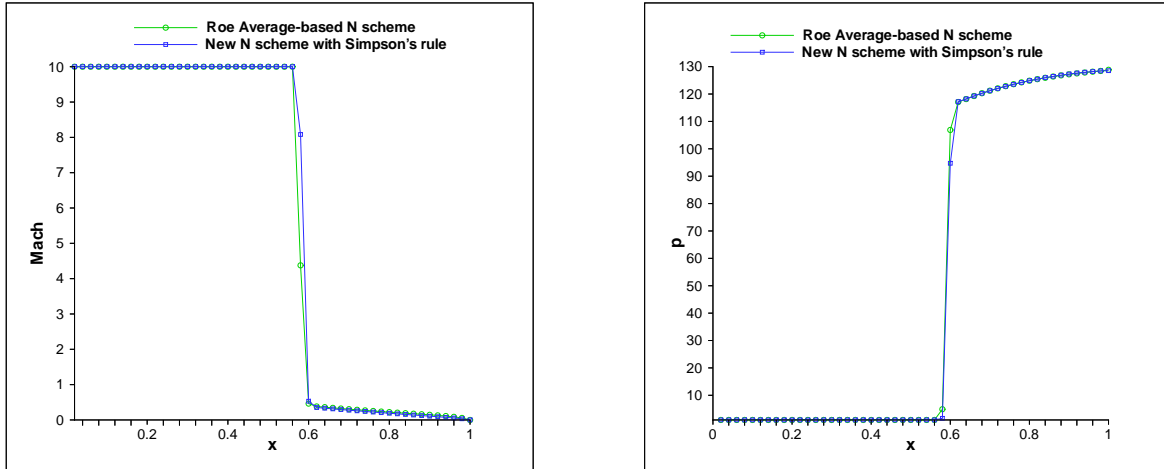


Figure 5.38: Mach 10 Flow Over a Cylinder: comparison with Roe averaging. Pressure and Mach distribution along the symmetry line

### Mach 4 Flow Around a Sphere

A bow shock computation was also used to test the robustness of the source term discretization. In particular, the steady matrix N scheme with the new consistent source term treatment of chapter 3 was used to solve equations (5.4) on the same 2D grid used for the test-case of the bow shock around a cylinder. This time the symmetry line has taken to be a line of axial symmetry so that a bow shock around a sphere could be simulated. The incoming flow Mach number was taken to be  $M_\infty = 4$ . A computation using a centered treatment of the axisymmetry source term was tried to compare with the new approach, but the central discretization turned out to be not stable enough to handle this problem. The result obtained with the new approach is shown in terms of Mach number and pressure isolines in figures 5.39 and 5.40.

The plots show a perfect and monotone shock capturing. What is very important to underline is that no special care has been taken in the low Mach region of the flow<sup>5</sup>, i.e. the basic matrix scheme has been applied to system (5.4) without any kind of preconditioning technique (see references [1, 2] for details). This adds value to the results shown here. The distribution of Mach number and pressure along the axis of symmetry is also reported (figure 5.41) to further prove the monotonicity of the solution.

<sup>5</sup>Which is also true for the Mach 10 flow around a cylinder test-case

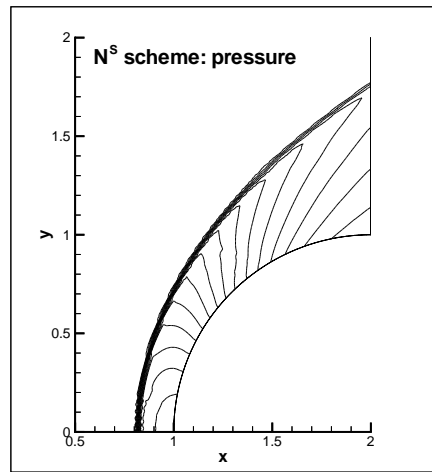
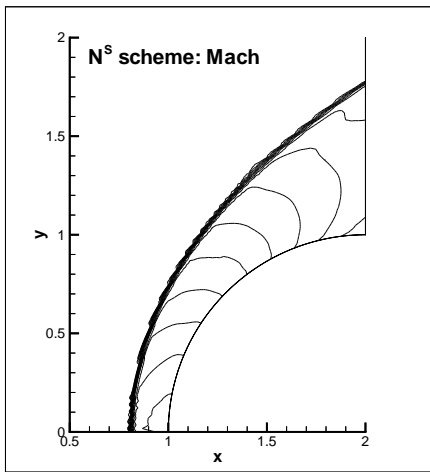


Figure 5.39: Mach 4 Flow Over a Sphere: Mach (left) and pressure (right) isolines

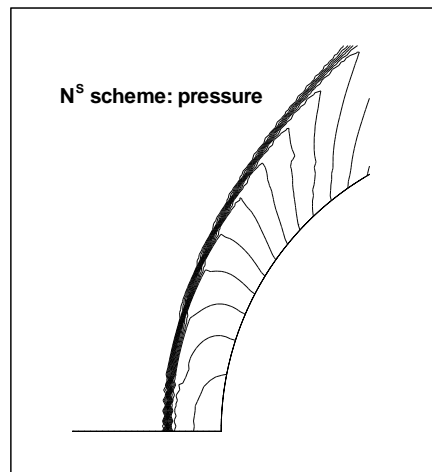
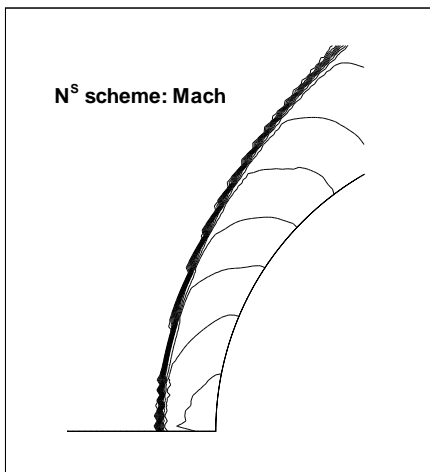


Figure 5.40: Mach 4 Flow Over a Sphere: Mach (left) and pressure (right) isolines at the Stagnation Point

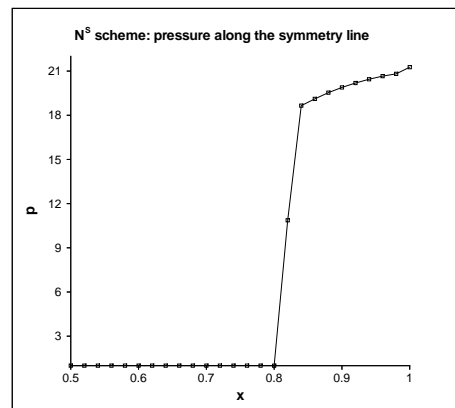
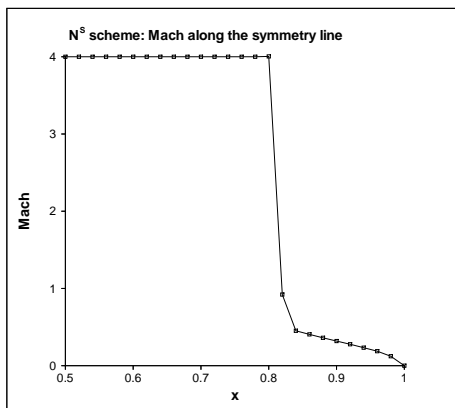


Figure 5.41: Mach 4 Flow Over a Sphere: Mach (left) and pressure (right) distribution along the axis of symmetry

## 5.2 Two-Fluid Mechanical Equilibrium Model

The two-phase flow model used in this project is probably the simplest model available in literature. It belongs to the class of models called Two-Fluid models and it can be obtained from the most general model under the assumptions of inviscid and isentropic flow of both phases and of a very strong mechanical coupling of the two fluids (see [5, 17, 18] for details). The two phases considered are a liquid phase and a gas phase chosen to be representative of water and air. As a consequence of the hypothesis of isentropic flow one does not need to solve the energy equations, while the strong mechanical coupling between the phases translates into the condition of equal velocities of the two phases [5]. The system of equations can be written in the following conservative form

$$\frac{\partial}{\partial t} \begin{bmatrix} \alpha_l \rho_l \\ \alpha_g \rho_g \\ \rho u \\ \rho v \end{bmatrix} + \frac{\partial}{\partial x} \begin{bmatrix} \alpha_l \rho_l u \\ \alpha_g \rho_g u \\ \rho u^2 + p \\ \rho uv \end{bmatrix} + \frac{\partial}{\partial y} \begin{bmatrix} \alpha_l \rho_l v \\ \alpha_g \rho_g v \\ \rho uv \\ \rho v^2 + p \end{bmatrix} = \begin{bmatrix} 0 \\ 0 \\ \rho (\vec{g})_x \\ \rho (\vec{g})_y \end{bmatrix},$$

where  $\alpha_l$  and  $\alpha_g$  are the liquid and gas void fractions,  $\rho_l$  and  $\rho_g$  are the liquid and gas densities,  $\vec{u} = (u \ v)$  is the velocity vector,  $\vec{g}$  is the gravity vector and  $\rho$  is the mixture density defined by

$$\rho = \alpha_l \rho_l + \alpha_g \rho_g .$$

The system is closed by the relation between the void fractions

$$\alpha_l + \alpha_g = 1$$

and by the state equations

$$\rho_l = \rho_{l0} + \frac{p - p_0}{a_l^2} \quad , \quad p = \Gamma_g \rho_g^{\gamma_g} .$$

In the last equation  $\rho_{l0}$  and  $p_0$  are reference density and pressure for the liquid phase,  $a_l$  is the speed of sound of the liquid phase, assumed to be constant and  $\gamma_g$  is the ratio of the specific heat coefficients of the gas phase. In all the computations the following values have been used for these quantities

$$\begin{aligned} \rho_{l0} &= 1000 \text{ kg/m}^3 \\ p_0 &= 10^5 \text{ Pa} \\ a_l &= 1000 \text{ m/s} \\ \gamma_g &= 1.4 \end{aligned} .$$

The value of the constant  $\Gamma_g$  in the gas state equation has been fixed to  $\Gamma_g = 10^5 \text{ Pa (m}^3/\text{kg)}^{\gamma_g}$ . Note that the equations of state used are consistent with the hypothesis of isentropic flow. Although the model is written in conservative form, no Roe-type linearization exists for it, hence this would be the typical case in which the new treatment of conservation should be applied. Unfortunately, because of the small amount of time left for this part of the project, only the non-conservative formulation used in [5] could be implemented. In particular, defining

the vector of primitive variables

$$P = \begin{bmatrix} p \\ u \\ v \\ \alpha_g \end{bmatrix},$$

the system can be rewritten in the quasi-linear form

$$\frac{\partial P}{\partial t} + \mathbf{A}_P \frac{\partial P}{\partial x} + \mathbf{B}_P \frac{\partial P}{\partial y} = S_P, \quad (5.6)$$

with  $\mathbf{A}_P$  and  $\mathbf{B}_P$  given by

$$\mathbf{A}_P = \begin{bmatrix} u & \rho a^2 & 0 & 0 \\ 1/\rho & u & 0 & 0 \\ 0 & 0 & u & 0 \\ 0 & \beta & 0 & u \end{bmatrix}, \quad \mathbf{B}_P = \begin{bmatrix} v & 0 & \rho a^2 & 0 \\ 0 & v & 0 & 0 \\ 1/\rho & 0 & v & 0 \\ 0 & 0 & \beta & v \end{bmatrix},$$

where  $a$  is a mixture speed of sound given by

$$a = a_0 \sqrt{\frac{\rho_l \rho_g}{\rho \rho_s}}$$

with

$$a_0 = \sqrt{\frac{\rho_s}{\frac{\alpha_g \rho_l}{a_g^2} + \frac{\alpha_l \rho_g}{a_l^2}}}, \quad \rho_s = \alpha_l \rho_g + \alpha_g \rho_l$$

being  $a_g = \sqrt{\gamma_g p / \rho_g}$  the speed of sound in the gas phase, while  $\beta$  is defined by

$$\beta = \frac{a_0^2 \alpha_l \alpha_g}{\rho_s} \left( \frac{\rho_g}{a_l^2} - \frac{\rho_l}{a_g^2} \right).$$

Since the system is hyperbolic, the matrix  $C = \mathbf{A}_P n_x + \mathbf{B}_P n_y$  is diagonalizable with a complete set of real eigenvalues and linearly independent eigenvectors. The eigenvalue decomposition of  $C$  is given in appendix E. The space-time formulation of system (5.6) has been solved using the non-linear blended scheme on three unsteady two-phase flow problems. The first and the second one are very well known tests for which has been possible to compare the solution obtained with analytical or experimental results. The third test has to be considered more as an application of the new space-time schemes to the simulation of relatively complex two-phase flows. In all the tests considered the gravity term played a major role, hence we could apply the new source term treatment.

### The Oscillating Manometer Problem

This is a rather simple 1D problem to set-up and it is very interesting since an analytical solution is available. It consists of a U shaped tube filled partially with liquid and partially with gas (see figure 5.42). The total length of the tube is 20 m, 10 m of which are filled with liquid. In the initial condition the liquid is at the bottom of the tube and both liquid

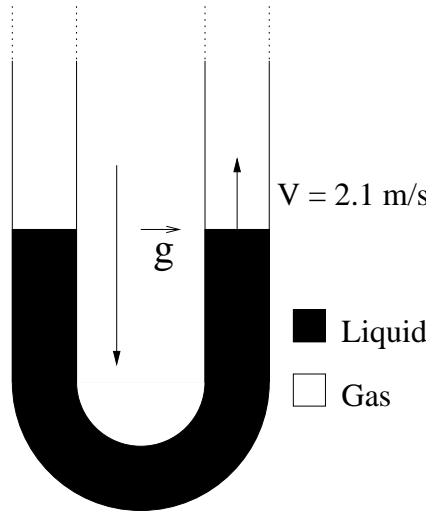


Figure 5.42: Oscillating Manometer: Problem Statement and Initial Condition

and gas are moving with the same speed. In the computations the tube has been considered one-dimensional and closed, so that simple periodic boundary conditions could be used at its extrema.

The initial condition is given by

$$[p, u, \alpha_g] = \begin{cases} [10^5, 2.1, 1] & \text{if } 0 \leq x \leq 5 \\ \left[ 10^5 + \rho_{l0} g \frac{L}{\pi} \sin\left(\frac{\pi(x-5)}{L}\right), 2.1, 0 \right] & \text{if } 5 \leq x \leq 15 \\ [10^5, 2.1, 1] & \text{if } 15 \leq x \leq 20 \end{cases},$$

where  $g = 9.81 \text{ m/s}^2$  is the magnitude of the gravity vector and  $L = 10 \text{ m}$  is the length of the liquid column. The effect of the curvature is taken into account in the initial pressure distribution in the liquid phase and in the gravity term which is defined as

$$\bar{g}(x) = \begin{cases} g & \text{if } 0 \leq x < 5 \\ g \cos\left(\frac{\pi(x-5)}{L}\right) & \text{if } 5 \leq x < 15 \\ -g & \text{if } 15 \leq x < 20 \end{cases}.$$

The problem has an analytical solution. In particular, the velocity at the bottom of the tube<sup>6</sup>  $u^*(t)$  is given by

$$u^*(t) = 2.1 \cos(\omega t), \quad \omega = \sqrt{2g/L}.$$

The computation was performed with two spatial resolutions and until time  $t = 15\text{s}$  which is slightly more than three periods of oscillation of the column. A first computation on 201 nodes was performed with different  $CFL$  numbers. In particular, thanks to the double layer approach, computations with  $CFL = 1$ ,  $CFL = 10$  and  $CFL = 20$  were performed.

---

<sup>6</sup> $x = 10\text{m}$

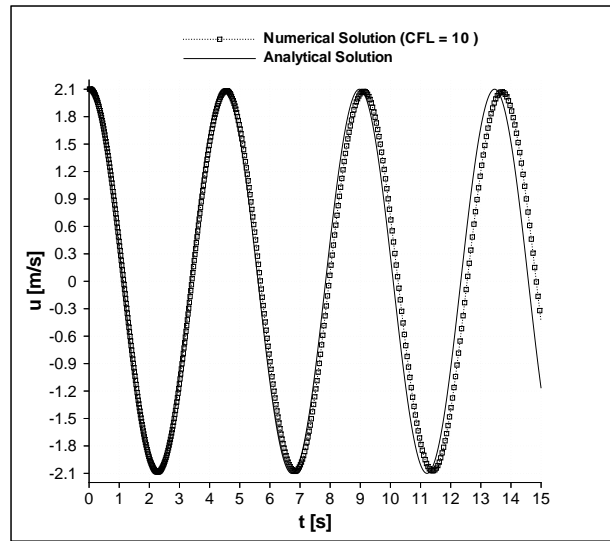
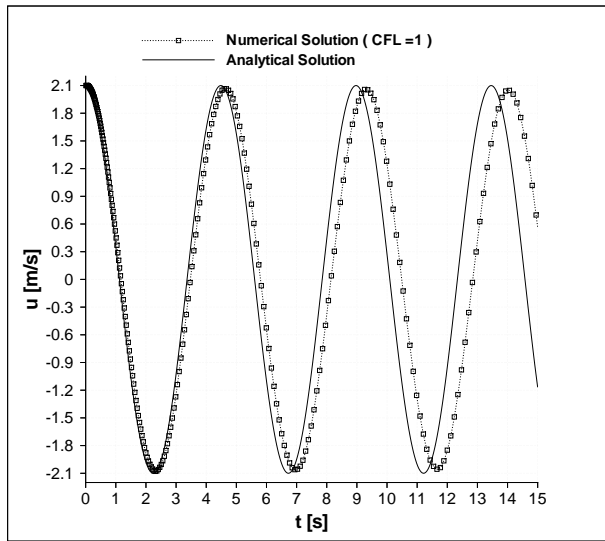


Figure 5.43: Oscillating Manometer Problem: Comparison with the Exact Solution. Left: 201 nodes -  $CFL = 1$ , Right: 201 nodes -  $CFL = 10$

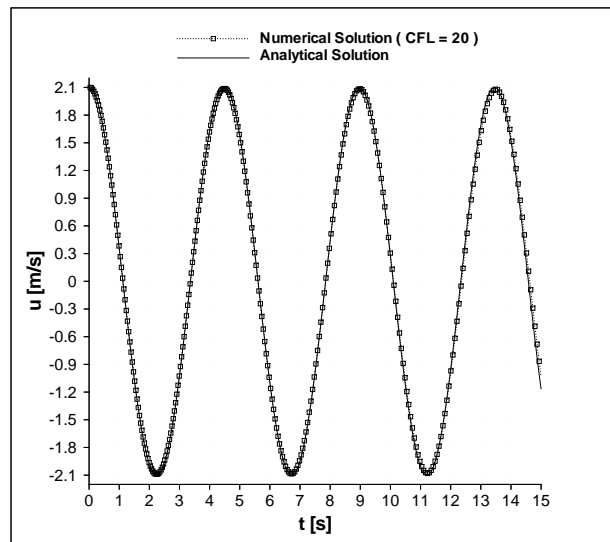
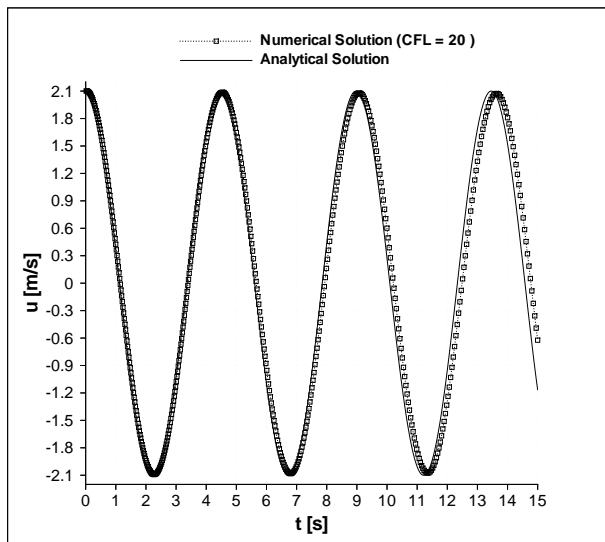


Figure 5.44: Oscillating Manometer Problem: Comparison with the Exact Solution. Left: 201 nodes -  $CFL = 20$ , Right: 401 nodes -  $CFL = 20$

The comparison between analytical solution and the solutions computed at different  $CFL$  numbers is shown in figure 5.43 and on the left in figure 5.44. Common feature of all the solutions is a very small numerical damping of the amplitude of the oscillation and an advancing phase error. Surprisingly, the smaller the  $CFL$  number, and hence the value of the time-step, the larger the phase error. This somehow contradicts the fact that for smaller time-steps one would expect a better time accuracy of the solution. The computation made with  $CFL = 20$  is indeed the best one, although a phase error is still visible. This can be attributed to the accumulation of the phase error in the computations made with smaller  $CFL$  numbers, due to the larger number of iterations needed to reach a fixed time with a smaller time-step.

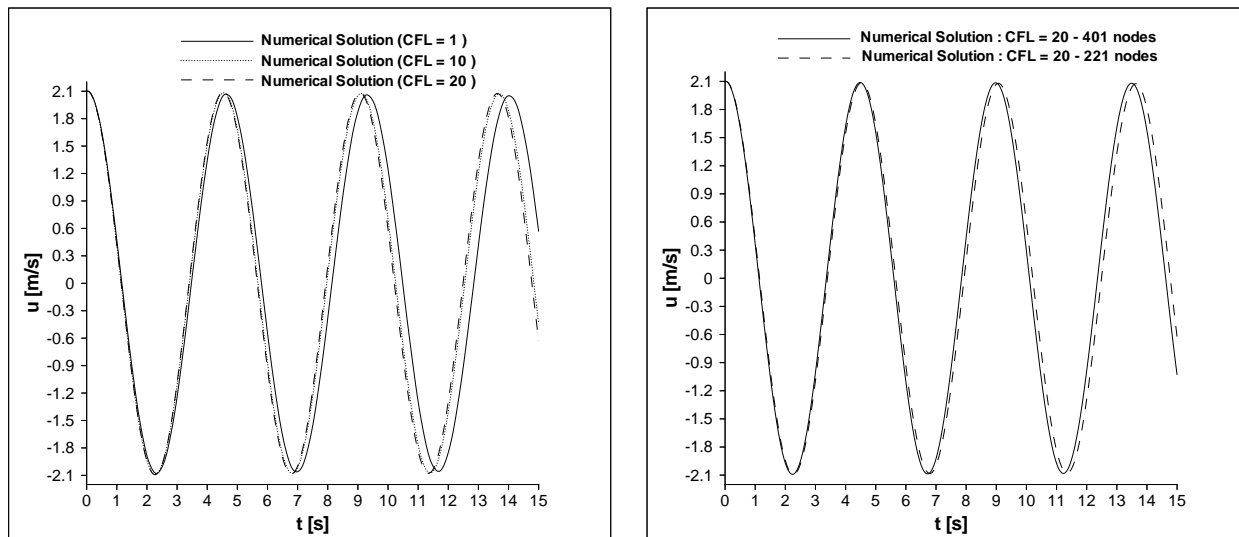


Figure 5.45: Oscillating Manometer Problem: Comparison with the Exact Solution. Left: 201 nodes - influence of  $CFL$  number, Right:  $CFL = 20$  - Influence of grid resolution

The advancing phase shift observed here seems to be consistent to the one observed in the computations of the transonic channel with fluctuating back-pressure. Whether the space-time treatment itself could introduce a phase error, when applied to non-linear equations, is not clear at the moment and further investigation of this aspect has to be done in the future. The computation at  $CFL = 20$  was repeated on a finer mesh containing 401 nodes. The result is reported on the right in figure 5.44. The agreement with the exact solution is very good, but a phase shift starts to be visible already at the beginning of the fourth cycle. Figure 5.45 summarizes the analysis made. As a matter of fact, the results obtained are not too bad, although the reasons of the advancing phase error should be investigated. Another important point is to perform some computations using the conservative formulation of the equations coupled with the new treatment of conservation, which will help to understand if the phase shift is related to the non-conservative approach used.

### Sloshing of a Water Column in a Tank

This problem has been used by several authors as a validation test for two-phase flow codes [5, 37] and has been also experimentally studied [36, 37]. The problem consists of a liquid column initially at rest in hydrostatic equilibrium in a tank. The height of the initial water column is  $2L$  and its width is  $L$ . The tank is a square with side  $4L$  and in the experiments its top side is open. Figure 5.46 summarizes the geometry of the problem.

At time  $t = 0$  the water column is left free to move and an instability due to gravity causes its break down. The water starts to move toward to opposite wall of the tank until it splashes against it and then moves back. Some experimental data are available in literature for the position of the leading edge of the moving liquid front. The distance of the front from the left wall of the tank  $Z$  scaled by the initial width of the water column  $L$  is given as a function of the reduced time  $t^*$  defined by

$$t^* = t\sqrt{2g/L},$$

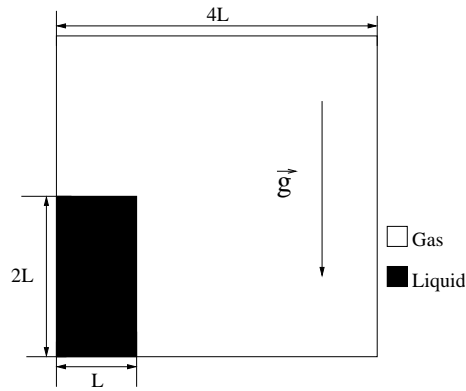


Figure 5.46: Sloshing of a Water Column: Geometry of the Problem and Initial Condition

being  $g$  the gravity acceleration. The initial column width used in the computations is  $L = 0.146$  m, which is the same used for the experiments in [37]. Unfortunately, because of the numerical diffusion, the interface between the phases is spread over several computational cells, so that a precise interface is not defined. What is usually done to compare with experimental data is to assume that the interface is located in the position where the gas void fraction assumes the value  $\alpha_g = 0.5$ . Using this criterion, the numerical position of the liquid front was compared with the experimental data of references [36, 37]. The numerical simulation was performed using the space-time formulation of system (5.6) and the non-linear blended scheme. The mesh used is an isotropic Delaunay mesh similar to the one in figure 5.19, containing 11804 nodes and 23206 triangles. The  $CFL$  number was fixed to 100. The comparison between the numerical prediction and the experimental data is shown in figure 5.47. The numerical results predict correctly the parabola-like behavior of the experimental data and it is also quantitatively very good at the earlier times of the movement of the water front, until  $t^* \approx 2$  which corresponds to a physical time  $t \approx 0.172$  s. The agreement worsens, although still qualitatively acceptable, at later times. The reason of this could be of course in the poor modeling of the physics. The model used is indeed one of the simplest one can think of. It does not include any viscous effect and, even more important, no modeling of the surface tension effects is included<sup>7</sup>. From the numerical point of view, a possible way of improving the result is certainly the use of a conservative approach that would guarantee a numerically correct prediction of the position of the interface which is not guaranteed by the present non-conservative formulation. Of course this would not overcome the problems related to the modeling issue.

The unsteady motion of the liquid mass has been also visualized plotting the isolines of the gas void fraction. The visualizations are reported in figures from 5.48 to 5.51, where the liquid phase is in blue and the gas phase in red. The initial condition is shown on the left in figure 5.48. On the right in the same figure the water column has already broken apart and it is moving toward the right end of the tank.

<sup>7</sup>The equilibrium of the stresses at the interface is probably what influences the real shape and motion of the interface

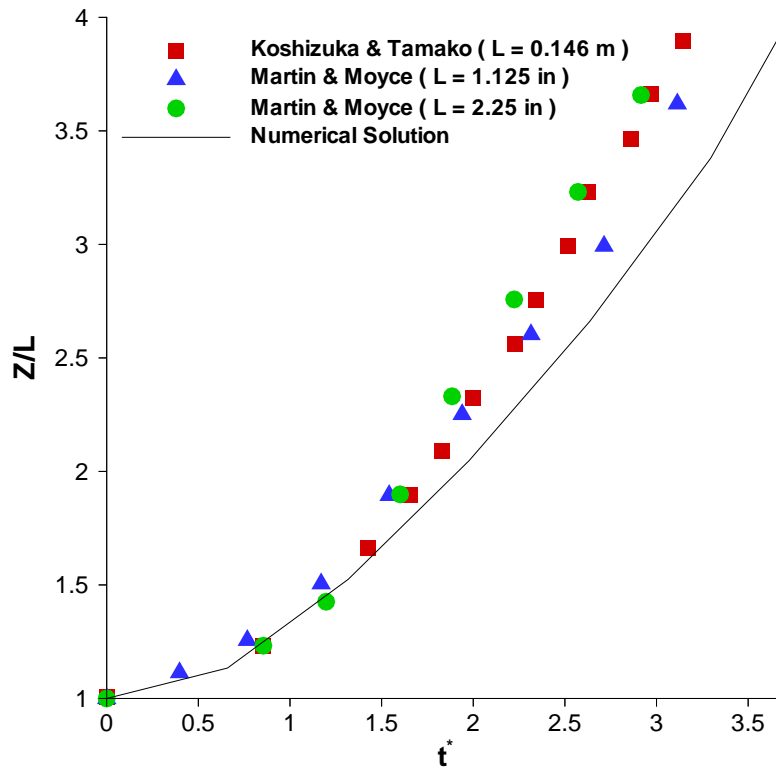


Figure 5.47: Sloshing of a Water Column: Comparison with Experimental Data

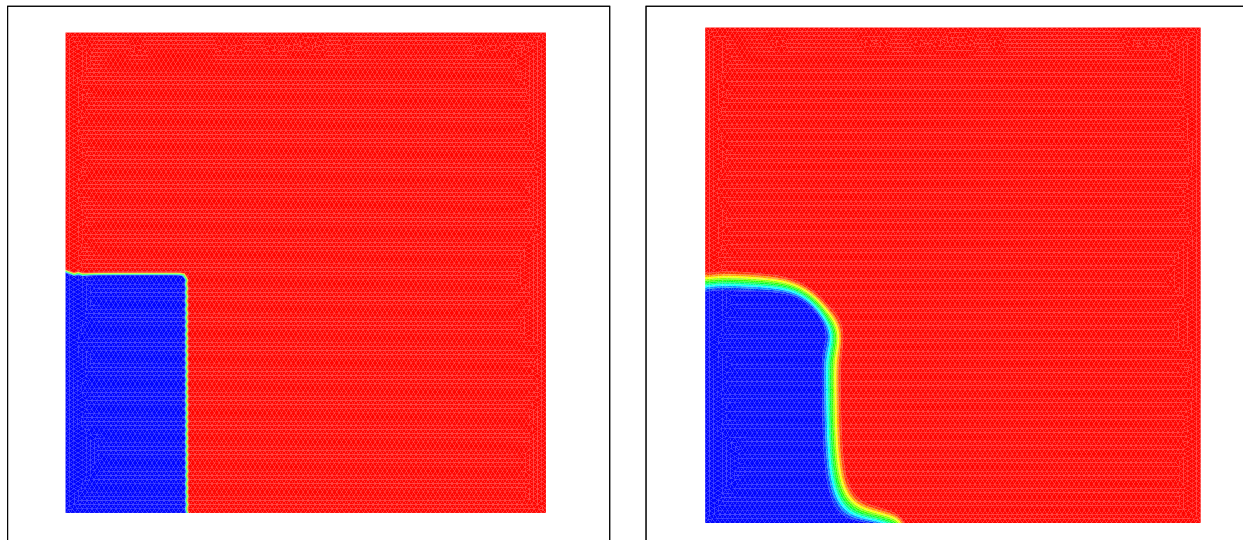


Figure 5.48: Sloshing of a Water Column: Gas Void Fraction. Left:  $t^* = 0$ , Right:  $t^* \approx 1.2$

On the right in figure 5.49 the liquid front has reached the wall and the splashing of the liquid on the wall is visible on the left in figure 5.50. The beginning of the sloshing of the water is finally shown on the right in figure 5.50 and in figure 5.51. In the caption of each picture the relative reduced time  $t^*$  is indicated.

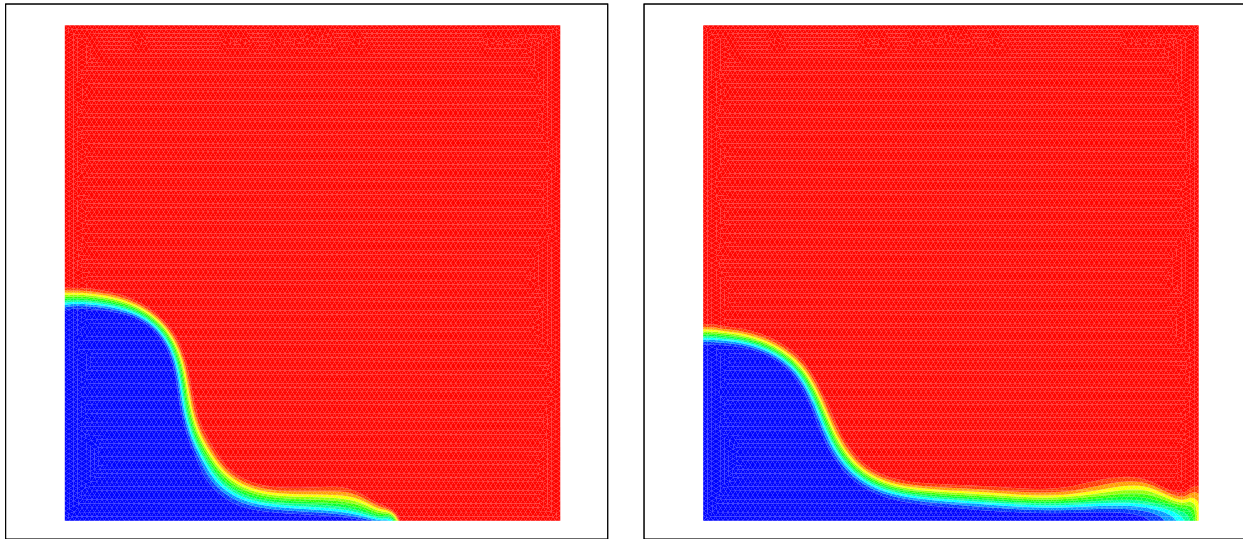


Figure 5.49: Sloshing of a Water Column: Gas Void Fraction. Left:  $t^* \approx 2.5$ , Right:  $t^* \approx 3.8$

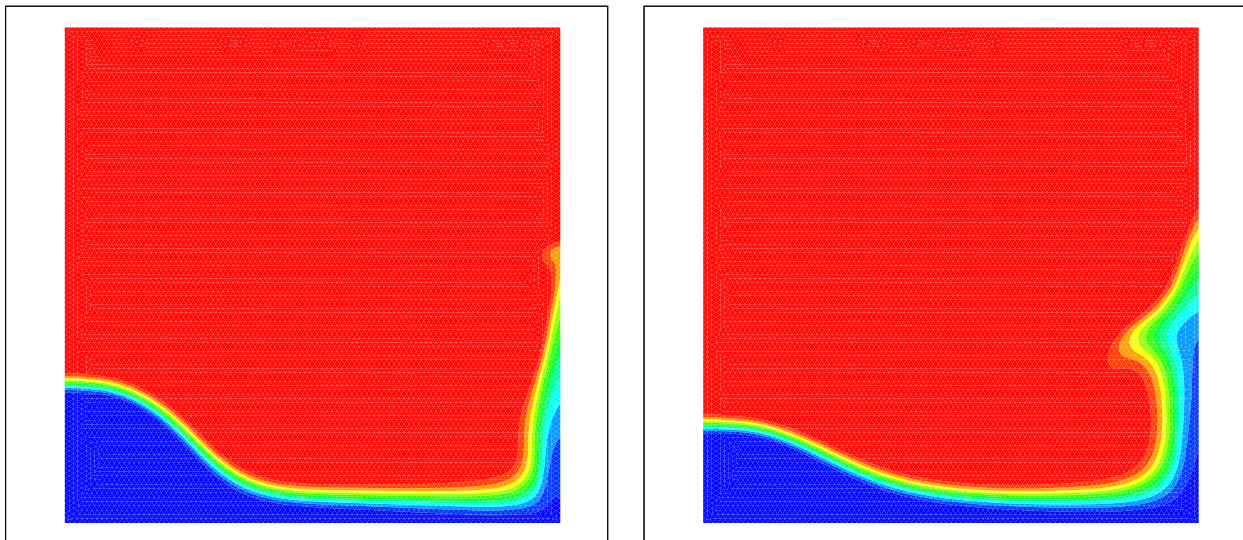


Figure 5.50: Sloshing of a Water Column: Gas Void Fraction. Left:  $t^* \approx 5.2$ , Right:  $t^* \approx 6.5$

The visualizations show the effect of the numerical diffusion spreading the void fraction discontinuity over a region covering several triangles. Note that the discontinuity in the void fraction is a linearly degenerated discontinuity, exactly like a slip line is for the Euler equations. As remarked when speaking about the Mach 3 flow over a forward step problem, the space-time schemes, because of the time upwinding, tend to badly smear this kind of discontinuities. As a last remark, it must be mentioned that, because the interface between the phases spreads over several cells, its position is not uniquely defined. In particular, the comparison with the experimental data of figure 5.47 was done assuming the interface to be located where the void fractions reach the value 0.5.

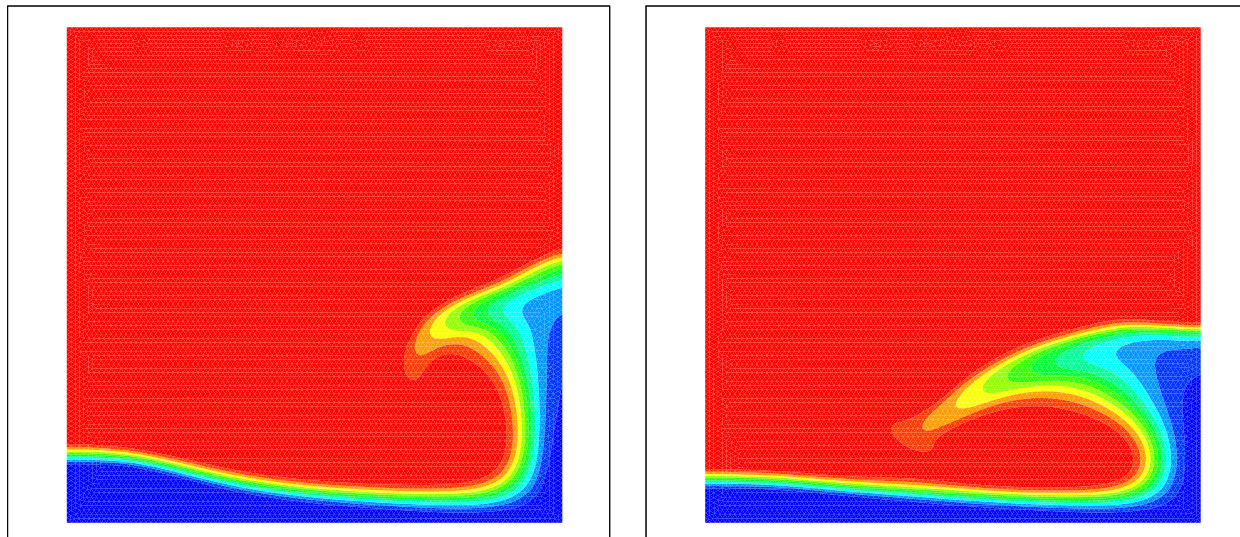


Figure 5.51: Sloshing of a Water Column: Gas Void Fraction. Left: $t^* \approx 7.8$ , Right: $t^* \approx 9$

### Gas Plume Test-Case

The evolution of a gas mass injected vertically into a liquid column initially at rest is considered here. The water is initially in hydrostatic equilibrium and the gas is injected with an inlet vertical velocity of 0.2 m/s. At the top the liquid phase is in contact with gas at atmospheric pressure. The injection starts at  $t = 0$  s and the entrainment of the gas phase into the liquid due to the formation of two symmetric vortices is observed. Given the symmetry of the problem, only half of it was simulated on a isotropic Delaunay grid (see figure 5.19) with a mesh-size  $h \approx 0.01$  corresponding to one tenth of the injection hole. System (5.6) was solved in its space-time formulation using the non-linear blended scheme and a  $CFL = 100$ . A similar test was performed in [5] with the same geometry, a higher injection speed and a much coarser mesh, solving system (5.6) with a first order residual distribution method. What is important to underline is that this test has a pure academical meaning, given the very simple model used<sup>8</sup> and the geometry of the problem<sup>9</sup>. The initial evolution of the injected gas, close to the inlet, and the formation of the two vortices is visualized using the isolines of the gas void fraction and the velocity vectors in figures from 5.52 to 5.55 where the red color denotes pure gas and the blue pure liquid. Note that the formation of the two counter-rotating vortices is related to the coupled effect of the gravity and of the equal velocity of the phases. Because of the last, in particular, in the regions where the void fraction goes from one to zero the liquid moves with the same velocity of the gas as if an infinite friction at the interface was acting<sup>10</sup>.

<sup>8</sup>Viscous and surface tension effects are not included

<sup>9</sup>The injection hole has a width of about 0.1 m which is practically too much to consider a jet of pure air

<sup>10</sup>Which is actually the basic assumption in the model

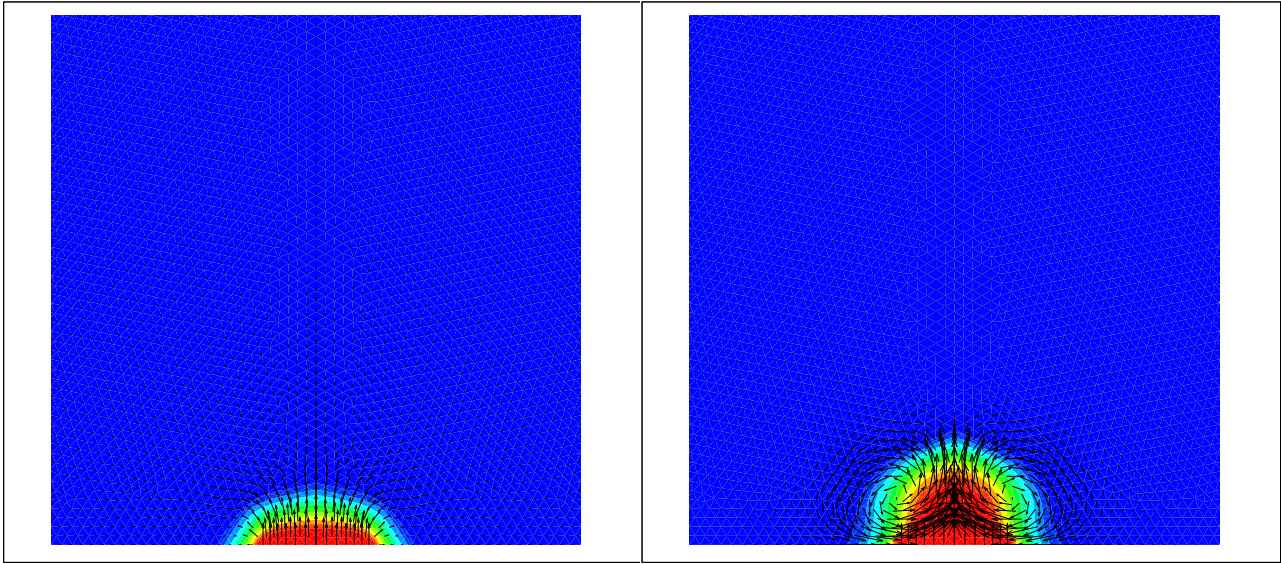


Figure 5.52: Gas Plume Problem: Gas Void Fraction at the inlet. Left:  $t = 0.2$  s, Right:  $t = 0.4$  s

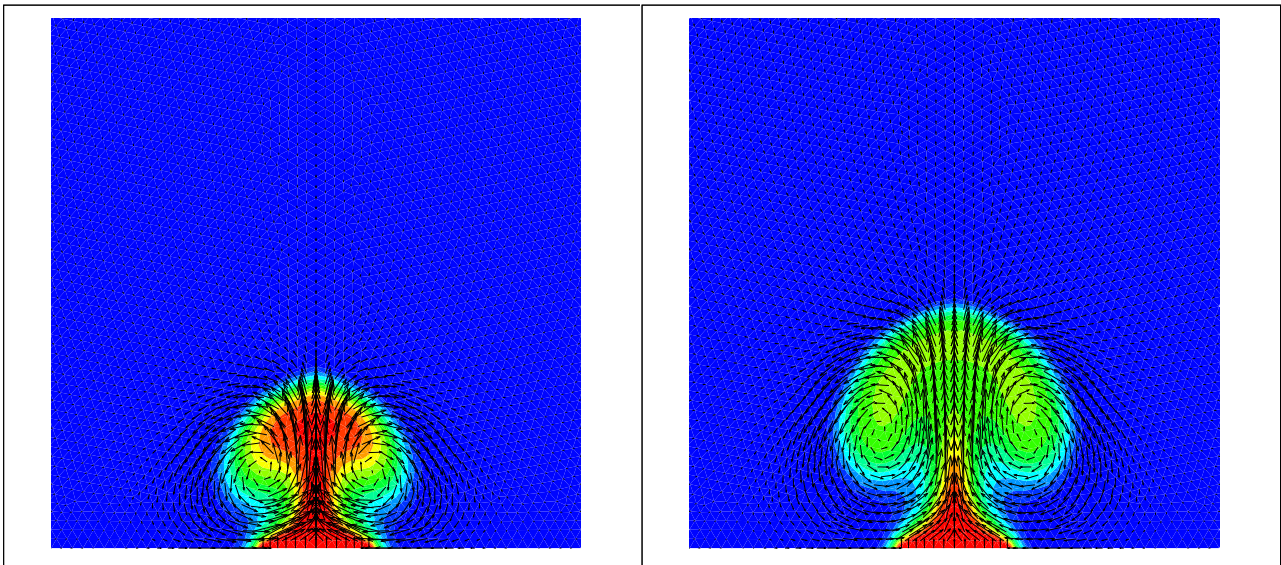


Figure 5.53: Gas Plume Problem: Gas Void Fraction at the inlet. Left:  $t = 0.6$  s, Right:  $t = 0.8$  s

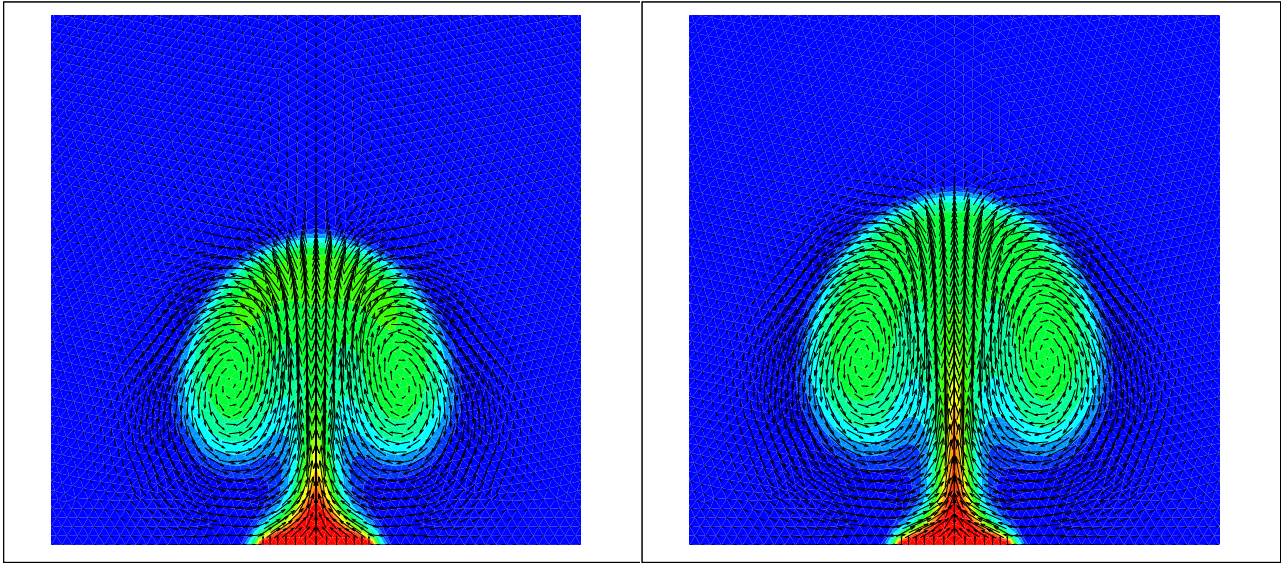


Figure 5.54: Gas Plume Problem: Gas Void Fraction at the inlet. Left:  $t = 1.0$  s, Right:  $t = 1.2$  s

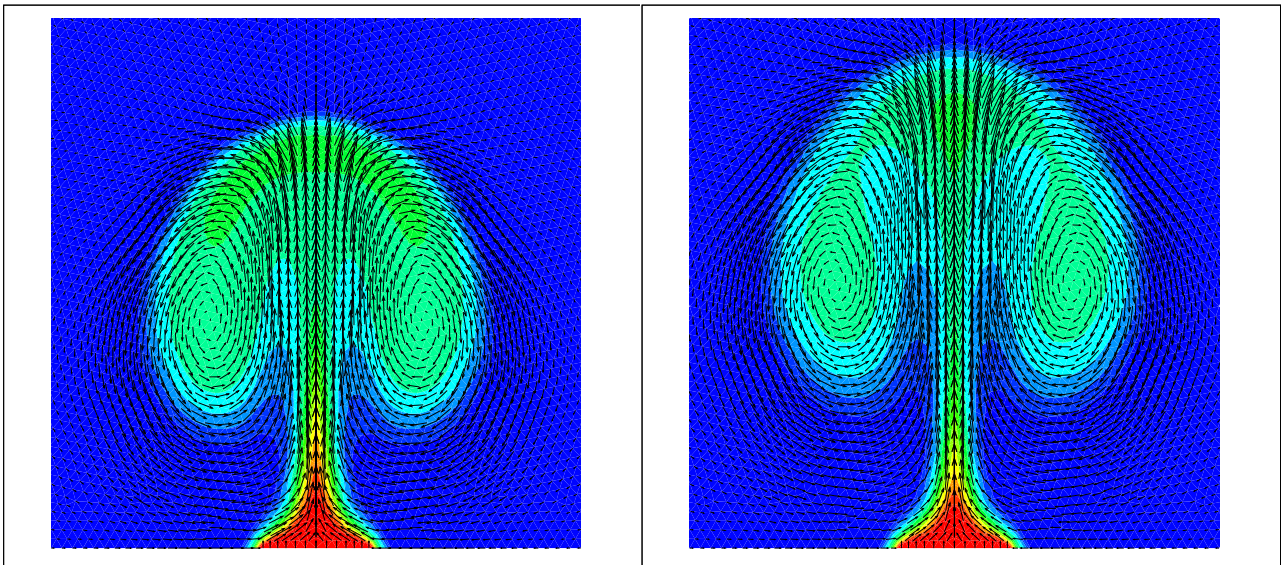


Figure 5.55: Gas Plume Problem: Gas Void Fraction at the inlet. Left:  $t = 1.4$  s, Right:  $t = 1.6$  s



# Chapter 6

## Conclusions, Final Remarks and Future Perspectives

### Achievements and Conclusions

The main goal of this project was to investigate the capabilities of a new Space-Time formulation of the Residual Distribution schemes and eventually to show its application to the simulation of unsteady two-phase flows on unstructured grids. The starting point was a code in which the basic method was implemented. The strategy adopted to reach the objective has been that of implementing step by step all the utilities and features needed to run more complex simulations and in parallel to develop the necessary theoretical background. Following this path the main achievements of the project can be summarized as follows

#### **Validation of the Code and of the Method**

Starting already with the initial version of the code, the new method has been intensively tested on a large number of problems, eventually comparing the solution obtained with reference solutions available in literature or with analytical solutions.

#### **Boundary Conditions**

To enlarge the capabilities of the code, a set of characteristics-based boundary conditions consistent with the nodal variable representation of the numerical method and based on the work done previously in [1] has been developed and analyzed, showing how to obtain an extension to implicit computations without the need of computing any numerical jacobian.

#### **Source Term Discretization**

To be able to perform two-phase flow simulations, there must be a way to include in the discretization the source terms present in the equations in a consistent manner which does not spoil the accuracy of the basic scheme and at the same time is robust enough to handle discontinuous or stiff sources. One possible way to do this has been developed and tested on rather severe problems within this project.

#### **New Conservative Formulation**

Residual Distribution schemes were born for the solution of multidimensional scalar ad-

vection problems and then later extended to the system of the Euler equations. This was possible thanks to their matrix formulation and to the extension of the Roe linearization to the multidimensional upwind method. A problem common to anybody willing to use the  $\mathcal{RD}$  method to solve a different system of equations is that, if no Roe linearization exists for the system, the method is not able to guarantee full conservation. The MHD equations, the equations of a chemically reacting flows and the two-phase Two-Fluid models are examples of systems for which no conservative linearization of the jacobians exists. Here, a new formulation of the  $\mathcal{RD}$  schemes has been proposed which guarantees full conservation without the need of any Roe-type linearization. The new approach has been tested and compared with the traditional formulation of the schemes.

### Application to Two-Phase Flows

The last item of this project was the application of the space-time approach to the simulation of two-phase flows. The model used is one of the simplest present in the literature, but still very interesting two-phase problems could be solved. The new theoretical results concerning source term discretization and conservation are of course of primary interest because they allow to discretize the two-phase flow equations in a consistent, accurate and conservative manner. Unfortunately, because of the time restrictions, the new conservative formulation could not be implemented, hence only the new treatment of the source term coupled with the space-time approach has been used.

The main achievements of the project are certainly the new developments relative to source terms and conservation. The results presented indeed prove their robustness although more testing is needed. The two-phase flow simulations have shown very promising results, besides the simple model used. As far as the space-time schemes are concerned, at the moment they are indeed the most robust and accurate formulation of the  $\mathcal{RD}$  schemes for unsteady simulation. As a matter of fact, in their present formulation, they are by far more expensive than a finite volume method coupled with a Runge-Kutta time integrator and their extension to three spatial dimensions<sup>1</sup> would probably not be competitive enough especially in terms of memory requirements. Nevertheless they could still be optimized and be very useful for two dimensional and axisymmetric computation. According to the author, the space-time schemes do not represent the ultimate way of performing accurate unsteady simulations using the  $\mathcal{RD}$  method.

## Future Perspectives

Several topics related to the work done deserve further attention

1. The strong node-wise boundary condition treatment used here, that allows a true control of the nodal value of the unknowns on the boundaries, should be implemented in an implicit solver and compared with the ghost-nodes approach used now in most of the  $\mathcal{RD}$  codes. In particular, the advantage of being able of computing analytically the new jacobian entries should be exploited.

---

<sup>1</sup>Apart from the trouble in extending the constrained space-time meshing to 4D

2. The new conservative formulation of the schemes enables to extend the use of the fluctuation splitting schemes to any system of equations. Of course one of the first items to take into consideration is to use it to solve the two-phase problems considered here. Further application to chemically reacting flows and to the MHD equations should be also tried.
3. A different use of the possibility of computing the cell residual through a numerical contour integration could be to build more accurate schemes. In fact, since the contour integral and hence the cell residual can be computed with any accuracy just by changing the quadrature rule, third order or even even more accurate schemes could be built. Two important issues have to be dealt with: how to define the residual distribution strategy and how to retain positivity when higher order polynomial representations of the variables are used. Help might come for the second issue from the work done in the field of the discontinuous Galerkin method [30].
4. Being able to perform 3D accurate unsteady computations using residual distribution schemes still remain a challenge, since the space-time approach would probably be too expensive. A way to go could be to go back to the finite elements formulation of the schemes, coupling it with the ideas at the basis of stabilized finite elements methods. A blending of the consistent mass matrix with the lumped one could be one of the first things to try. Following the work of Sidilkover [38] the computation of the blending coefficient should be based on the time variation of the unknown. Investigation of the application to the time derivative of the same technique used for the discretization of the source terms and for the treatment of conservation could be also interesting
5. Even for two dimensional and axisymmetric flows, the space-time schemes are very expensive and a long computational time can be required also for simple problems. The explicit pseudo-time iterative procedure in use at the moment could be abandoned in favor of a Newton or quasi-Newton iterative method, but the large memory requirements associated to the method have to be kept in mind.
6. Cheaper space-time meshing techniques, like the one proposed in [22], should be considered.
7. The dual time loop intrinsic in the space-time method of solution could be easily used to perform incompressible flow simulation by the use of the artificial compressibility approach.
8. Dual time preconditioning techniques could be easily coupled with the space-time method, thanks to its intrinsic dual time-stepping formulation.



# Appendix A

## Consistency of the $N^S$ Scheme in 1D

It is known that the 1D upwind finite volume Roe scheme can be rewritten as a  $\mathcal{RD}$  scheme (see [1, 26]). In particular, with reference to figure A.1, scheme (3.6) can be rewritten as

$$\begin{aligned} (\Phi_i^e)^{UP} &= \hat{A}_e^-(U_{i+1} - U_i) - \frac{I - \text{sgn}(\hat{A}_e) \Delta x}{2} (S_i + S_{i+1}) \\ (\Phi_i^{e-1})^{UP} &= \hat{A}_{e-1}^+(U_i - U_{i-1}) - \frac{I + \text{sgn}(\hat{A}_{e-1}) \Delta x}{2} (S_i + S_{i-1}) \end{aligned} \quad ,$$

and similarly for the nodes  $i + 1$  and  $i - 1$ .

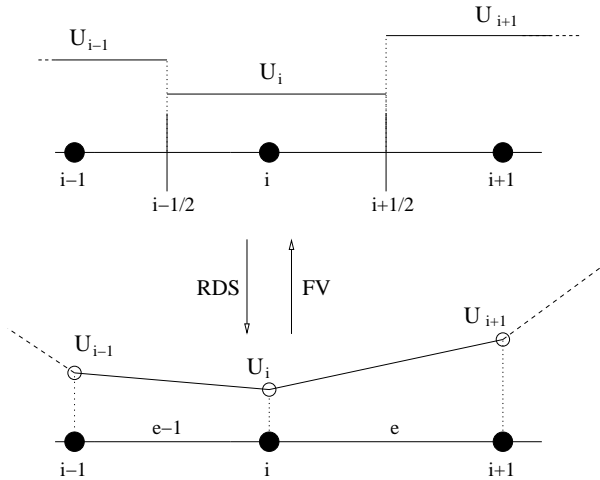


Figure A.1:  $\mathcal{RD}$  formulation of a 1D Finite Volume Scheme

In order to derive the 1D version of scheme (3.4) consider the following relations:

$$\left\{ \begin{array}{l} K_i^e = -A \quad \rightarrow \quad K_i^- = \frac{-A - |A|}{2} = -A^+ = -\frac{I + \text{sgn}(A)}{2} A \\ \quad \quad \quad \rightarrow \quad K_i^+ = \frac{-A + |A|}{2} = -A^- = \frac{-I + \text{sgn}(A)}{2} A \\ \quad \quad \quad \rightarrow \quad I_i^+ = K_i^+ (K_i^e)^{-1} = \frac{-I + \text{sgn}(A)}{2} \\ K_{i+1}^e = A \quad \rightarrow \quad K_{i+1}^- = A^- = \frac{I - \text{sgn}(A)}{2} A \\ \quad \quad \quad \rightarrow \quad K_{i+1}^+ = A^+ = \frac{I + \text{sgn}(A)}{2} A \\ \quad \quad \quad \rightarrow \quad I_{i+1}^+ = K_{i+1}^+ (K_{i+1}^e)^{-1} = \frac{I + \text{sgn}(A)}{2} \\ \quad \quad \quad \rightarrow \quad \sum_{j \in e} K_j^+ = -\sum_{j \in e} K_j^- = |A| \quad , \quad \sum_{j \in e} I_j^+ = I \end{array} \right. \quad . \quad (\text{A.1})$$

Note that the subscript  $e$  has been dropped for clearness.

The source term fluctuation (3.5) is given by

$$\Phi^S = S_i^* + S_{i+1}^* = \frac{\Delta x}{2} S_i + \frac{\Delta x}{2} S_{i+1} ,$$

and the inflow states can be proven to be

$$\begin{aligned} S_{in}^* &= \frac{I - \mathbf{sgn}(A)}{2} S_i^* + \frac{I + \mathbf{sgn}(A)}{2} S_{i+1}^* + \Phi^S \\ U_{in} &= \frac{I + \mathbf{sgn}(A)}{2} U_i + \frac{I - \mathbf{sgn}(A)}{2} U_{i+1} . \end{aligned}$$

Then, according to (3.4) and using relations (A.1), the element-to-node contribution for node  $i$  from element  $e$  is

$$(\Phi_i^e)^{N,S} = -A^- (U_i - U_{in}) + \frac{I - \mathbf{sgn}(A)}{2} (S_i^* - S_{in}^*) . \quad (\text{A.2})$$

For the first term in the last equation one has

$$\begin{aligned} -A^- (U_i - U_{in}) &= \\ -A^- U_i + \frac{I - \mathbf{sgn}(A)}{2} A \frac{I + \mathbf{sgn}(A)}{2} U_i + \frac{I - \mathbf{sgn}(A)}{2} A \frac{I - \mathbf{sgn}(A)}{2} U_{i+1} &= \\ -A^- U_i + A^{-1} A^- A^+ U_i + \frac{1}{4} (A - |A|) (I - \mathbf{sgn}(A)) U_{i+1} &= -A^- U_i + A^- U_{i+1} , \quad (\text{A.3}) \end{aligned}$$

and finally

$$-A^- (U_i - U_{in}) = A^- (U_{i+1} - U_i) .$$

Note that in equation (A.3) the relation  $A^- A^+ = 0$ , the definition of the sign of a matrix (equation (3.8)) and the fact that  $\mathbf{sgn}(A) = \mathbf{sgn}(A^{-1})$  has been used. For the second term in equation (A.2) one has

$$\begin{aligned} \frac{I - \mathbf{sgn}(A)}{2} (S_i^* - S_{in}^*) &= \\ \frac{I - \mathbf{sgn}(A)}{2} \left( S_i^* - \frac{I - \mathbf{sgn}(A)}{2} S_i^* + \frac{I + \mathbf{sgn}(A)}{2} S_{i+1}^* - \Phi^S \right) &= \\ -\frac{I - \mathbf{sgn}(A)}{2} \Phi^S + \frac{I - \mathbf{sgn}(A)}{2} \left( \frac{I + \mathbf{sgn}(A)}{2} S_i^* - \frac{I + \mathbf{sgn}(A)}{2} S_{i+1}^* \right) &= \\ -\frac{I - \mathbf{sgn}(A)}{2} \Phi^S + \frac{I - \mathbf{sgn}(A)}{2} \frac{I + \mathbf{sgn}(A)}{2} (S_i^* - S_{i+1}^*) &= \\ -\frac{I - \mathbf{sgn}(A)}{2} \Phi^S + A^{-1} A^- A^+ A^{-1} (S_i^* - S_{i+1}^*) &= -\frac{I - \mathbf{sgn}(A)}{2} \Phi^S . \end{aligned}$$

Assembling the two contributions and writing explicitly the source term fluctuation one ends with

$$(\Phi_i^e)^{N,S} = \hat{A}_e^- (U_{i+1} - U_i) - \frac{I - \mathbf{sgn}(\hat{A}_e)}{2} \frac{\Delta x}{2} (S_i + S_{i+1}) = (\Phi_i^e)^{UP} .$$

Similarly one can prove that  $(\Phi_i^{e-1})^{N,S} = (\Phi_i^{e-1})^{UP}$ .

# Appendix B

## The New N Scheme is $\mathcal{IST}$

Consider the scheme given by the combination of the  $N^S$  and the  $N^c$  schemes introduced in chapter 3:

$$\Phi_j = I_j^+ [K_j^T (U_j - U_c) + S_j^* - S_{in}^*] ,$$

being

$$S_{in}^* = \left( \sum_{l \in T} I_l^+ \right)^{-1} \left( \sum_{l \in T} I_l^+ S_l^* + \Phi^S \right) , \quad U_c = \left( \sum_{j \in T} K_j^+ \right)^{-1} \left( \sum_{j \in T} K_j^+ U_j - \Phi^T \right) ,$$

and

$$\Phi^T = \oint_{\partial T} \vec{F} \cdot \vec{n} \, dl \quad , \quad \Phi^S = \int_T S \, d\Omega .$$

What we would like to do is to extend the proof of the  $\mathcal{IST}$  property also to this scheme. In order to do this, consider two sets of variables  $U$  and  $W$ , linked by the relation

$$\partial W = \frac{\partial W}{\partial U} \partial U .$$

It is easy to prove that

$$K_j^U = \frac{\partial U}{\partial W} K_j^W \frac{\partial W}{\partial U} ,$$

and hence

$$K_j^{\pm W} = \frac{\partial W}{\partial U} K_j^{\pm U} \frac{\partial U}{\partial W} , \quad I_j^{+W} = \frac{\partial W}{\partial U} I_j^{+U} \frac{\partial U}{\partial W} . \quad (\text{B.1})$$

Suppose  $U$  is the vector of conserved variables, of course  $\Phi^T$  must be computed using the conservative fluxes, hence  $\Phi^T = \Phi^{T,U}$ . Suppose that also  $\Phi^S$  is computed in conservative variables, consistently with what is done for the fluxes. So we also have  $\Phi^S = \Phi^{S,U}$ . Define now the following quantities

$$\Phi^{T,W} = \frac{\partial W}{\partial U} \Phi^{T,U} , \quad \Phi^{S,W} = \frac{\partial W}{\partial U} \Phi^{S,U} , \quad S_i^{*,W} = \frac{\partial W}{\partial U} S_i^* , \quad W_i = \frac{\partial W}{\partial U} U_i . \quad (\text{B.2})$$

The nodal residual of the new scheme will be computed in the  $W$  variables as

$$\Phi_j^W = I_j^{+W} \left[ K_j^W (W_j - W_c) + S_j^{*,W} - S_{in}^{*,W} \right] ,$$

with

$$S_{in}^{*,W} = \left( \sum_{l \in T} I_l^{+,W} \right)^{-1} \left( \sum_{l \in T} I_l^{+,W} S_l^{*,W} + \Phi^{S,W} \right), \quad W_c = \left( \sum_{j \in T} K_j^{+,W} \right)^{-1} \left( \sum_{j \in T} K_j^{+,W} W_j - \Phi^{T,W} \right).$$

Using relations (B.1) and (B.2) one can easily check that

$$S_{in}^{*,W} = \frac{\partial W}{\partial U} S_{in}^* \quad , \quad W_c = \frac{\partial W}{\partial U} U_c \quad ,$$

and hence, using again (B.2)

$$\Phi_j^W = I_j^{+W} \left[ K_j^W \frac{\partial W}{\partial U} (U_j - U_c) + \frac{\partial W}{\partial U} (S_j^* - S_{in}^*) \right].$$

Applying one last time (B.1) to last equation, one can write

$$\Phi_j^W = \frac{\partial W}{\partial U} I_j^{+U} \left[ \frac{\partial U}{\partial W} \frac{\partial W}{\partial U} K_j^U \frac{\partial U}{\partial W} \frac{\partial W}{\partial U} (U_j - U_c) + \frac{\partial U}{\partial W} \frac{\partial W}{\partial U} (S_j^* - S_{in}^*) \right],$$

and finally

$$\Phi_j^W = \frac{\partial W}{\partial U} I_j^{+U} [K_j^U (U_j - U_c) + S_j^* - S_{in}^*] = \frac{\partial W}{\partial U} \Phi_j^U \quad ,$$

hence the new scheme is  $\mathcal{IST}$ .

# Appendix C

## Flux Computations

### C.1 Second Order Flux Integration

The proof of relation (3.12) will be given here, first in the case of a triangle and then for a tetrahedron. Consider then the triangle of figure C.1; applying the trapezium rule one obtains

$$\begin{aligned} \oint_{\partial T} \vec{\mathcal{F}} \cdot \vec{n} \, dl &= -\frac{1}{2} (\vec{\mathcal{F}}_0 + \vec{\mathcal{F}}_1) \cdot \vec{n}_2 - \frac{1}{2} (\vec{\mathcal{F}}_1 + \vec{\mathcal{F}}_2) \cdot \vec{n}_0 - \frac{1}{2} (\vec{\mathcal{F}}_2 + \vec{\mathcal{F}}_0) \cdot \vec{n}_1 = \\ &= -\frac{1}{2} \vec{\mathcal{F}}_0 \cdot (\vec{n}_1 + \vec{n}_2) - \frac{1}{2} \vec{\mathcal{F}}_1 \cdot (\vec{n}_0 + \vec{n}_2) - \frac{1}{2} \vec{\mathcal{F}}_2 \cdot (\vec{n}_0 + \vec{n}_1) . \end{aligned}$$

Using the relation  $\vec{n}_0 + \vec{n}_1 + \vec{n}_2 = \vec{0}$ , one ends with

$$\oint_{\partial T} \vec{\mathcal{F}} \cdot \vec{n} \, dl = \frac{1}{2} (\vec{\mathcal{F}}_0 \cdot \vec{n}_0 + \vec{\mathcal{F}}_1 \cdot \vec{n}_1 + \vec{\mathcal{F}}_2 \cdot \vec{n}_2) ,$$

that is exactly what (3.12) says.

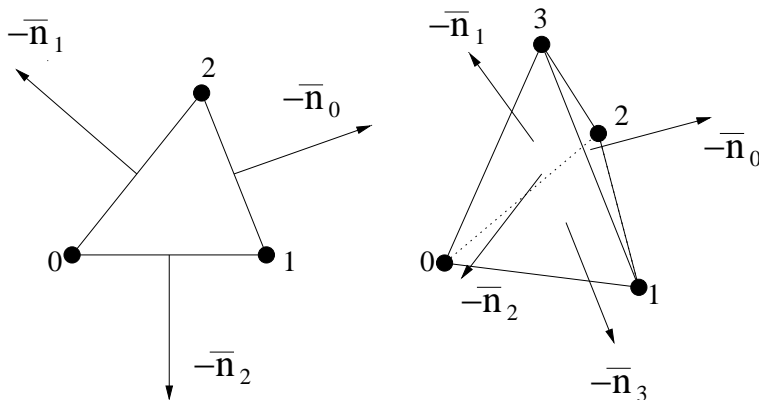


Figure C.1: Contour Integration with Trapezium Rule

In the case of a tetrahedron the trapezium rule becomes

$$\begin{aligned} \oint_{\partial T} \vec{\mathcal{F}} \cdot \vec{n} \, dl &= \\ &= -\frac{(\vec{\mathcal{F}}_0 + \vec{\mathcal{F}}_1 + \vec{\mathcal{F}}_2)}{3} \cdot \vec{n}_3 - \frac{(\vec{\mathcal{F}}_1 + \vec{\mathcal{F}}_2 + \vec{\mathcal{F}}_3)}{3} \cdot \vec{n}_0 - \frac{(\vec{\mathcal{F}}_0 + \vec{\mathcal{F}}_2 + \vec{\mathcal{F}}_3)}{3} \cdot \vec{n}_1 - \frac{(\vec{\mathcal{F}}_0 + \vec{\mathcal{F}}_1 + \vec{\mathcal{F}}_3)}{3} \cdot \vec{n}_2 \\ &= -\vec{\mathcal{F}}_0 \cdot \frac{\vec{n}_1 + \vec{n}_2 + \vec{n}_3}{3} - \vec{\mathcal{F}}_1 \cdot \frac{\vec{n}_0 + \vec{n}_2 + \vec{n}_3}{3} - \vec{\mathcal{F}}_2 \cdot \frac{\vec{n}_0 + \vec{n}_1 + \vec{n}_3}{3} - \vec{\mathcal{F}}_3 \cdot \frac{\vec{n}_0 + \vec{n}_1 + \vec{n}_2}{3}. \end{aligned}$$

Using the relation  $\vec{n}_0 + \vec{n}_1 + \vec{n}_2 + \vec{n}_3 = \vec{0}$ , one ends with

$$\oint_{\partial T} \vec{\mathcal{F}} \cdot \vec{n} \, dl = \frac{1}{3} \left( \vec{\mathcal{F}}_0 \cdot \vec{n}_0 + \vec{\mathcal{F}}_1 \cdot \vec{n}_1 + \vec{\mathcal{F}}_2 \cdot \vec{n}_2 + \vec{\mathcal{F}}_3 \cdot \vec{n}_3 \right),$$

as we wanted to prove.

## C.2 Third Order Flux Integration

Using the notation of figure C.2, Simpson's rule contour integration reads:

$$\begin{aligned} \oint_{\partial T} \vec{\mathcal{F}} \cdot \vec{n} \, dl &= \\ &= -\frac{1}{3} \left( \frac{1}{2} \vec{\mathcal{F}}_0 + 2\vec{\mathcal{F}}_{m_2} + \frac{1}{2} \vec{\mathcal{F}}_1 \right) \cdot \vec{n}_2 - \frac{1}{3} \left( \frac{1}{2} \vec{\mathcal{F}}_1 + 2\vec{\mathcal{F}}_{m_0} + \frac{1}{2} \vec{\mathcal{F}}_2 \right) \cdot \vec{n}_0 - \frac{1}{3} \left( \frac{1}{2} \vec{\mathcal{F}}_2 + 2\vec{\mathcal{F}}_{m_1} + \frac{1}{2} \vec{\mathcal{F}}_0 \right) \cdot \vec{n}_1 = \\ &= -\frac{1}{3} \left[ \frac{1}{2} \vec{\mathcal{F}}_0 \cdot (\vec{n}_1 + \vec{n}_2) + \frac{1}{2} \vec{\mathcal{F}}_1 \cdot (\vec{n}_0 + \vec{n}_2) + \frac{1}{2} \vec{\mathcal{F}}_2 \cdot (\vec{n}_0 + \vec{n}_1) + 2\vec{\mathcal{F}}_{m_0} \cdot \vec{n}_0 + 2\vec{\mathcal{F}}_{m_1} \cdot \vec{n}_1 + 2\vec{\mathcal{F}}_{m_2} \cdot \vec{n}_2 \right]. \end{aligned}$$

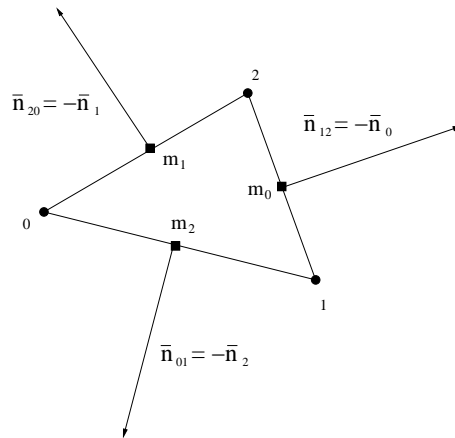


Figure C.2: Contour Integration on a Triangle with Simpson's Rule

Using the relation  $\vec{n}_0 + \vec{n}_1 + \vec{n}_2 = \vec{0}$  one ends with

$$\oint_{\partial T} \vec{\mathcal{F}} \cdot \vec{n} \, dl = \frac{1}{3} \left( \frac{1}{2} \vec{\mathcal{F}}_0 - 2\vec{\mathcal{F}}_{m_0} \right) \cdot \vec{n}_0 + \frac{1}{3} \left( \frac{1}{2} \vec{\mathcal{F}}_1 - 2\vec{\mathcal{F}}_{m_1} \right) \cdot \vec{n}_1 + \frac{1}{3} \left( \frac{1}{2} \vec{\mathcal{F}}_2 - 2\vec{\mathcal{F}}_{m_2} \right) \cdot \vec{n}_2 ,$$

exactly as stated by equation (3.13).



# Appendix D

## Boundary Conditions

Consider the following update formula:

$$U_i^{n+1} = U_i^n - k_{i\Delta} \mathbf{R}_i ,$$

where the coefficient  $k_{i\Delta}$  is a function of the time-step and of the local geometry, for example  $k_{i\Delta} = \Delta t/S_i$ . The correction related to the boundary treatment will be of the type

$$\delta U^* = \sum_{\lambda_k^i > 0} \beta^k \mathbf{r}^k ,$$

where  $\mathbf{r}^k$  is the right eigenvector relative to the  $k$ -th positive eigenvalue of the jacobian of the differential system  $\lambda_k^i$  (see section 4.1). The final update formula becomes

$$U_i^{n+1} = U_i^n - k_{i\Delta} \mathbf{R}_i + \delta U^* = U_i^n - k_{i\Delta} (\mathbf{R}_i + \mathbf{R}_i^*) \rightarrow \mathbf{R}_i^* = -\frac{1}{k_{i\Delta}} \sum_{\lambda_k^i > 0} \beta^k \mathbf{r}^k .$$

Since the eigenvectors  $\mathbf{r}^k$  are known analytically, the only information missing is the one relative to the  $\beta^k$  coefficient. As already explained, they are computed from the imposition of the required boundary condition on  $U_i^{n+1}$ . Instead of giving the general procedure to compute the coefficients, here the way they were computed for the Euler equations will be reported as an example. In a second section the value of the  $\beta^k$  coefficient for imposing the boundary conditions for the Two-Fluid model are also given. For their computation one can refer to [5].

### D.1 Euler Equations

#### Inviscid Wall Condition for the 2D Euler equations

The condition we want to impose is either  $\Delta u_\perp = 0$  or  $u_\perp^{n+1} = 0$ . What we need to compute is the provisional increment  $\delta U_i$  of our variables and then derive an equation for  $\beta^w$ . Indicate with  $P = [\rho, u, v, p]^t$  the vector of primitive variables, one has in a first order approximation

$$\delta P_i = \left( \frac{\partial P}{\partial U} \right)_i^n \delta U_i = -k_{i\Delta} \left( \frac{\partial P}{\partial U} \right)_i^n \mathbf{R}_i ,$$

where the jacobian  $\partial P/\partial U$  is known analytically (see appendix E). The last expression gives for the provisional increment of the primitive variables

$$\begin{aligned}\delta\rho &= -k_{i\Delta} (\mathbf{R}_i)_1 \\ \delta u &= -k_{i\Delta} \frac{(\mathbf{R}_i)_2 - u_i^n (\mathbf{R}_i)_1}{\rho_i^n} \\ \delta v &= -k_{i\Delta} \frac{(\mathbf{R}_i)_3 - v_i^n (\mathbf{R}_i)_1}{\rho_i^n} , \\ \delta p &= (\gamma - 1) [-k_{i\Delta} (\mathbf{R}_i)_4 - k_{ei}^n \delta\rho - \rho_i^n (u_i^n \delta u + v_i^n \delta v)]\end{aligned}$$

where  $k_{ei}^n$  is the kinetic energy per unit mass. In the case of wall boundary conditions, there is only one ingoing wave associated to the eigenvalue  $\vec{u} \cdot \vec{n}_i + a$ , with relative eigenvector given in primitive variables as follows (see appendix E)

$$\mathbf{r}^w = \begin{bmatrix} \rho_i^n / a_i^n \\ n_{ix} \\ n_{iy} \\ \rho_i^n a_i^n \end{bmatrix} .$$

Writing the final update in primitive variables, one obtains for the velocity components

$$\begin{aligned}u_i^{n+1} &= u_i^n + \delta u + \beta^w n_{ix} \\ v_i^{n+1} &= v_i^n + \delta v + \beta^w n_{iy} ,\end{aligned}$$

and finally multiplying the first equation by  $n_{ix}$ , the second by  $n_{iy}$  and remembering that  $n_{ix}^2 + n_{iy}^2 = 1$ , one obtains for  $u_{\perp}^{n+1}$  and  $\Delta u_{\perp}$

$$u_{\perp}^{n+1} = u_{\perp}^n + \delta u_{\perp} + \beta^w \rightarrow \Delta u_{\perp} = \delta u_{\perp} + \beta^w ,$$

being  $\delta u_{\perp} = \delta u n_{ix} + \delta v n_{iy}$ . Finally the value of  $\beta^k$  is obtained simply by setting  $u_{\perp}^{n+1} = 0$  or  $\Delta u_{\perp} = 0$ :

$$\begin{aligned}u_{\perp}^{n+1} = 0 &\rightarrow \beta^w = -(u_{\perp}^n + \delta u_{\perp}) \\ \Delta u_{\perp} = 0 &\rightarrow \beta^w = -\delta u_{\perp} .\end{aligned}$$

Note that  $\beta^w$  can be written as the following linear combination of the values of the nodal residual:

$$\beta^w = \mathbf{D}^w(U_i) \cdot \mathbf{R}_i + c^w(U_i) , \quad \mathbf{D}^w(U_i) = \frac{k_{i\Delta}}{\rho} [ -u_{\perp}^n \quad n_x \quad n_y \quad 0 ]^t , \quad c^w(U_i) = -u_{\perp}^n .$$

## Subsonic Outlet Condition for the 1D Euler equations

Proceeding exactly as in the previous case, one obtains for the provisional increment of the primitive variables

$$\begin{aligned}\delta\rho &= -k_{i\Delta} (\mathbf{R}_i)_1 \\ \delta u &= -k_{i\Delta} \frac{(\mathbf{R}_i)_2 - u_i^n (\mathbf{R}_i)_1}{\rho_i^n} . \\ \delta p &= (\gamma - 1) [-k_{i\Delta} (\mathbf{R}_i)_3 - k_{ei}^n \delta\rho - \rho_i^n u_i^n \delta u]\end{aligned}$$

Also in this case the only ingoing wave is associated to the eigenvalue  $\vec{u} \cdot \vec{n}_i + a$ , with relative eigenvector given in primitive variables as (see appendix E)

$$\mathbf{r}^a = \begin{bmatrix} \rho_i^n / a_i^n \\ n_x / |n_x| \\ \rho_i^n a_i^n \end{bmatrix} .$$

Writing the final update in primitive variables one obtains for the pressure

$$p_i^{n+1} = p_i^n + \delta p + \beta^a \rho_i^n a_i^n ,$$

and finally  $\beta^a$  is obtained either imposing  $p_i^{n+1} = p_{out}(t^{n+1})$  or  $\Delta p = 0$ :

$$\begin{aligned} p_i^{n+1} = p_{out}(t^{n+1}) &\rightarrow \beta^a = \frac{1}{\rho_i^n a_i^n} (-\delta p + p_{out}(t^{n+1}) - p_i^n) \\ \Delta p = 0 &\rightarrow \beta^a = -\frac{\delta p}{\rho_i^n a_i^n} . \end{aligned}$$

Note that the expression of  $\beta^a$  is exactly the same for the 2D Euler equations. Making use of the definition of  $\delta p$ ,  $\beta^a$  can be easily expressed as  $\beta^a = \mathbf{D}^a(U_i) \cdot \mathbf{R}_i + c^a(u_i)$ . In particular one can easily show that in the 2D case

$$\mathbf{D}^a(U_i) = \frac{\gamma - 1}{\rho_i^n a_i^n} k_{i\Delta} [ k_{ei}^n \quad -u_i^n \quad -v_i^n \quad 1 ]^t , \quad c^a = \frac{p_{out}(t^{n+1}) - p_i^n}{\rho_i^n a_i^n} .$$

## Subsonic Inlet Condition for the 2D Euler equations

Because of the lengthy algebra, only the general procedure will be explained and the final results will be given. In this case there are three positive eigenvalues given by  $\vec{u} \cdot \vec{n}_i + a$  and  $\vec{u} \cdot \vec{n}_i$  two times. The eigenvectors associated to these eigenvalues are written in primitive variables as (see appendix E)

$$\mathbf{r}^1 = \begin{bmatrix} \rho_i^n / a_i^n \\ n_{ix} \\ n_{iy} \\ \rho_i^n a_i^n \end{bmatrix} , \quad \mathbf{r}^2 = \begin{bmatrix} 1 \\ 0 \\ 0 \\ 0 \end{bmatrix} , \quad \mathbf{r}^3 = \begin{bmatrix} 0 \\ -n_{iy} \\ n_{ix} \\ 0 \end{bmatrix} .$$

As in the case of the wall boundary conditions, one can easily derive the provisional increment for the primitive variables:

$$\begin{aligned} \delta \rho &= -k_{i\Delta} (\mathbf{R}_i)_1 \\ \delta u &= -k_{i\Delta} \frac{(\mathbf{R}_i)_2 - u_i^n (\mathbf{R}_i)_1}{\rho_i^n} \\ \delta v &= -k_{i\Delta} \frac{(\mathbf{R}_i)_3 - u_i^n (\mathbf{R}_i)_1}{\rho_i^n} \\ \delta p &= (\gamma - 1) [-k_{i\Delta} (\mathbf{R}_i)_4 - k_{ei}^n \delta \rho - \rho_i^n (u_i^n \delta u + v_i^n \delta v)] \end{aligned}$$

The variables we are interested in are the total temperature  $T_0$ , the total pressure  $p_0$  and the tangent of the flow angle  $tg_\alpha = v/u$ . The idea is to write the increment of these variables as a linear combination of the increments of the primitive variables. This can be obtained as follows:

$$\begin{aligned} T_{0i}^{n+1} - T_{0i}^n &= \delta T_0 + \delta T_0^* = \\ &= \frac{\partial T_0}{\partial \rho} (\delta \rho + \delta \rho^*) + \frac{\partial T_0}{\partial u} (\delta u + \delta u^*) + \frac{\partial T_0}{\partial v} (\delta v + \delta v^*) + \frac{\partial T_0}{\partial p} (\delta p + \delta p^*) , \quad (\text{D.1}) \end{aligned}$$

$$\begin{aligned} p_{0i}^{n+1} - p_{0i}^n &= \delta p_0 + \delta p_0^* = \\ &= \frac{\partial p_0}{\partial \rho} (\delta \rho + \delta \rho^*) + \frac{\partial p_0}{\partial u} (\delta u + \delta u^*) + \frac{\partial p_0}{\partial v} (\delta v + \delta v^*) + \frac{\partial p_0}{\partial p} (\delta p + \delta p^*) , \quad (\text{D.2}) \end{aligned}$$

$$tg_{\alpha i}^{n+1} - tg_{\alpha i}^n = \delta tg_{\alpha} + \delta tg_{\alpha}^* = \frac{\partial tg_{\alpha}}{\partial \rho} (\delta \rho + \delta \rho^*) + \frac{\partial tg_{\alpha}}{\partial u} (\delta u + \delta u^*) + \frac{\partial tg_{\alpha}}{\partial v} (\delta v + \delta v^*) + \frac{\partial tg_{\alpha}}{\partial p} (\delta p + \delta p^*) , \quad (\text{D.3})$$

where the vector of the corrective increments of the primitive variables is given by

$$\begin{bmatrix} \delta \rho^* \\ \delta u^* \\ \delta v^* \\ \delta p^* \end{bmatrix} = \beta^1 \mathbf{r}^1 + \beta^2 \mathbf{r}^2 + \beta^3 \mathbf{r}^3 . \quad (\text{D.4})$$

Substituting the expression of the eigenvectors in (D.4) and then inserting the expressions of the corrective increments of the primitive variables in equations (D.1), (D.2) and (D.3) one obtains a linear system for the unknowns  $\beta^k$  coefficients which can be solved as soon as informations are given on the time increments of  $T_0$ ,  $p_0$  and  $tg_{\alpha}$ . The final results are:

$$\begin{aligned} \beta^3 &= v_i^n \frac{\delta u}{u_{\perp}^n} - u_i^n \frac{\delta v}{u_{\perp}^n} - \beta^1 \frac{u_{\parallel}^n}{u_{\perp}^n} \\ \beta^2 &= \beta_{\Delta=0}^2 + \Delta \beta^2 , \\ \beta^1 &= \beta_{\Delta=0}^1 + \Delta \beta^1 \end{aligned}$$

where  $u_{\parallel} = un_{iy} - vn_{ix}$ ,  $\beta_{\Delta=0}^1$  and  $\beta_{\Delta=0}^2$  are the values of  $\beta^1$  and  $\beta^2$  obtained requiring  $\Delta T_0 = 0$  and  $\Delta p_0 = 0$  and are given by

$$\begin{aligned} \beta_{\Delta=0}^1 &= -\frac{\delta p / (\rho_i^n a_i^n) + 2\delta u_{\perp} k_{ei}^n / (a_i^n u_{\perp}^n)}{1 + 2k_{ei}^n / (a_i^n u_{\perp}^n)} , \\ \beta_{\Delta=0}^2 &= \frac{\delta p}{(a_i^n)^2} - \delta \rho \end{aligned}$$

By imposing a required value of  $T_0^{n+1}$  and  $\tilde{p}_0^{n+1}$  (see section 4.1), one can compute the additional terms  $\Delta \beta^1$  and  $\Delta \beta^2$  which are given by

$$\begin{aligned} \Delta \beta^1 &= \frac{\Delta p_0 / k_{ei}^n + \gamma \rho_i^n \Delta T_0 / (a_i^n)^2}{\rho_i^n a_i^n \lambda_* (1 + 2k_{ei}^n / (a_i^n u_{\perp}^n))} \\ \Delta \beta^2 &= (\gamma - 1) \frac{\rho_i^n}{a_i^n} \left( 1 + \frac{1k_{ei}^n}{a_i^n u_{\perp}^n} \right) \Delta \beta^1 - \frac{\gamma \rho_i^n}{(a_i^n)^2} \Delta T_0 , \end{aligned}$$

with

$$\begin{aligned} \lambda_* &= \frac{1}{k_{ei}^n} + \frac{\gamma - 1}{(a_i^n)^2} \\ \Delta T_0 &= R (T_0^* - T_0^n) , \\ \Delta p_0 &= \left( \frac{p_0^n}{p_i^n} \right)^{-\frac{1}{\gamma}} (p_0^* - p_0^n) \end{aligned}$$

where  $T_0^*$  and  $p_0^*$  are the required total temperature and pressure required at the inlet. Although less easy to prove,  $\beta^1$ ,  $\beta^2$  and  $\beta^3$  can be written, as in the previous cases, as  $\beta^k = \mathbf{D}^k \cdot \mathbf{R}_i + c^k$ .

## D.2 Two-Phase Equilibrium Model

### Inviscid Wall Condition for the 2D Mechanical Equilibrium Model

Only one positive eigenvalue is present in this case and it is given by  $\vec{u} \cdot \vec{n}_i$ . The correspondent right eigenvector is

$$\mathbf{r}^w = \begin{bmatrix} \rho_i^n a_i^n \\ n_{ix} \\ n_{iy} \\ \beta_i^n / a_i^n \end{bmatrix}.$$

The coefficient  $\beta^w$  required for the wall boundary condition  $\Delta u_\perp = 0$  is given by

$$\beta^w = \delta u_\perp.$$

### Subsonic Outlet Condition for the 2D Mechanical Equilibrium Model

Also in this case the only positive eigenvalue is given by  $\vec{u} \cdot \vec{n}_i$  with the correspondent right eigenvector

$$\mathbf{r}^a = \begin{bmatrix} \rho_i^n a_i^n \\ n_{ix} \\ n_{iy} \\ \beta_i^n / a_i^n \end{bmatrix}.$$

The coefficient  $\beta^a$  required for the wall boundary condition  $\Delta p = 0$  is given by

$$\beta^a = -\frac{\delta p}{\rho_i^n a_i^n}.$$

### Subsonic Inlet Condition for the 2D Mechanical Equilibrium Model

In this case three positive eigenvalues are present:  $\vec{u} \cdot \vec{n}_i$  and  $\vec{u} \cdot \vec{n}_i$  two times. The correspondent right eigenvectors are

$$\mathbf{r}^1 = \begin{bmatrix} \rho_i^n a_i^n \\ n_{ix} \\ n_{iy} \\ \beta_i^n / a_i^n \end{bmatrix}, \quad \mathbf{r}^2 = \begin{bmatrix} 0 \\ -n_{iy} \\ n_{ix} \\ 0 \end{bmatrix}, \quad \mathbf{r}^3 = \begin{bmatrix} 0 \\ 0 \\ 0 \\ 1 \end{bmatrix}.$$

The coefficients needed to impose the conditions  $\Delta(\rho u) = 0$ ,  $\Delta(\rho v) = 0$  and  $\Delta\alpha_g = 0$  are

$$\begin{aligned} \beta^1 &= -\frac{\left[ \left( \frac{\alpha_i^n}{a_i^n} + \frac{\alpha_{gi}^n}{(a_{gi}^n)^2} \right) u_\perp \delta p + \rho_i^n \delta u_\perp \right]}{\rho_i^n + \left( \frac{\alpha_i^n}{a_i^n} + \frac{\alpha_{gi}^n}{(a_{gi}^n)^2} \right) u_\perp \rho_i^n a_i^n} \\ \beta^2 &= -\frac{\left[ \left( \frac{\alpha_i^n}{a_i^n} + \frac{\alpha_{gi}^n}{(a_{gi}^n)^2} \right) u_\parallel \delta p + \rho_i^n \delta u_\parallel \right]}{\rho_i^n + \left( \frac{\alpha_i^n}{a_i^n} + \frac{\alpha_{gi}^n}{(a_{gi}^n)^2} \right) u_\parallel \rho_i^n a_i^n} \\ \beta^3 &= -\delta\alpha_g - \beta^1 \frac{\beta_i^n}{a_i^n} \end{aligned}.$$

For all the boundary conditions related to the Two-Fluid Model is also very easy to check that  $\beta^k = \mathbf{D}^k \cdot \mathbf{R}_i$ . In particular, note that since the computations were actually run in primitive variables, the provisional increments were simply computed as

$$\begin{aligned} \delta p &= -k_{i\Delta} (\mathbf{R}_i)_1 \\ \delta u &= -k_{i\Delta} (\mathbf{R}_i)_2 \\ \delta v &= -k_{i\Delta} (\mathbf{R}_i)_3 \\ \delta \alpha_g &= -k_{i\Delta} (\mathbf{R}_i)_4 \end{aligned} .$$

# Appendix E

## Equations, Jacobians and Eigenvalue Decompositions

### E.1 2D Euler Equations

For the Euler equations, two different sets of variables are used in the computations: the conservative variables given by

$$U = \begin{bmatrix} \rho \\ \rho u \\ \rho v \\ \rho E \end{bmatrix},$$

and the primitive variables, given by

$$P = \begin{bmatrix} \rho \\ u \\ v \\ p \end{bmatrix}.$$

The transformations jacobian matrices between the two sets of variables are

$$\frac{\partial U}{\partial P} = \begin{bmatrix} 1 & 0 & 0 & 0 \\ u & \rho & 0 & 0 \\ v & 0 & \rho & 0 \\ k_e & \rho u & \rho v & \frac{1}{\gamma-1} \end{bmatrix}, \quad \frac{\partial P}{\partial U} = \begin{bmatrix} 1 & 0 & 0 & 0 \\ -\frac{u}{\rho} & \frac{1}{\rho} & 0 & 0 \\ -\frac{v}{\rho} & 0 & \frac{1}{\rho} & 0 \\ (\gamma-1)k_e & -(\gamma-1)u & -(\gamma-1)v & \gamma-1 \end{bmatrix},$$

being  $k_e$  the kinetic energy per unit mass. In primitive variables the jacobian of the system is given by

$$C = \begin{bmatrix} \vec{V} \cdot \vec{n} & \rho n_x & \rho n_y & 0 \\ 0 & \vec{V} \cdot \vec{n} & 0 & \frac{n_x}{\rho} \\ 0 & 0 & \vec{V} \cdot \vec{n} & \frac{n_y}{\rho} \\ 0 & \rho a^2 n_x & \rho a^2 n_y & \vec{V} \cdot \vec{n} \end{bmatrix},$$

where  $\vec{V} \cdot \vec{n} = \vec{u} \cdot \vec{n}$  in the steady computations, while  $\vec{V} \cdot \vec{n} = un_x + vn_y + n_t$  for the space-time computations. The eigenvalues and eigenvectors of  $C$  can be computed as

$$\begin{aligned}\lambda_1 &= \vec{V} \cdot \vec{n}, \mathbf{r}^1 = \begin{bmatrix} 1 \\ 0 \\ 0 \\ 0 \end{bmatrix}, \\ \lambda_2 &= \vec{V} \cdot \vec{n}, \mathbf{r}^2 = \begin{bmatrix} 0 \\ -n_y \\ n_x \\ 0 \end{bmatrix}, \\ \lambda_3 &= \vec{V} \cdot \vec{n} + a, \mathbf{r}^3 = \begin{bmatrix} \frac{\rho}{a} \\ n_x \\ n_y \\ \rho a \end{bmatrix}, \\ \lambda_4 &= \vec{V} \cdot \vec{n} - a, \mathbf{r}^4 = \begin{bmatrix} \frac{\rho}{a} \\ -n_x \\ -n_y \\ \rho a \end{bmatrix}.\end{aligned}$$

For the boundary conditions the knowledge of the eigenvectors in conservative variables is needed. If  $\mathbf{r}_U$  indicates the generic eigenvector in conservative variables and  $\mathbf{r}_P$  indicates the generic eigenvector in primitive variables, one can easily prove that

$$\mathbf{r}_U = \frac{\partial U}{\partial P} \mathbf{r}_P.$$

Using the previous relation one obtains

$$\begin{aligned}\mathbf{r}_U^1 &= \begin{bmatrix} 1 \\ u \\ v \\ k_e \end{bmatrix}, \mathbf{r}_U^2 = \begin{bmatrix} 0 \\ -\rho n_y \\ \rho n_x \\ -\rho u n_y + \rho v n_x \end{bmatrix}, \\ \mathbf{r}_U^3 &= \begin{bmatrix} \frac{\rho}{a} \\ \rho(n_x + \frac{u}{a}) \\ \rho(n_y + \frac{v}{a}) \\ \rho \left( \frac{k_e}{a} + \frac{a}{\gamma-1} + un_x + vn_y \right) \end{bmatrix}, \mathbf{r}_U^4 = \begin{bmatrix} \frac{\rho}{a} \\ \rho(-n_x + \frac{u}{a}) \\ \rho(-n_y + \frac{v}{a}) \\ \rho \left( \frac{k_e}{a} + \frac{a}{\gamma-1} - un_x - vn_y \right) \end{bmatrix}.\end{aligned}$$

Note that all the previous matrices have been computed with the hypothesis  $n_x^2 + n_y^2 = 1$

## E.2 1D Euler Equations

Also for the 1D Euler equations, two different sets of variables are used in the computations: the conservative variables given by

$$U = \begin{bmatrix} \rho \\ \rho u \\ \rho E \end{bmatrix},$$

and the primitive variables, given by

$$P = \begin{bmatrix} \rho \\ u \\ p \end{bmatrix} .$$

The transformations jacobian matrices between the two sets of variables are

$$\frac{\partial U}{\partial P} = \begin{bmatrix} 1 & 0 & 0 \\ u & \rho & 0 \\ k_e & \rho u & \frac{1}{\gamma-1} \end{bmatrix} , \quad \frac{\partial P}{\partial U} = \begin{bmatrix} 1 & 0 & 0 \\ -\frac{u}{\rho} & \frac{1}{\rho} & 0 \\ (\gamma-1)k_e & -(\gamma-1)u & \gamma-1 \end{bmatrix} ,$$

being  $k_e$  the kinetic energy per unit mass. Since in 1D only space-time computations have been performed, it is the space-time jacobian that is reported here. In primitive variables it reads

$$C = \begin{bmatrix} un_x + n_t & \rho n_x & 0 \\ 0 & un_x + n_t & \frac{n_x}{\rho} \\ 0 & \rho a^2 n_x & un_x + n_t \end{bmatrix} ,$$

The eigenvalues and eigenvectors of  $C$  can be computed as

$$\begin{aligned} \lambda_1 &= \vec{V} \cdot \vec{n} , \quad \mathbf{r}^1 = \begin{bmatrix} 1 \\ 0 \\ 0 \end{bmatrix} , \\ \lambda_2 &= \vec{V} \cdot \vec{n} + a|n_x| , \quad \mathbf{r}^2 = \begin{bmatrix} \frac{\rho}{a} \\ n_x/|n_x| \\ \rho a \end{bmatrix} , \\ \lambda_3 &= \vec{V} \cdot \vec{n} - a|n_x| , \quad \mathbf{r}^3 = \begin{bmatrix} \frac{\rho}{a} \\ -n_x/|n_x| \\ \rho a \end{bmatrix} . \end{aligned}$$

For the boundary conditions the knowledge of the eigenvectors in conservative variables is needed. If  $\mathbf{r}_U$  indicates the generic eigenvector in conservative variables and  $\mathbf{r}_P$  indicates the generic eigenvector in primitive variables, one can easily prove that

$$\mathbf{r}_U = \frac{\partial U}{\partial P} \mathbf{r}_P .$$

Using the previous relation one obtains

$$\mathbf{r}_U^1 = \begin{bmatrix} 1 \\ u \\ k_e \end{bmatrix} , \quad \mathbf{r}_U^2 = \begin{bmatrix} \frac{\rho}{a} \\ \rho \left( \frac{n_x}{|n_x|} + \frac{u}{a} \right) \\ \rho \left( \frac{k_e}{a} + \frac{a}{\gamma-1} + u \frac{n_x}{|n_x|} \right) \end{bmatrix} , \quad \mathbf{r}_U^3 = \begin{bmatrix} \frac{\rho}{a} \\ \rho \left( -\frac{n_x}{|n_x|} + \frac{u}{a} \right) \\ \rho \left( \frac{k_e}{a} + \frac{a}{\gamma-1} - u \frac{n_x}{|n_x|} \right) \end{bmatrix} ,$$

### E.3 2D Two-Phase Equilibrium Model

The complete jacobian of the system reads in primitive variables

$$C = \begin{bmatrix} \vec{V} \cdot \vec{n} & \rho a^2 n_x & \rho a^2 n_y & 0 \\ n_x/\rho & \vec{V} \cdot \vec{n} & 0 & 0 \\ n_y/\rho & 0 & \vec{V} \cdot \vec{n} & 0 \\ 0 & \beta n_x & \beta n_y & \vec{V} \cdot \vec{n} \end{bmatrix},$$

where in the case of space-time computations  $\vec{V} \cdot \vec{n} = un_x + vn_y + n_t$ . The following eigenvalue decomposition can be proven:

$$C = R\Lambda L,$$

with

$$R = \begin{bmatrix} \rho a & \rho a & 0 & 0 \\ n_x & -n_x & -n_y & 0 \\ n_y & -n_y & n_x & 0 \\ \beta/a & \beta/a & 0 & 1 \end{bmatrix}, \quad L = \begin{bmatrix} \frac{1}{2\rho a} & \frac{1}{2}n_x & \frac{1}{2}n_y & 0 \\ \frac{1}{2\rho a} & -\frac{1}{2}n_x & -\frac{1}{2}n_y & 0 \\ 0 & -n_y & n_x & 0 \\ -\frac{\beta}{\rho a^2} & 0 & 0 & 1 \end{bmatrix},$$

and

$$\Lambda = \begin{bmatrix} \vec{V} \cdot \vec{n} + a & 0 & 0 & 0 \\ 0 & \vec{V} \cdot \vec{n} - a & 0 & 0 \\ 0 & 0 & \vec{V} \cdot \vec{n} & 0 \\ 0 & 0 & 0 & \vec{V} \cdot \vec{n} \end{bmatrix}.$$

Note that all the previous matrices have been computed with the hypothesis  $n_x^2 + n_y^2 = 1$

### E.4 1D Two-Phase Equilibrium Model

The 1D space-time jacobian of the system reads in primitive variables

$$C = \begin{bmatrix} un_x + n_t & \rho a^2 n_x & 0 \\ n_x/\rho & un_x + n_t & 0 \\ 0 & \beta n_x & un_x + n_t \end{bmatrix}.$$

The following eigenvalue decomposition can be proven:

$$C = R\Lambda L,$$

with

$$R = \begin{bmatrix} \rho a & \rho a & 0 \\ n_x/|n_x| & -n_x/|n_x| & 0 \\ \beta/a & \beta/a & 1 \end{bmatrix}, \quad L = \begin{bmatrix} \frac{1}{2\rho a} & \frac{n_x}{2|n_x|} & 0 \\ \frac{1}{2\rho a} & -\frac{n_x}{2|n_x|} & 0 \\ -\frac{\beta}{\rho a^2} & 0 & 1 \end{bmatrix},$$

and

$$\Lambda = \begin{bmatrix} un_x + n_t + a|n_x| & 0 & 0 \\ 0 & un_x + n_t - a|n_x| & 0 \\ 0 & 0 & un_x + n_t \end{bmatrix}.$$

# Bibliography

- [1] H. Paillère, *Multidimensional Upwind Residual Distribution Schemes for the Euler and Navier-Stokes Equations on Unstructured Grids*, PhD thesis, Université Libre de Bruxelles, June 1995
- [2] E. van der Weide, *Compressible Flow simulation on Unstructured Grids using Multidimensional Upwind Schemes*, PHD thesis, Technical University of Delft, November 1998
- [3] H.Deconinck, K. Sermeus and R.Abgrall, *Status of Multidimensional Upwind Residual Distribution Schemes and Applications in Aeronautics*, AIAA-CP 2000-2328, 2000
- [4] Á. Csík, H. Deconinck and S. Poedts, *Monotone Residual Distribution Schemes for the Ideal 2D MHD on Unstructured Grids*, AIAA-CP 99-3325, 1999
- [5] E. Valero, *Advanced 2D Two-Phase Flow Simulation Tool for Application to Reactor Safety*, VKI-TN 2001-198, von Karman Institute, 2001
- [6] J. Maerz and G. Degrez *Improving time accuracy for residual distribution schemes*, VKI-PR 1996-17, von Karman Institute, 1996
- [7] A.Ferrante and H. Deconinck *Solution of the Unsteady Euler Equations using Residual Distribution and Flux Corrected Transport*, VKI-PR 1997, von Karman Institute, 1997
- [8] S.T.Zalesak, *Fully multidimensional flux-corrected transport algorithm for fluids*, Journal Computational Physics, Vol. 31, 1979
- [9] R. Lohner, K. Morgan, J. Peraire and M.Vahdati, *Finite element flux-corrected transport (FEM-FCT) for the Euler and Navier-Stokes equations*, International Journal for Numerical Methods in Fluids, vol.7, 1987
- [10] M.E.Hubbard and P.L.Roe, *Compact High-Resolution Algorithms for Time-Dependent Advection on Unstructured Grids*, International Journal for Numerical Methods in Fluids, Vol. 33, No. 5, 1997
- [11] M. Ricchiuto and H. Deconinck *Time Accurate Solution of Hyperbolic Partial Differential Equations using FCT and Residual Distribution Schemes*, VKI-SR 1999-33, von Karman Institute, 1999

- [12] Á. Csík, H. De Sterck, M. Ricchiuto, S. Poedts, H. Deconinck and D. Roose, *Explicit and Implicit Parallel Upwind Monotone Residual Distribution Solver for the Time Dependent Ideal 2D and 3D Magnetohydrodynamics Equations on Unstructured Grids*, Second International Conference on Engineering Computational Techniques, Leuven, 2000
- [13] R. Abgrall and M. Mezone, *A Consistent Upwind Residual Scheme for Unsteady Advection Problems*, AMIF Conference, Italy, 2000
- [14] Á. Csík, M. Ricchiuto, H. Deconinck and S. Poedts, *Space Time Residual Distribution Schemes for Hyperbolic Conservation Laws*, Proc. 15th AIAA CFD Conference, 2001
- [15] Á. Csík and H. Deconinck, *Space Time Residual Distribution Schemes for Hyperbolic Conservation Laws on Unstructured Linear Finite Elements*, in Proc. ICFD conf., Oxford, 2001
- [16] R. Abgrall, *Toward the Ultimate Conservative Scheme: Following the Quest*, Journal of Computational Physics, Vol. 167, 2001
- [17] M. Ishii, *Thermo-Fluid Dynamic Theory of Two-Phase Flow*, Eyrolles, Paris, 1975
- [18] I. Tóth, A. Kumbaro and H. Paillère, *Approximate Riemann Solvers and Flux Vector Splitting Schemes for Two-Phase Flow*, 30<sup>th</sup> VKI Lecture Series in Computational Fluid Dynamics, March 1999
- [19] M. Ricchiuto and H. Deconinck, *Two-Phase Flow Computations Using a Two-Fluid Model and Fluctuation Splitting Schemes*, VKI-SR 2000-13, von Karman Institute, 2000
- [20] E. van der Weide, K. Sermeus and H. Deconinck, *Industrial Demonstration of Accurate and Efficient Multidimensional Upwind and Multi grid Algorithms for Aerodynamic Simulation on Unstructured Grids*, VKI-TR, von Karman Institute 1998
- [21] H. Deconinck, P.L. Roe and R. Struijs, *A Multidimensional Generalization of Roe's Flux Difference Splitter for the Euler Equations*, Journal of Computers and Fluids, Vol. 22, 1993
- [22] A. Üngör, C. Heeren, X.-Y. Li, A. Sheffer, R. Haber and S.-H. Teng, *Constrained 2D Space-Time Meshing With All Tetrahedra*
- [23] P.L. Roe, *Characteristic-Based Schemes for the Euler Equations*, Ann. Rev Fluid Mech., Vol. 18, 1986
- [24] F. Alouges, J.-M. Ghidaglia and M. Tajchman, *On the Interaction of Upwinding and Forcing for Nonlinear Hyperbolic Systems of Conservation Laws*
- [25] M.E. Hubbard and P. Garcia-Navarro, *Flux Difference Splitting and the Balancing of Source Terms and Flux Gradients*, Journal of Computational Physics, Vol. 165, 2000
- [26] W.A. Wood, *Equivalence of Fluctuation Splitting and Finite Volume for One-Dimensional Gas Dynamics*, NASA/TM-97-206271, 1997

- [27] H. Deconinck, personal communication
- [28] C. Hirsch, *Numerical Computation of Internal and External Flows*, Vol. 1 and 2, Wiley 1990
- [29] P. Colella and P. Woodward, *The Numerical Simulation of Two-Dimensional Flows with Strong Shocks*, Journal of Computational Physics, Vol. 83, 1984
- [30] B. Cockburn, *Discontinuous Galerkin Methods for Convection-Dominated Problems*, in High Order Methods for Computational Physics, T.J. Barth and H. Deconinck Eds., 1999
- [31] A. Böles, T.H. Fransson and M.F. Platzer, *Numerical Simulation of Inviscid Transonic Flow Through Nozzles with Fluctuating Back Pressure*, ASME Journal of Turbomachinery, Vol. 111, 1989
- [32] C.J. Hwang and J.L. Liu, *Locally Implicit Hybrid Algorithm for Steady and Unsteady Viscous Flows*, AIAA Journal, Vol. 30, 1992
- [33] P. Rogiest, *An Implicit Finite Volume Scheme for the Computation of Unsteady Compressible Flow on Multi-Block Structured Grids. Application to Aeroelastic Problems.*, PhD Thesis, Université de Liège, April 1997
- [34] E.F. Toro, *Riemann Solvers and Numerical Methods for Fluid Dynamics - A Practical Introduction*, Springer 1997
- [35] J. Peuteman, *Application of the Time Dependent Gasdynamic Equations to Steady Flow*, VUB Internal Report
- [36] J.C. Martin and W.J. Moyce, *An Experimental Study of the Collapse of Liquid Columns on a Rigid Horizontal Plane*, Phils. Trans. R. Soc. Lond, Vol. 244, 1952
- [37] S. Koshizuka, H. Tamako and Y. Oka, *A Particle Method for Incompressible Viscous Flow with Fluid Fragmentation*, Journal of Computational Fluid Dynamics, Vol. 4, 1995
- [38] D. Sidilkover, *A new Time-Space Accurate Scheme for Hyperbolic Problems I: Quasi-Explicit Case*, ICASE Report No 98-25, 1998